Universidade Vigo

Departamento de Química Física

PhD Thesis

ENGINEERING THE MORPHOLOGY AND ORGANIZATION OF GOLD NANOSTRUCTURES FOR SERS DETECTION

Director: Professor Luis Manuel Liz Marzán
Candidate: Andrea La Porta

CIC biomaGUNE
Centro de Investigación Cooperativa en Biomateriales

Vigo, Diciembre de 2015

D. Luis Manuel Liz Marzán, Catedrático del Departamento de Química Física de la Universidad de Vigo informa que:

Andrea La Porta, licenciado en Física, ha realizado en el Centro de Investigaciones Cooperativas en Biomateriales (CICbiomaGUNE) de San Sebastián bajo su dirección el trabajo descrito en la presente memoria, que lleva por título "Engineering the Morphology and Organization of Gold Nanostructures for SERS Detection", y que presenta para optar al grado de Doctor por la Universidad de Vigo con Mención Internacional.

Vigo, 14 de Diciembre de 2015

Fdo. Luis Manuel Liz Marzán

Contents

CHAPTER 5

THESIS SCOPE

Since its discovery, *Surface-enhanced Raman Scattering* (SERS) has become one of the most powerful and intensively studied spectroscopic analytical techniques. The electric near-field enhancement created by illumination of metallic nanostructures provides SERS with the ability to overcome the main drawback of standard Raman scattering spectroscopy, namely its low sensitivity. Many efforts are therefore currently devoted toward the fabrication of high-performance, homogeneous and reproducible SERS substrates by means of the most advanced methods, both top-down and bottom-up. Metallic nanoparticles represent an attractive route to the design of SERS supports with suitable properties. Among all the available metals and related alloys, gold and silver are the principal materials of choice because of their special interaction with light. Applications of SERS spectroscopy are foreseen in a wide variety of fields like medicine, biology, forensic science, archaeology, pharmacy and others.

The activity of the Bionanoplasmonics Laboratory at CIC biomaGUNE is focused on the chemical synthesis of Au and Ag nanoparticles with different sizes and shapes. The research in the group is also dedicated to the functionalization of the above-mentioned nanoparticles toward driving interparticle and particle-support interactions, to achieve control over self-assembly processes. Being able to tune morphology and organization allows the design of efficient SERS substrates since size, shape and interparticle distance are crucial parameters to create highly localized areas where the electric field is largely enhanced (*hot-spots*), leading to a suitable response of the substrate.

The scope of this thesis lies within the search for innovative and efficient SERS substrates that may become useful in the identification and quantification of specific chemical species. With the objective of expanding the potential field of application, different strategies have been followed in this process. After a brief general introduction, the selected strategies are presented in the subsequent chapters. Each of these chapters describes the ideas behind the work, as well as the experimental set-up, results and conclusions. Key bibliographic references are also provided, which can guide interested readers toward acquiring a more complete knowledge of the subject.

General considerations about the Raman effect and SERS spectroscopy are provided in Chapter 1, which are important for understanding the basic theoretical concepts behind these spectroscopy techniques. The chapter is also dedicated to discuss the optical properties of Au and Ag nanoparticles, as these are the most frequently used materials in SERS. A final section is aimed to give an overview on some common procedures to fabricate SERS substrates and a series of representative examples is discussed.

Chapter 2 deals with a chemical method leading to the vertical growth of Au seeds from a glass substrate. The highly anisotropic growth mechanism results in closely packed Au nanowires, which present interesting plasmonic properties. The possibility to tune the plasmon band by changing the length and diameter of each nanowire allows the choice of the optimal morphology according to the targeted SERS application. A particular application is demonstrated for this system in the detection of analytes in the gas phase.

Apart from efficiency, aspects like low cost and easy fabrication process are also important and should be taken into consideration during the development of a SERS substrate. In Chapter 3 standard industrial paper is used as a solid support for the adsorption of plasmonic nanoparticles. With no need for additional treatment of the paper support, the nanoparticles can be deposited until complete coverage of the paper fibers and directly used as a SERS support. In order to avoid problems related to the drying step, nanoparticles were deposited in the form of an ink, using a simple fountain pen. It is thus possible to obtain flexible SERS substrates where the nanoparticles are uniformly deposited into the desired pattern with no need of any expensive instrumentation or technique.

One of the problems when dealing with colloidal nanoparticles is that their SERS efficiency strongly depends on the stabilizing agents used in the synthesis process. Surfactants with high affinity for the metal prevent the analyte from getting close to the nanoparticle surface, where the electric field enhancement responsible for SERS detection is present. In chapter 4 we introduce a process for replacing the stabilizing agent covering the nanoparticle surface to facilitate adsorption of analyte molecules. This method allowed us to compare several morphologies with identical surface chemistry as well as reaching a limit of detection in the nanomolar range.

Apart from solid supports, colloidal solutions themselves can also be used as liquid substrates for SERS spectroscopy. This approach presents several advantages like reduced sample degradation or improved uniformity in the distribution of the analyte, and therefore represents a valid alternative to solid supports. We introduce in Chapter 5 a hybrid SERS substrate that combines the optical properties of Au nanoparticles and the magnetic response of magnetite nanocrystals. We were thus able to create a system whose SERS sensitivity can be increased by several orders of magnitude upon application of an external magnetic field.

As a whole, this thesis is expected to contribute toward the development of novel plasmonic nanoplatforms as sensible and reliable SERS substrates for sensing applications in various fields.

CHAPTER 1

GENERAL INTRODUCTION

1.1 The Raman effect

In 1928 C. V. Raman observed a new type of radiation resulting from light-matter interaction.[1] By using a set of lenses to focus sunlight onto a material and a very basic experimental setup he observed two kinds of scattered radiation: the most intense one maintained the same wavelength as the incident light, whereas the secondary one possessed a different wavelength. The effect responsible for such a shift in wavelength is known today as *Raman scattering* and is widely used as a non-invasive analytical tool to obtain accurate information about the chemical composition of the sample and thus allows us to identify specific substances regardless of their physical state (liquid, gas or solid).[2]

Let us consider a monochromatic light beam with a specific frequency ω_I interacting with a molecule (Figure 1.1a). The incident light can be scattered either elastically or inelastically by the molecule itself. If the frequency of the scattered radiation (ω_L) is equal to ω_i (elastic interaction) the process is called *Rayleigh Scattering* while it is called *Raman Scattering* when it is shifted by a certain amount, ω_S (inelastic interaction). Within Raman scattering two distinct cases can be distinguished: *Stokes* and *Anti-Stokes Scattering*, when $\omega_L = \omega_i - \omega_S$ and $\omega_L = \omega_i + \omega_S$, respectively.

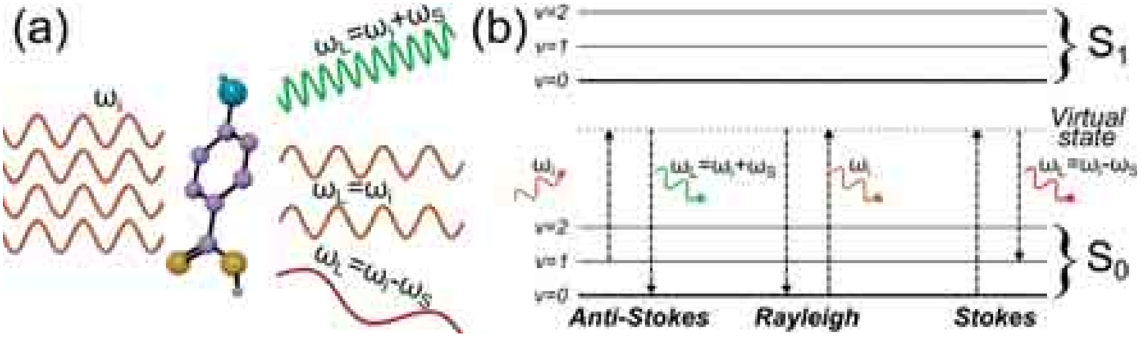

Figure 1.1. (a) Schematic representation of the three scattering processes occurring during the interaction of light with a molecule. (b) Jablonski diagram showing the electronic transitions involved.

The shift in frequency ω_S corresponds to the energy of some vibrational level, which is excited by the incident light. Figure 1.1b shows a simplified Jablonski diagram of the three processes occurring upon light-molecule interaction. Different to other optical phenomena (i.e. fluorescence), the Raman effect is a scattering process. This means that the incident photon does not need to have the exact energy corresponding to a real state of the molecule and be absorbed, but it can reach a so-called *virtual state* and then instantaneously decay into another state. It is important to stress that the virtual state does not physically exist but it is useful in the understanding of the effect.[3] In some practical cases it might happen that the energy of the incident light matches the frequency of a molecular electronic transition or, in other words, the energy of the virtual state is close to the energy of an electronic level of the molecule. This situation is called *resonance* and the phenomenon is known as *Resonance Raman Scattering* (RRS). The direct consequence of the resonance is an enhancement of the scattering efficiency of the molecule.[4]

There is a general selection rule that allows us to predict whether a certain molecular vibration will be Raman excited or not: a vibration is said to be *Raman active* when a change in the polarizability α of the molecule, i.e. its ability to distort the electronic cloud, is produced. This is different from what happens, for example, in infrared spectroscopy where the vibration must induce a change in the dipole of the molecule so as to appear in the infrared spectrum. As a consequence, symmetric and asymmetric vibrations are very intense in Raman and Infrared spectra, respectively.

Raman scattering is a rather weak effect. In fact, Rayleigh, Stokes and Anti-Stokes effects do not occur with the same probability. The interaction between the incident light and the molecule is mainly elastic and only one in every 10^6-10^8 photons is Raman scattered. Moreover, most of the incident photons are rather Stokes scattered than Anti-Stokes depending on the initial state of the molecule (Figure 1.2). Indeed, Anti-Stokes scattering needs the molecule to be already in an excited state, while prior to the interaction with the light the vast majority of the molecules at room temperature are found to be in their ground vibrational state.

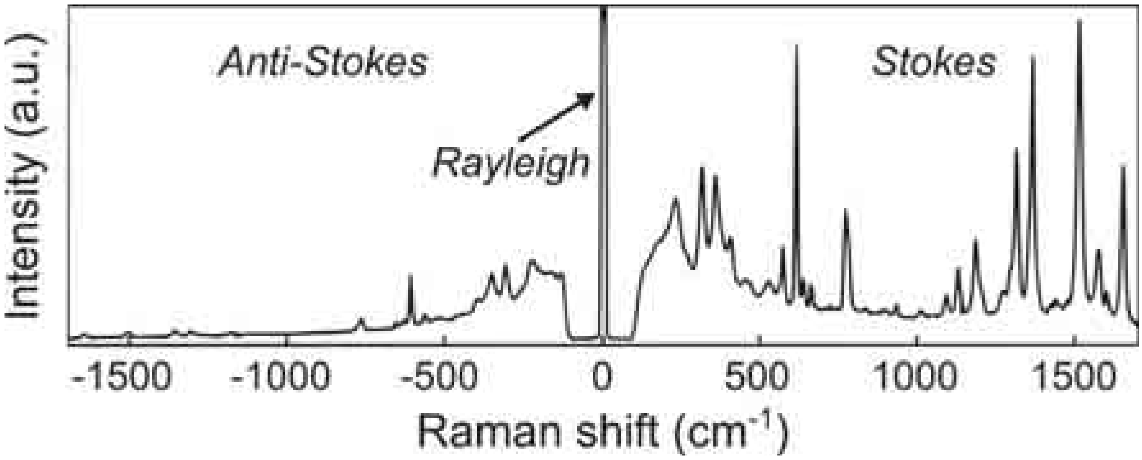

Figure 1.2. Anti-Stokes, Rayleigh and Stokes peaks. At room temperature, almost all the molecules are in the ground vibrational level, this resulting in a different intensity of Stokes (stronger) and Anti-Stokes (weaker) scattering.[2]

The ratio between the number of molecules in the excited and ground levels is given by Boltzmann's equation:

$$\frac{N_n}{N_m} = \frac{g_n}{g_m} exp\left[\frac{-(E_n - E_m)}{kT}\right] \qquad \textit{Equation 1.1}$$

where *n* and *m* indicate the excited and ground vibrational levels, respectively, *N* the number of molecules, *g* the degeneracy and *E* the energy.[2]

One of the most important aspects of Raman spectroscopy is the concept of *Raman cross-section*. By definition, the Raman cross-section of a certain molecule is the effective area of a homogeneous incident beam from which every photon will be Raman scattered by the molecule itself. In other words, the Raman cross-section σ_R [m^2] relates the incident power density S_0 [Wm^{-2}] to the Raman scattered intensity of a given vibrational mode P_R [W] averaged over all possible orientations of the molecule in space. However, in real experimental situations the detector is placed along a specific direction and there is no interest in knowing the scattered power over all possible directions. In order to take into account the so-called *radiation profile* (i.e. number of photons scattered along a well defined direction) the definition of P_R is given by

$$\frac{dP_R}{d\Omega}(\Omega) = \frac{d\sigma_R}{d\Omega}(\Omega)S_0 \qquad \textit{Equation 1.2}$$

where the variable $\Omega(\theta, \phi)$ is the solid angle that defines the scattering direction. The term $d\sigma_R/d\Omega$ [m^2sr^{-1}] describes the scattering efficiency along the direction defined by Ω and it is called *differential Raman cross-section* and in some cases it is used to calculate the *absolute Raman cross-section* σ_R [m^2] by integrating it over all the possible directions. Figure 1.3 shows a comparison of σ_R for the most common optical processes in spectroscopy. In Raman spectroscopy typical values for σ_R are in the order of magnitude of 10^{-29} cm^2 while for RSS it increases up to 10^{-24} cm^2. In any case, event in resonant conditions the Raman cross-section is much smaller than other optical phenomena like fluorescence (~10^{-19} cm^2) or UV absorption (~10^{-18} cm^2).[4]

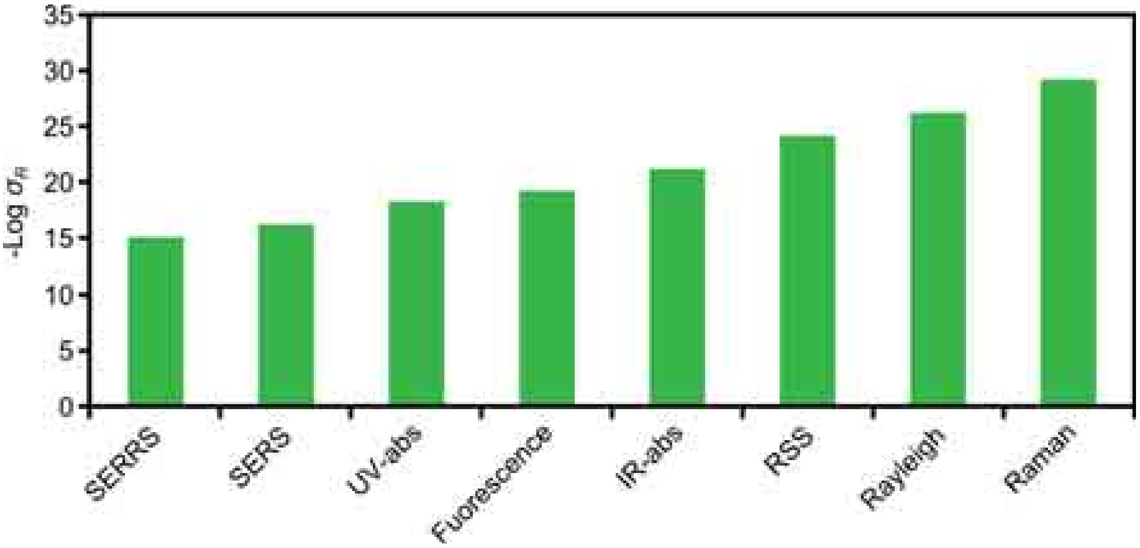

Figure 1.3. Cross-section comparison for the most common optical spectroscopic techniques.

1.2 Surface-enhanced Raman Scattering

Surface-enhanced Raman Scattering (SERS) was observed for the first time by *Fleischman* and co-workers[5] in 1974, when they observed a surprisingly high intensity of the Raman signal coming from pyridine adsorbed onto electrochemically roughened silver electrodes. Their explanation of the phenomenon was based on the increased amount of molecules onto the electrode surface due the roughness. The actual discovery of SERS is often attributed to *Jeanmarie* and *Van Duyne*[6] and to *Albrecht* and *Creighton*[7] who simultaneously demonstrated in 1977 that a higher concentration of analyte is not able to explain the observed strong Raman enhancement ($\sim 10^5$-10^6) and proposed the idea of a different kind of interaction between the metallic surface and the molecule adsorbed onto it.[3] An idea of the strength of this enhancement can be given by looking at the σ_R values in Fig. 1.3: for SERS they are approximately around 10^{-16} cm^2 which means more than ten orders of magnitude larger than for standard Raman scattering. When SERS is performed with a probe under RSS conditions it is often referred to as *Surface-enhanced Resonant Raman Scattering* (SERRS). As it can be seen again in Fig. 1.3, working in SERRS conditions allows us to lower an additional order of magnitude the σ_R of the process.[4]

During the decades following its discovery, SERS has been the subject of an intense research activity. Many factors played a crucial role in the fast worldwide diffusion of SERS:

- ✓ Improvement in Raman scattering instrumentation allowed scientists to perform a wide variety of measurements while making every experiment faster;
- ✓ Progress in chemical and physical sciences has driven the development of new techniques for the fabrication of efficient and reproducible SERS substrates, i.e. chemical synthesis of nanoparticles (NPs) with many different morphologies and increasingly accurate instruments for lithographic fabrication;
- ✓ Some studies predicted the possibility of single molecule detection;[8,9]
- ✓ Advantages of SERS as compared with other detection techniques. Apart from being a non-invasive tool and working under a broad range of conditions (temperature, pressure), the most attractive aspect of SERS is the possibility to analyze very small amounts of sample (down to single molecule) and obtain specific spectra (fingerprints) with high spatial resolution.

Nowadays SERS is one of the most powerful techniques for trace detection and for the study of molecules adsorbed onto a surface. SERS as an analytical tool is used today in many different fields, such as: analytical chemistry[10–12], biology and biotechnology[13–17], forensic science[18,19], study of artistic objects[20–22], biochemical sensing, diagnostics and other applications[23].[24]

1.2.1 Optical Properties of Metals: The Case of Silver and Gold

The main experimental difference between Raman scattering and SERS is the presence of a metallic enhancer in the latter. Because of their special optical properties, nanostructured metals (Ag and Au in particular) are essential in the enhancement mechanism of SERS spectroscopy. The optical properties of any bulk material are defined by their dielectric functions $\varepsilon(\lambda)$ which describes the material's response to an applied electric field and it is a function of the field's wavelength λ. As a general rule, $\varepsilon(\lambda)$ can be real or complex depending on whether the material is transparent or opaque, respectively. Metals are included in the list of materials for which $\varepsilon(\lambda)$ is complex and can thus be expressed as:

$$\varepsilon(\lambda) = Re[\varepsilon(\lambda)] + iIm[\varepsilon(\lambda)] \qquad \textit{Equation 1.3}$$

Figure 1.4 shows a plot of $\varepsilon(\lambda)$ of Ag and Au, which are the most often used metals in SERS spectroscopy. Looking at both $Re[\varepsilon(\lambda)]$ and $Im[\varepsilon(\lambda)]$ it is possible to deduce some conclusions that turn out to be of crucial importance in understanding the different behaviour of Ag and Au as SERS substrates:

- ✓ The real parts of both dielectric functions (Fig. 1.4a) have approximately the same trend, this meaning that Ag and Au actually have very similar electronic densities. Moreover, their values are both large in magnitude and negative.
- ✓ On the other hand, the imaginary components of $\varepsilon(\lambda)$ (Fig. 1.4b) look totally different from each other for $\lambda \leq 600$ nm. Even though the values are small compared with $Re[\varepsilon(\lambda)]$, $Im[\varepsilon(\lambda)]$ determines the optical response of a material interacting with light. In fact, it is related to the absorption of the material. Due to the interband electronic transitions which occur in Au and not in Ag, the absorption is higher for Au when $\lambda \leq 600$ nm. For longer wavelengths $Im[\varepsilon(\lambda)]$

of both materials follows the same trend, meaning that in that spectral region Au and Ag are very similar from an electromagnetic point of view.

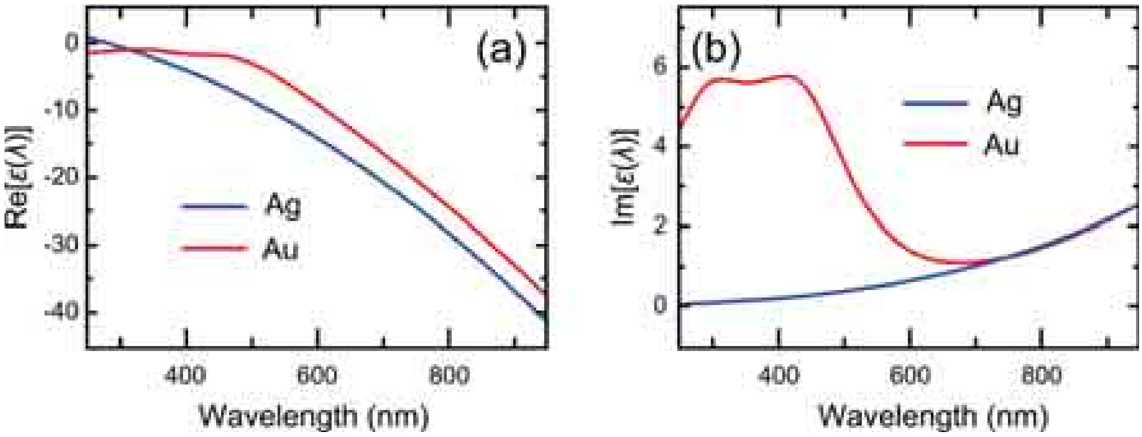

Figure 1.4. (a) Re[ε(λ)] and (b) Im[ε(λ)] of the dielectric function ε(λ) for Au and Ag. While the real parts of these two materials present very similar behavior, the difference in the imaginary parts at short wavelengths is the main reason for their optical response.[24]

Let us consider a metallic sphere interacting with an external electric field. By solving Maxwell's equations it is possible to determine exactly the value of the electric field induced inside the sphere by the applied one. However, in many practical cases the so-called *electrostatic approximation* can be used. In this approximation the external electric field is considered as a uniform field oscillating up and down with a specific frequency and therefore it is valid only in the case that the size of the object is at least one or two orders of magnitude smaller than the wavelength of the field oscillation. Under these conditions it can be demonstrated that, due to the oscillating free electrons, the electric field induces an electric dipole p in the sphere:

$$p \propto \frac{\varepsilon(\lambda)-\varepsilon_M}{\varepsilon(\lambda)+2\varepsilon_M}$$ *Equation 1.4*

where ε_M is the dielectric function of the embedding medium. Considering that $\varepsilon(\lambda)$ is complex, it is not possible to satisfy the condition $\varepsilon(\lambda) = -2\varepsilon_M$, which would imply the strongest response of the sphere (*resonance*). In any case, it is interesting to consider the situation in which Re[ε(λ)]= $-2\varepsilon_M$ because in that case the intensity of p is only limited by the magnitude of the imaginary part at that particular λ: the smaller Im[ε(λ)] the stronger p. Such oscillations of free electrons in small particles due to electric fields are called *Localized Surface Plasmon Resonances* (LSPR).

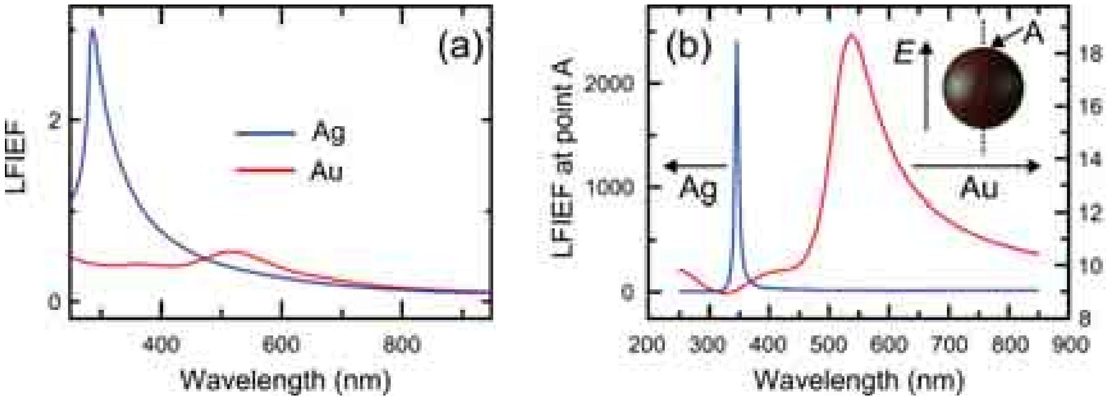

Figure 1.5. Au and Ag LFIEFs in the case of (a) flat and (b) spherical metal-air interfaces. A change in the geometry of the object induces a strong enhancement of the electric field onto the metallic surface.[24]

Figure 1.5a shows the *Local Field Intensity Enhancement Factor* (LFIEF) at Ag-air and Au-air interfaces, for the case in which the metal surfaces are considered to be flat. LFIEF is defined as the intensity of the electric field in the presence of an object, normalized with respect to the intensity the electric field would have without that object. In other words, it describes whether an incident electric field is enhanced (LFIEF>1) or quenched (LFIEF<1) by an external object interacting with it. In the specific case of Ag and Au the LFIEF is <1 almost in the complete visible range. Only for Ag and $\lambda \leq 400$ nm the LFIEF is >1 and its value is around three at its maximum. All these considerations about the LFIEF seem to bring to the conclusion that there is not a real advantage in using metals as electric field enhancers because they mostly quench the initial intensity. The crucial concept here is the shape of the metallic object. Going back to the sphere problem, it is possible to see in Figure 1.5b what actually happens when the metal-air interface is not flat anymore but spherical. The plot describes the LFIEF behavior for both Ag and Au at a point A onto the surface of the sphere along the direction defined by the electric field oscillations.

Three main considerations can be made here:

- ✓ For both Ag and Au the resonance peak appears at the λ where the condition $\mathrm{Re}[\varepsilon(\lambda)] = -2\varepsilon_M$ is satisfied (see Fig. 1.4a);
- ✓ The imaginary part at this specific λ is much smaller for Ag. As discussed before, this reduces absorption and losses in Ag and, as a consequence, makes the peak stronger and narrower;
- ✓ LFIEF resonances are much stronger as compared with the case of flat surfaces (Fig. 1.5a). Especially for Ag, a molecule placed in point A onto the sphere surface would sense an electric field three orders of magnitude more intense than in any other place.

As a result of the dependence of the electromagnetic behavior of an object on its shape, each structure has a characteristic absorption spectrum whose peaks correspond to the LSPR for that particular shape. Figure 1.6a shows absorbance spectra of different NP geometries.

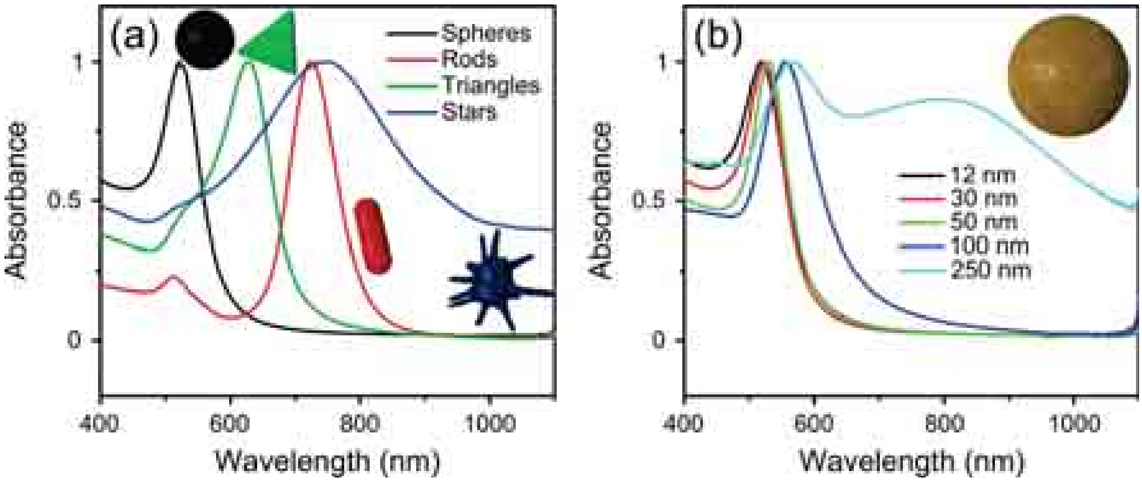

Figure 1.6. (a) Normalized UV-Vis spectra of Au NPs with different geometries. The LSPR is sensitive, among other factors, to shape, size and material. (b) Normalized UV-Vis spectra of Au spherical NPs of different sizes: an increase in the dimensions induces a red-shift of the LSPR and activation of higher-order resonances.

For anisotropic shapes, more than one LSPR peaks are possible. This is the case, for example, of Au nanorods (NRs) where a transversal and a longitudinal band are visible, corresponding to the oscillation of the electric field along the short and long axes of the rod. In the specific case of Figure 1.6a, transversal and longitudinal bands peak at ~ 513 nm and ~724 nm, respectively. Not only the shape can affect the LSPR of a nanostructure: in Figure 1.6b UV-Vis spectra of Au spheres with different sizes are shown. As the size increases, the LSPR peak shifts to longer wavelengths (red-shift) and becomes broader due to increased radiation losses. Another important effect of increasing the size of the NPs is the appearance of higher-order resonances. As indicated above, the electrostatic approximation is valid only when the size of the metallic objects is several orders of magnitude smaller than the wavelength of the incident light. As wavelength and size become comparable the electrostatic approximation fails, the electric field on the surface cannot be considered uniform anymore and as a consequence new resonances appear. In the case of 250 nm spheres in Fig. 1.6b the peak at ~ 570nm is known as quadrupolar resonance.[24]

Silver and gold are not the only metals that can enhance incident electric fields. Several works have been carried out using Al, Pt, Ru, Rh, Pd, Fe, Co and their alloys.[25–29] The reason why these metals are not so widely used for SERS spectroscopy is that their dielectric functions lead to broader and weaker LSPRs as compared with Ag and Au. Even if Ag is the best performing material in terms of electric field enhancement, very often Au is preferred for other reasons.[30] In biological applications of SERS, for example, the spectral region $\lambda \geq 700$ nm (NIR) becomes very important[14,31–33] and in this region Ag and Au become electromagnetically identical due to the similar trends in the imaginary part of their dielectric functions. In these conditions where Ag has not any LFIEF-related advantage, Au is always preferred because of its higher chemical stability and biocompatibility.[24]

1.2.2 Electromagnetic enhancement

In order to describe in more detail the electromagnetic enhancement mechanism that is responsible for the high sensitivity of SERS, let us consider two Au spheres interacting with an incident laser beam defined by its frequency ω_{inc} and electric field amplitude E_0. In this particular case the interparticle distance is big enough to avoid any kind of optical interaction between the two spheres. As previously shown, the result is the formation of an induced electric dipole in the spheres that oscillates at the same frequency ω_{inc} but whose intensity E_{loc} is significantly higher than E_0 along the oscillation axis of the electric field (Figure 1.7a). If the two spheres are so close each other (few nanometers) that their mutual interactions cannot be neglected anymore, the electric field intensity in the space between them becomes several orders of magnitude higher than before due to coupling of individual LSPRs (Figure 1.7b). These highly localized areas are known as *hot-spots* and examples of enhancements of the order of 10^8-10^{10} or higher have been reported in the literature.

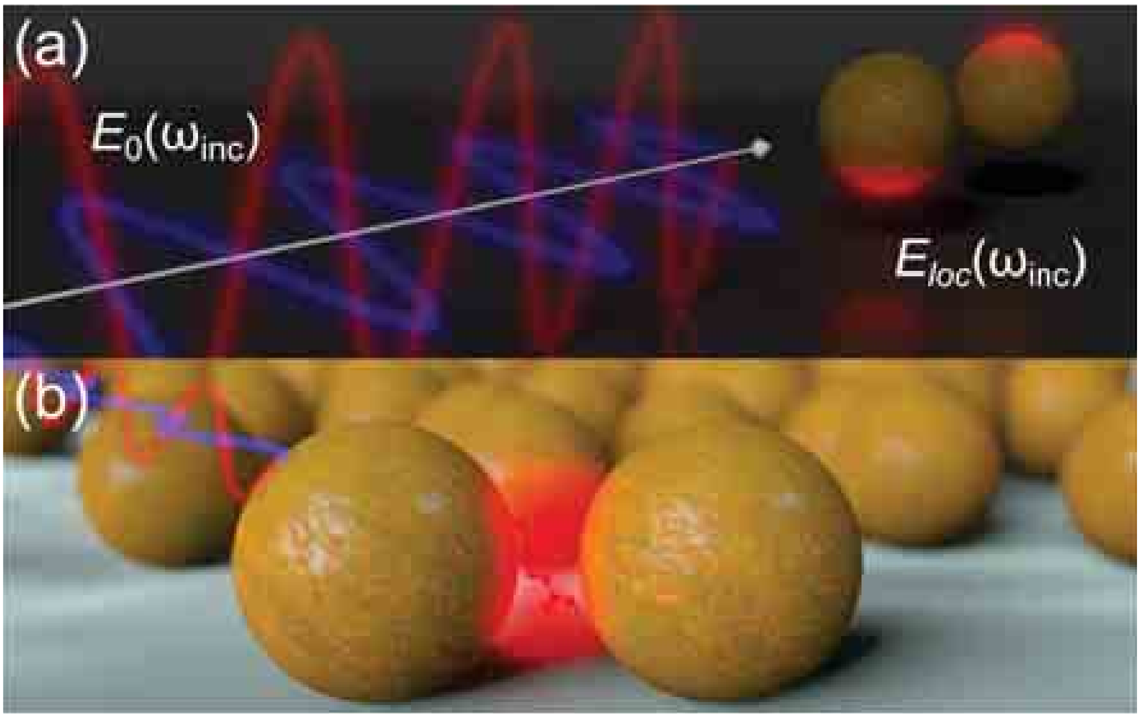

Figure 1.7. (a) Schematic representation of the induced electric dipole in two Au spheres by an incident electromagnetic radiation. Such a dipole can emit radiation at the same incident frequency but its amplitude is locally enhanced because of the interaction with the Au NPs. (b) Hot-spot formation between two Au spheres separated by a small distance. Molecules placed inside this area feel an electric field up to ten or more orders of magnitude higher than anywhere else.

The same way the laser induces an electric dipole moment in the spheres, $E_{loc}(\omega_{inc})$ induces a dipole in a molecule that is placed within a hot-spot or onto the surface of an individual particle. If α_{mol} is the polarizability tensor of the molecule, the induced dipole can be expressed as:

$$\mu_{ind} = \alpha_{mol} E_{loc}(\omega_{inc}) \qquad \textit{Equation 1.5}$$

If the molecule is vibrating at its own vibrational frequency ω_{vib}, inelastic scattering will occur and only three components of μ_{ind} will be possible: $\mu_{ind}(\omega_{inc})$, $\mu_{ind}(\omega_{inc} - \omega_{vib})$ and $\mu_{ind}(\omega_{inc} + \omega_{vib})$ which correspond to Rayleigh, Stokes and Anti-Stokes scattering, respectively. The final SERS intensity thus depends on both the incident and irradiated fields so that:

$$I_{SERS} = I_{inc}(\omega_{inc})I(\omega_{inc} - \omega_{vib}) =$$

$$= |E_{inc}(\omega_{inc})|^2|E(\omega_{inc} - \omega_{vib})|^2 \qquad \textit{Equation 1.6}$$

Since in many practical cases $\omega_{inc} \gg \omega_{vib}$, the expression for I_{SERS} becomes

$$I_{SERS} \approx |E(\omega_{inc})|^4 \qquad \textit{Equation 1.7}$$

which is known as $|E|^4$ *approximation*. The main message in equation 1.7 is that moderate enhancements in the local field lead to huge enhancements of the SERS field. Considering for example a local intensity 10^2 higher than the incident one ($E_{loc}/E_{inc} = 10^2$), the final SERS intensity will be $(E_{loc}/E_{inc})^4 = 10^8$. The term 10^8 is called *Enhancement Factor* (EF) and it expresses how intense is the local field as compared with the incident one.[34] A more general definition of EF comes from the comparison between SERS and Raman intensities and it is given by:

$$EF = \frac{I_{SERS}}{I_{Raman}} \cdot \frac{N_{Raman}}{N_{SERS}} \qquad \textit{Equation 1.8}$$

where *I* and *N* represent the intensities and average number of sampled molecules, respectively, in the corresponding Raman and SERS experiments. Equation 1.8 presents however a few problems. First of all the definition of N_{SERS} is not yet clear: for example in a planar substrate it is not defined whether N_{SERS} includes only the molecules adsorbed onto the surface of the metallic structure or also those adsorbed onto the non-metallic surface in between. In addition, in many cases the scattering volume (used for estimating N_{Raman}) is not well defined and calculating the exact metallic area is not straightforward especially for structures with complicated morphology. Finally, the excitation intensity is not uniform inside the scattering volume. Because of all these reasons additional definitions of EF have been proposed, even if Eq. 1.8 is most frequently used in literature.[35] The last consideration that it is worth mentioning is the distance dependence of I_{SERS}. Considering a point at a distance r from the center of the dipole, the electric field of the dipolar radiation is known to scale as r^{-3}, meaning that $I_{SERS} \sim r^{-12}$. In other words, SERS is a highly surface-sensitive technique and it allows to obtain information, apart from the nature of the chemical species adsorbed onto the substrate, about the orientation of the molecules relative to the surface normal.[34]

1.2.3 Chemical enhancement

The electromagnetic mechanism described in the previous paragraph is not the only effect involved during SERS scattering. Electric field enhancement and hot-spot formation are phenomena that would occur even in the absence of any analyte, they are only related to the optical and morphological properties of the metallic structures that are used. All other effects taking into account the interaction between the substrate and the adsorbate are known as *chemical enhancement* (CE). The nature of the CE is still subject of specific studies aimed to understand exactly the origin of this additional contribution to the overall SERS intensity. Probably one of the most common definitions of the CE given in the literature says:

> *"…is best thought to arise from the modification of the Raman polarizability tensor of the adsorbate, resulting from the formation of a complex between the adsorbate and the metal. Rather than an enhancement mechanism, the chemical effect is more logically to be regarded as a change in the nature and identity of the adsorbate."*[36]

Three main possible mechanisms for the CE have been proposed to exist:[37–41]

- ✓ The simplest model considers an adsorbate that is not covalently bound to the metal. In this case the electronic structure, and as a consequence the polarizability tensor, is only slight perturbed by the presence of the metal and this produces a small change in the SERS efficiency of a specific molecular vibration;

- ✓ When the analyte is covalently bound to the metal surface there is the possibility that it creates new electronic states in resonance with the laser and this leads to an enhancement of the Raman modes;
- ✓ The third hypothesis accounts for a photo-driven charge transfer between the analyte and the metal. In further detail, by changing the difference in energy between the adsorbate and the metal it is possible to trigger photo-driven charge transfer from the HOMO of the adsorbate to unoccupied states above the Fermi level in the metal (or from the LUMO to states that are slightly below the Fermi level).[3]

However, it is worth mentioning that the chemical contribution to the total enhancement is quite low (a factor ~10 in the best cases). All the SERS EFs are primarily electromagnetic and based on the LSPR of the metallic structure. The CE is crucial when the tiniest details of the process are studied but any realistic SERS application mainly focus on playing with the geometry of the metallic support in order to obtain the highest electromagnetic enhancement.

1.3 SERS substrates

As it can be deduced from the previous sections, the design of a SERS substrate that supports strong plasmon resonances and guarantees high amplification of the incident electric field is probably the most important task in SERS spectroscopy. There are several requirements that a SERS substrate should accomplish in order to be considered as a good choice: high EFs, uniformity of the signal all over its area, time-stability of the detection capability, easy to produce and, more important, to reproduce, mechanical stability and absence of background signal hindering the detection.[23,42]

Thanks to improvements in technology and knowledge, many efforts have been dedicated to the production of high-performance SERS substrates. Nowadays many techniques exist and they can be divided into two big categories: *top-down* and *bottom-up* approaches. The top-down approach relies on the use of several techniques like lithography, film deposition or laser and mechanical processing[43,44] to fabricate small structures on a large area through milling, etching and molding bulk materials into smaller features.[43–47] For instance, Sivashanmugan *et al.*[48] used focused ion beam (FIB) lithography to fabricate Au/Ag multilayered nanorod arrays as SERS active supports (Figure 1.8a). The substrate was the result of a two-step procedure: deposition of alternating Au/Ag layers by electron beam evaporation onto a silicon support was followed by FIB patterning at a constant power of 30 kV. The study was focused onto the detection of influenza A virus and reported that the SERS efficiency was significantly enhanced by increasing the thickness of the Ag layers. Another example of lithographic SERS support fabrication is given in Figure 1.8b. In this work, Wu and Dong[49] adopted an approach similar to the previous example but with a different final FIB pattern. Instead of Au/Ag they deposited a thin film of Al onto a glass slide and created an array of nanoholes with a specific diameter (150 µm in this case) and different periodicities.Working in resonance conditions they have been able to obtain en EF on the order of 10^6.

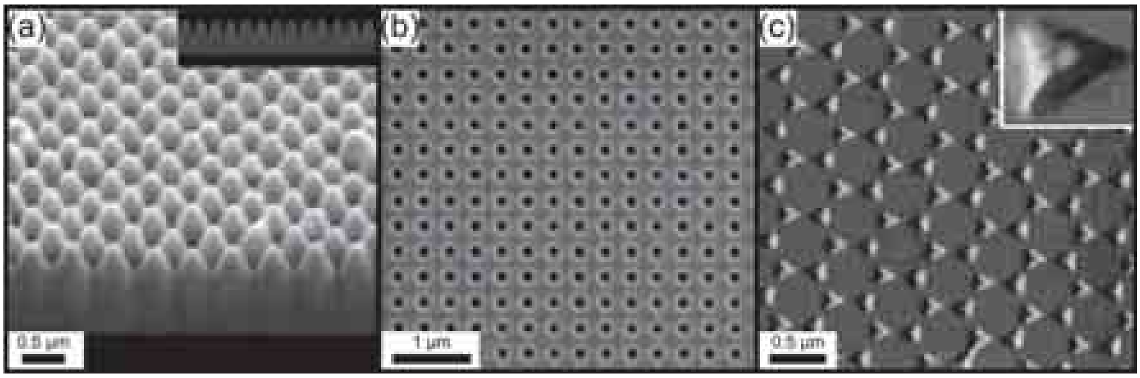

Figure 1.8. Examples of SERS substrates fabricated with top-down techniques: (a) standing Au/Ag multilayered nanorods, (b) nanoholes in an Al matrix and (c) ordered triangular Ag islands.[48–50]

The main advantages in using lithography are the high reproducibility and the large-area fabrication, rendering it suitable for industrial purposes. On the other hand, it presents quite a few drawbacks like high costs, low throughput and limited spatial resolution.[51]A widely used lithographic technique, which overcomes the high costs problem, is the so-called nanosphere lithography (NSL).[52] The idea behind NSL is to use self-assembled colloidal nanospheres as a mask to carefully control the subsequent deposition of a metal, typically by electron beam deposition. When the substrate orientation is normal to the deposition direction the result is a pattern made of uniformly spaced planar triangle-shaped NPs. By changing nanospheres size, density on the mask and deposition angle it is possible to create many different shapes.[53–55] A representative example in this field is the work of Haynes and Van Duyne,[50] shown in Figure 1.8c. By using a single layer of closely packed nanospheres as a mask, tip-to-tip Ag triangular platforms were created on the substrate once the spheres were removed. They also showed what happens when extra sphere layers are added to the first one. In the case of a double layer of nanospheres the result is an array of smaller hexagonal particles while with three layers the organization of the third one has to be taken into account: if the layers pack ABAB the particles have again hexagonal shape but if the packing is ABCABC all the mask holes are blocked and no particles are deposited.

The bottom-up approach is an alternative way to produce SERS substrates and it is the one that was used to fabricate all the samples in this thesis. In this approach, small units such as atoms, molecules and NPs were used to create larger systems by using different techniques such as chemical synthesis and self-assembly.[43,44] Because of their optical properties (see section 1.2.1), which make them optimal for SERS, the preparation of chemically stable Ag and Au NPs with different shapes and sizes has enormously improved and expanded. An incredibly wide variety of different geometries has been produced, including spheres,[56–58] rods,[59–65] stars,[66–70] prism and triangles,[71–77] wires,[78,79] shells,[80] cubes,[81,82] disks,[83] flowers,[84,85] dumbbells,[86,87] spiky dumbbells[88] and other geometries.[82,89–91] The TEM images in Figure 1.9 show some examples of NPs with different morphologies.

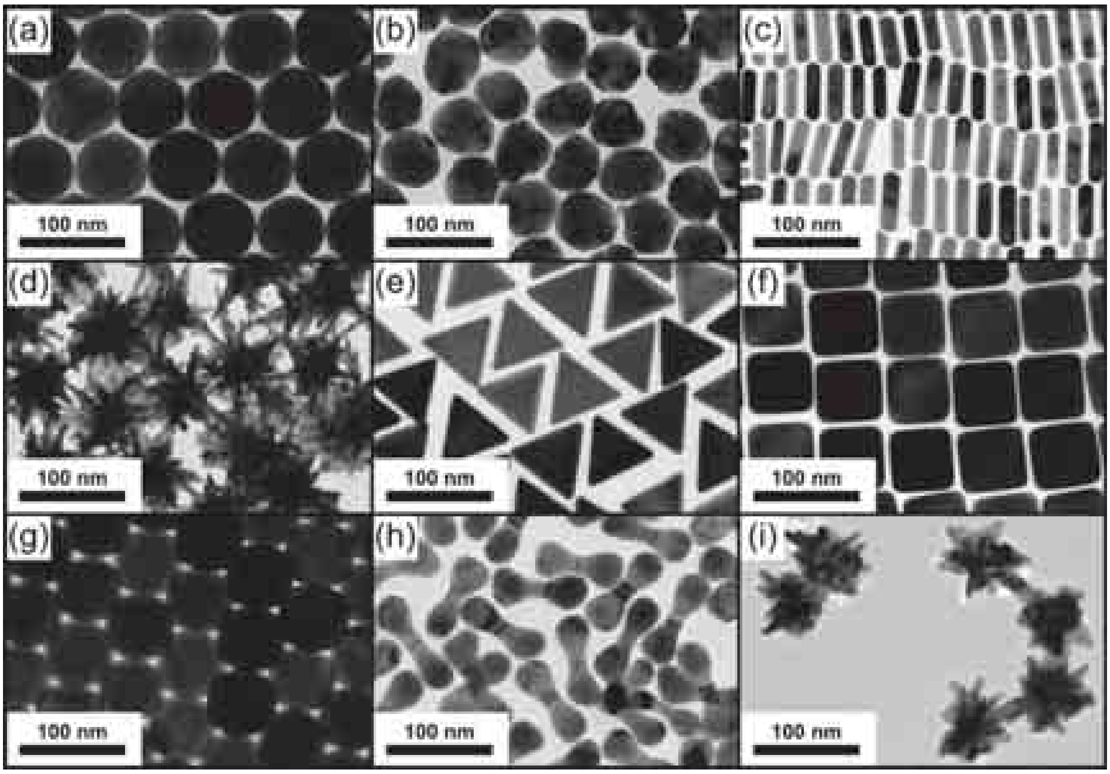

Figure 1.9. TEM pictures showing some examples of different morphologies of NPs that can be used in SERS experiments: (a) Au spheres, (b) Ag spheres, (c) Au rods, (d) Au stars, (e) Au triangles, (f) Au cubes, (g) Au octahedra, (h) Au dumbbells, (i) Au spiky dumbbells. All these NPs were synthetized at the Bionanoplasmonics Laboratory.

As we have seen above (section 1.2.1), the shape of the NPs determines their optical response to an incident electromagnetic field. In particular, NPs with sharp edges or tips are widely used in single particle SERS detection because of the extremely intense electric fields that can be produced in those areas. This effect is known as *lightning rod effect*. The synthesis of such spiky NPs allowed LFIEF of approximately 10^{10} for a single particle while the maximum LFIEF previously reported with a single Au NP was 10^4.[51,92] The bottom-up approach has several advantages related to low fabrication costs, easy procedures, scale-up of the synthesis, high control of shape, size and concentration, possibility to modify the surface chemistry and to work in different environments (e.g. organic and inorganic solvents). Among the numerous protocols proposed to obtain monodisperse NPs, the most common ones in the literature rely on the presence of a strong reducing agent that chemically reduces the metal salt (typically Au or Ag) and capping molecules preventing their aggregation after synthesis.[58,92–96]

Apart from the possibility to control the morphology of the individual NPs, bottom-up techniques like wet chemical synthesis and self-assembly allow a relatively precise control over the interparticle distance, which is important for the creation of hot-spots, either in solution and onto a solid support. The most common method to produce a SERS substrate is the direct drop-casting of NPs onto a support (like glass or silicon) but this does not allowto control NPs organization and therefore low reproducibility is often the main disadvantage. More reproducible and reliable SERS substrates are fabricated by exploiting the self-assembly driven by interactions between the NPs and the support. These interactions can have different nature: physical (electrostatic or capillary forces) or chemical (covalent bonding). For instance, highly ordered arrays of Au and Ag NPs were prepared by exploiting the strong chemical affinity of S, N and O for these two metals.[92,97–100] Typical self-assembly strategies are dip-coating, physical template-guided arrangement, spin coating, electrophoretic deposition and others.[97] An example of chemistry-driven self-assembly of NPs is the work of Gandra *et al.*[101], where plasmonic core-satellites structures were formed by exploiting the interaction between the surface of the Au NPs and chemical groups such as –SH and $-NH_2$ (Figure 1.10a). By playing with parameters like the surface charge of the NPs and the pH of the colloidal solutions, they were able to avoid the formation of core-core and satellite-satellite composites, resulting in a stable solution of core-satellite structures. They also demonstrated the possibility to form chains of core-satellite clusters with a resulting EF on the order of 10^8. Figure 1.10b illustrates an alternative method to produce SERS substrates: in this work, Gómez-Graña *et al.*[102] were able to obtain SERS-active plasmonic supercrystals made of core-shell Au@Ag NRs stabilized with a Gemini surfactant. They demonstrated that an accurate control over drop casting conditions (temperature and humidity) allows the formation of superlattices of standing Au@Ag NRs. High humidity and low temperatures were found to be the best conditions to form larger islands of standing Au@Ag NRs (~ 40 µm). The SERS efficiency of such substrates was then tested and compared to supercrystals made of Au NRs with no Ag shell. The comparison shows a 4 fold higher intensity for Au@Ag NRs, which confirms the superior enhancing capability of Ag as compared to Au. Interestingly, regions of standing NRs present a SERS intensity which is 2 orders of magnitude higher than that recorded in areas with randomly distributed NRs. This confirms the importance of the geometrical arrangement of the NPs within supercrystals.

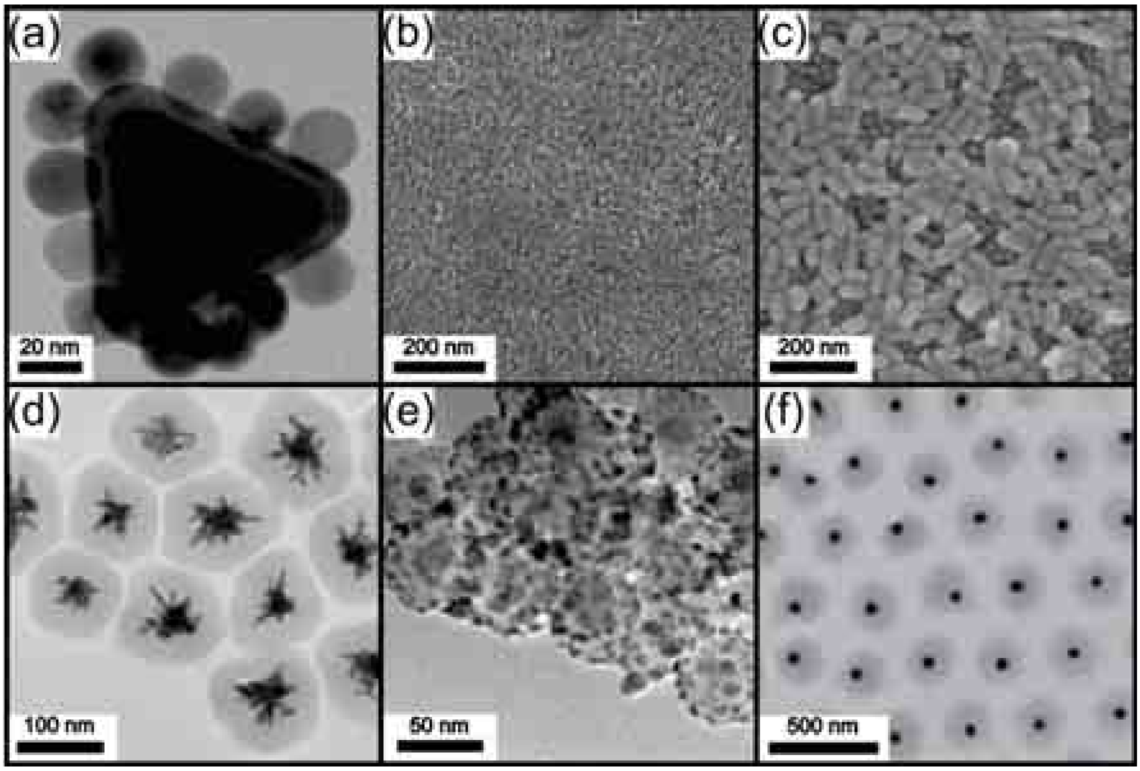

Figure 1.10. Different approaches for SERS-active substrates fabrication by exploiting the self-assembly of the NPs. (a) Core-satellite clusters, (b) standing Au@Ag NRs, (c) multilayered 3D structures, (d) silica-coated Au nanostars, (e) nanoshells with both magnetic and optical properties and (f) Au@pNIPAM NPs.[101–106]

In the work by Oh *et al.*[103] the arrangement of the layers in a multilayered structure was crucial (Figure 1.10c). By using Au nanospheres and NRs as building blocks for the layer formation, they showed interesting SERS response depending on the number of layers and their composition. The strongest SERS intensity for multilayered structures made of both spheres and rods was observed after a few layers of NPs and it was higher for NRs than for spheres. An interesting zigzag trend was found when spheres and rods were alternatively deposited on the substrate, this being consistent with previous results showing better SERS efficiency for NRs. By introducing a host layer inside a matrix of layers with different composition they also demonstrated that the 86% of the total SERS contribution comes from the first layer. Another approach in SERS substrates fabrication comprises covering the NPs with porous or thermoresponsive shells to improve colloidal stability and control the interaction between NPs and analyte. Silica-coated Au nanostars (NSs) were proposed by Fales *et al.*[104] as a promising support for diagnostic and therapeutic applications (Figure 1.10d). The silica shell allows the encapsulation of Methylene Blue (MB) around the gold core and improves the stability of the solution, this resulting in an enhanced reproducibility of the SERS analysis. Apart from the SERS application, this substrate was shown to be suitable for photodynamic therapy (PDT) because MB inside the shell is protected from degradation and can efficiently act as producer of singlet oxygen, which is the main cytotoxic reacting oxygen species used in PDT. Silica-coated AuNSs with MB produce a cytotoxic effect on BT549 breast cancer cells, which is not observed when silica-coated AuNSs without MB are used. Another example is represented by the hybrid approach used by Jun *et al.*[105] that combines both optical and magnetic properties of the building blocks (Figure 1.10e). The idea behind this hybrid solution is to improve the sensitivity of the system by magnetically inducing the aggregation of the plasmonic structures. In this case the final result was a colloidal solution made of core-shell plasmonic composites, each of them composed of one magnetite NP as core surrounded by a silica shell where Ag NPs were attached by thiol groups functionalization to enhance the incident electric field. After adding a Raman probe and inducing aggregation by applying a magnet, a second layer of silica was grown to make the aggregates physically and chemically more stable. This kind of system has been demonstrated to be suitable for cancer cell targeting, separation and imaging. The use of thermoresponsive shells around the NPs not only allows to trap the analyte but also gives the possibility to place it closer to the NP surface by tuning only the temperature of the system during the experiment. Álvarez-Puebla *et al.*[106] used poly-(N-isopropylacrylamide) (pNIPAM) microgel as thermally responsive medium to embed Au NPs (~ 67 nm), which were then further grown by additional reduction of $HAuCl_4$ (Figure 1.10f). The most interesting property of pNIPAM is the transition phase from a hydrophilic-swollen state to a hydrophobic-collapsed state when the temperature is below or above the critical value of ~ 32 ºC, respectively. The different results obtained for 1-Naphthalenethiol (1-NAT) and Nile Blue A (NBA) are consistent with their different chemical nature. While 1-NAT SERS signal remains constant over swelling-collapsing cycles, NBA efficiency increases or decreases depending on whether pNIPAM is collapsed or swollen, respectively. Since 1-NAT covalently binds to Au, lowering or increasing the temperature does not make any difference because the analyte is bound in any case to the NP surface. NBA, on the other hand, has a lower affinity for Au surfaces and is larger in size comparing with 1-NAT, resulting in a restricted diffusion through pNIPAM and, as a consequence, in a different behavior depending on temperature.

All the considerations made in this chapter aimed at providing a general overview over the theoretical aspects of SERS spectroscopy and the state of the art in the fabrication of reliable SERS substrates. Even though many improvements have been reached during the past decades, the fabrication of SERS substrates is still a field in which many efforts need to be done to guarantee best performance in terms of uniformity, stability and reproducibility.

CHAPTER 2

GOLD NANOWIRE FORESTS FOR SERS DETECTION

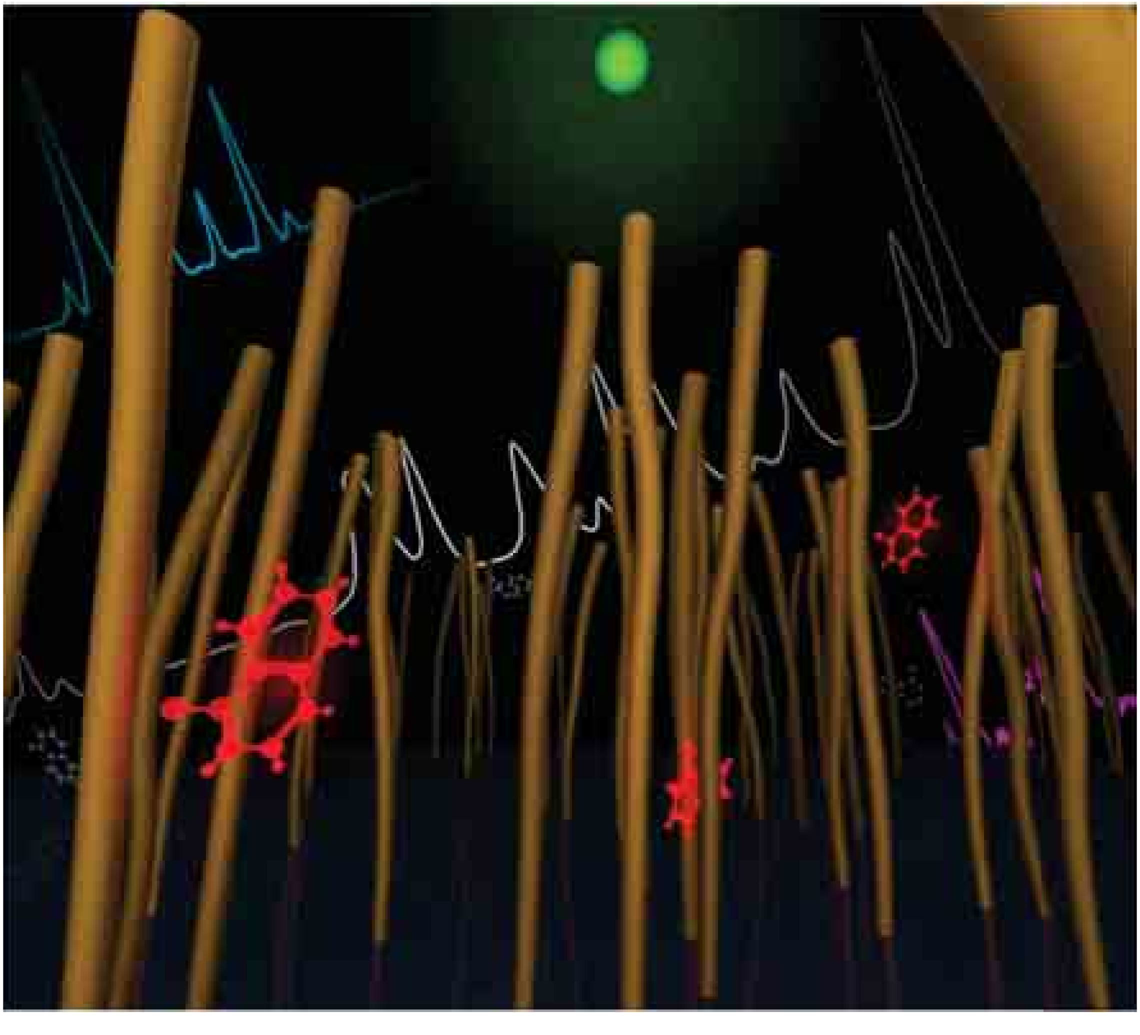

Abstract

Simple wet chemistry has been applied to control the vertical growth of gold nanowires (AuNWs) on a glass substrate. As a consequence, longitudinal localized surface plasmon resonances could be tuned from 656 to 1477 nm in few minutes by simply controlling the growth rate and time. This process allowed us to select the optimum conditions for maximum electromagnetic enhancement and performance in surface enhanced Raman scattering (SERS) detection. SERS measurements confirmed the uniform and reproducible distribution of the NWs on the substrate, with the subsequent high reproducibility of hot spot formation. Detection of malachite green in water and of 1-naphthalenethiol from the gas phase were demonstrated as proof-of-concept applications of these three-dimensional SERS substrates.

2.1 Introduction

Surface enhanced Raman scattering (SERS) is a powerful analytical tool, mainly based on the interaction of the high electromagnetic fields generated at the surface of metal nanostructures when illuminated at their corresponding localized surface plasmon resonances (LSPRs). Such enhanced near fields are typically favored at small gaps between nanoparticles (NPs), which are known as hot spots.[107–109] Recent progress in metal processing techniques and in colloid chemistry methods has driven a large amount of research focusing on the fabrication of high-performance SERS substrates and their application in various fields.[110–118] NPs with a wide variety of shapes have been used to create substrates with a high density of hot-spots, reaching enhancements of the Raman signal by many orders of magnitude.[119–125] The main challenge regarding the fabrication of SERS substrates however concerns their uniformity and reproducibility. One of the most studied methods to create hot spots is the self-assembly of metallic NPs (bottom-up approach) and many efforts are being spent to reach a suitable control over this technique. Recent examples include the self-assembly of Au[99] and Au@Ag[121] nanorods into supracrystals, which have been applied to the detection of scrambled prions and other bio-relevant molecules. In a related report, Zhu *et al.*[126] demonstrated the detection of Microcystin LR (MC-LR), a toxin produced by an algae, exploiting the electric field enhancement occurring at the hot spots of an end-to-end assembly of gold nanorods. In particular they detected the SERS signal of the probe molecule 4-aminothiophenol (4-ATP), which is highly dependent on the MC-LR concentration in solution. Zheng *et al.*[127] used directed self-assembly of DNA-functionalized spherical particles of different sizes to create a core-satellite plasmonic structure and fabricate a reproducible SERS substrate. By changing Au NPs concentration and the number of DNA chains per NP they were able to control the distance between each core Au NP and, as a consequence, the optical properties of the substrate. SERS experiments showed a limit of detection of 10^{-9} M for benzenethiol.

Alternatively, top-down methods, including focused ion beam (FIB) and electron beam lithography (EBL), have been used to deposit nanostructures on solid substrates with high precision, thereby controlling NPs size and shape, as well as interparticle distance.[128–133] These fabrication methods opened new possibilities to realize highly ordered and reproducible SERS supports. Examples include the work by Wells *et al.*,[134] who fabricated "isolated" nanopillars by using a combination of EBL, metal mask lift-off patterning and reactive ion etching (RIE). SERS measurements of a thin layer of zinc phthalocyanine (ZnPc) showed that the SERS enhancement largely depends on the physical features of the nanopillars, such as height, diameter and shape. Nanopillars have also been fabricated by Boisen *et al.*[135] by using a maskless approach. In this work they exploit the bending capability of standing nanopillars to create hot spots and achieve picomolar SERS detection. However, next to these advantages top-down approaches also present certain drawbacks such as the need for very sophisticated equipment and high cost. This represents an important limit in the large scale fabrication of substrates, which may be overcome by improving the control over the relatively inexpensive self-assembly approaches.

In this chapter we present a simple and highly reproducible procedure to control the optical response of AuNWs, vertically grown on top of a silanized glass support. A high control over the LSPR of the NWs was achieved by tuning growth time, which allowed us to tailor the resonance wavelength of the collective Au NW plasmon band with good accuracy, within the near infrared (NIR) region. The growth of Au NWs is demonstrated to be homogeneous over the whole glass surface, and to provide a large enhancement of the SERS signals of mercaptobenzoic acid (MBA), used during the synthesis. Removal of MBA from the Au NWs resulted in highly efficient SERS substrates for the detection of malachite green (MG), a carcinogenic and antibacterial compound.[136–139] Plasma cleaning allowed us to recycle the substrates and we also demonstrate the possibility to detect molecules from the gas phase by using 1-naphthalenethiol (1-NAT) as a volatile probe.

2.2 Results and Discussion

The growth of vertical Au NWs on glass substrates was based on the method recently reported by He *et al*.[140] This method comprises three steps: glass functionalization with an aminosilane (aminopropyltriethoxy silane, APTES), seed self-assembly and seeded growth. The key element behind the preferential anisotropic growth perpendicular to the substrate is likely related to the use of MBA to functionalize the Au NP seeds upper surface, which is not possible on the lower part because of the presence of APTES binding the NP to the glass surface. This results in the reduction of Au(III) only at the bottom side of the seeds, which act as catalysts. As a consequence, each seed is lifted up from the glass and the reduced gold atoms are covered by MBA molecules present in solution, thereby forcing the reduction to occur always at the bottom side. Whereas the diameter of the NWs depends on the ratio between MBA and Au(III) in solution, their length can be readily controlled through the growth time. The resulting increase in the aspect ratio was readily observed through changes in the vis-NIR spectra (Figure 2.1a). As the NWs grow longer, red-shift and broadening are observed in the plasmon band, with a new band developing after 4-5 min. After 10 min of NW growth, two distinct bands can be appreciated, one centered around 600 nm and a broader one around 1500 nm. Although the bands become very broad after Au NW growth, this process proved to be highly reproducible, as shown in Figure 2.1b, where the maximum positions of the low energy bands are plotted vs. growth time for three different synthesis series, each comprising seven substrates that were grown for different times.

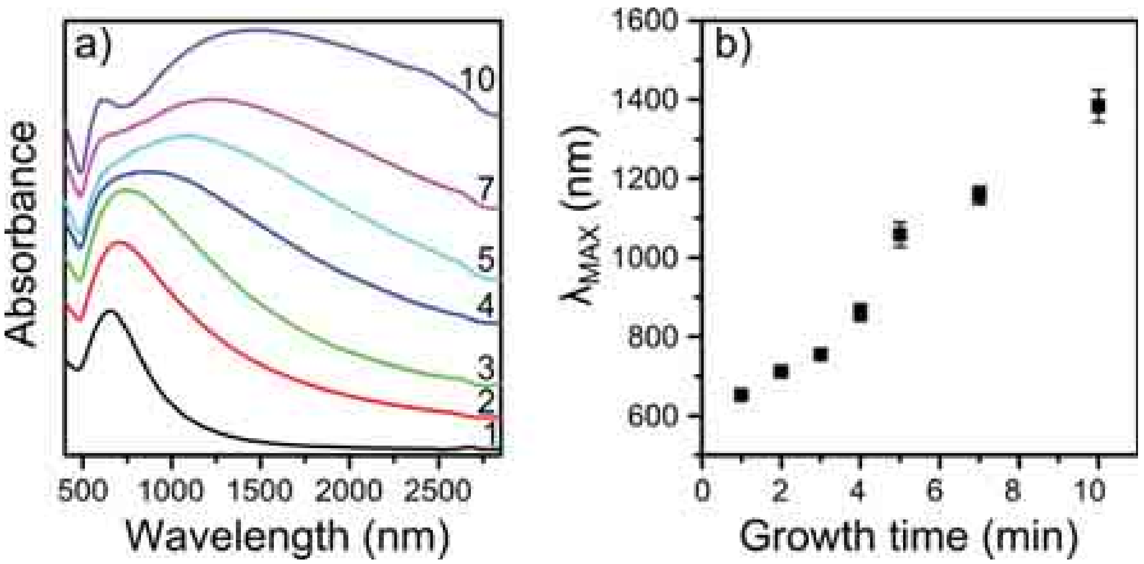

Figure 2.1. (a) Absorbance spectra of Au NWs for different growth times as labeled (min). (b) Wavelength of the maximum of the lower energy plasmon band, as a function of growth time. Each point is the result of an average over three different substrates and the error bar indicates high synthesis reproducibility.

The LSPR spectra in Figure 2.1a show the effect of plasmon coupling between individual NWs. Interestingly, the LSPR of (non-coupled) NWs in solution (not shown) shows a red-shifted longitudinal band, which is in agreement with the results by Funston et al.[141] for side-by-side aligned nanorods. The NWs substrate used in our work can be considered as many side-by-side aligned NWs, so that by changing the growth time it is possible to control not only the LSPR of the individual NWs but also their collective coupling behavior. It is important to highlight that the growth solution used for the synthesis always consisted of freshly-prepared MBA and ascorbic acid stock solutions, meaning that changes arising from potential errors in this preliminary step do not appear to affect NW growth. From Figure 2.1a it is however not perfectly clear at which point of the synthesis the nanowire shape starts to develop. Indeed, for growth times up to 3 min a single plasmon band is visible in the spectrum. TEM was used to analyze the formed particles, upon detachment from the substrate (see Experimental for details). The electron micrographs show that already after one minute of growth anisotropic nanoparticles are formed but with rather undefined shapes (Figure 2.2). After 2 min the aspect ratio has increased and a rod-like morphology is clearly observed, whereas after 3 min NWs have definitely been formed.

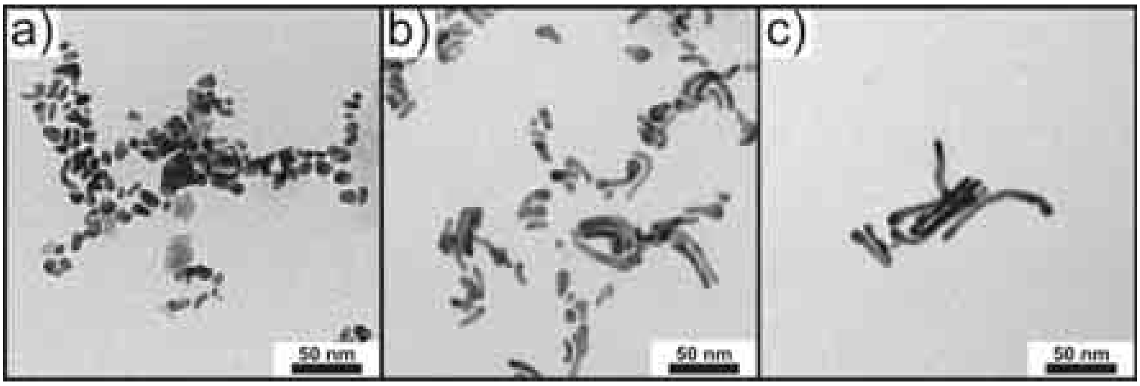

Figure 2.2. TEM micrographs of particles obtained for different growth times. After 1 min the NPs still have undefined shapes (a), whereas they display rod- and wire-like shapes after 2 (b) and 3 min (c), respectively.

Systematic experiments evidenced that the growth rate can be controlled by varying the amounts of Au(III) and MBA in the growth solution while keeping a constant molar ratio between them. Another important factor influencing the overall growth rate is the number of seeds acting as catalysts: at fixed [Au(III)]/[MBA] ratio, increasing the seed density on the substrate leads to slower NW growth because of a lower amount of Au(III) per seed. This is an important issue in terms of reproducibility in NW length.

Figure 2.3a-c shows SEM images of three substrates grown for 3, 7 and 10 min, displaying the resulting density of NWs on the glass substrate, as well as their tendency to bend and form bundles. Details about the dimensions were obtained from TEM images as shown in Figure 2.3d-f. The average diameter does not vary during growth and is determined by the MBA/Au(III) molar ratio in the growth solution (0.48 in these samples) and it was determined to be 5.34 ± 0.76 nm. Statistical analysis revealed that after 3, 7 and 10 minutes the NW lengths were 68 ± 9, 198 ± 26 and 334 ± 47 nm, respectively.

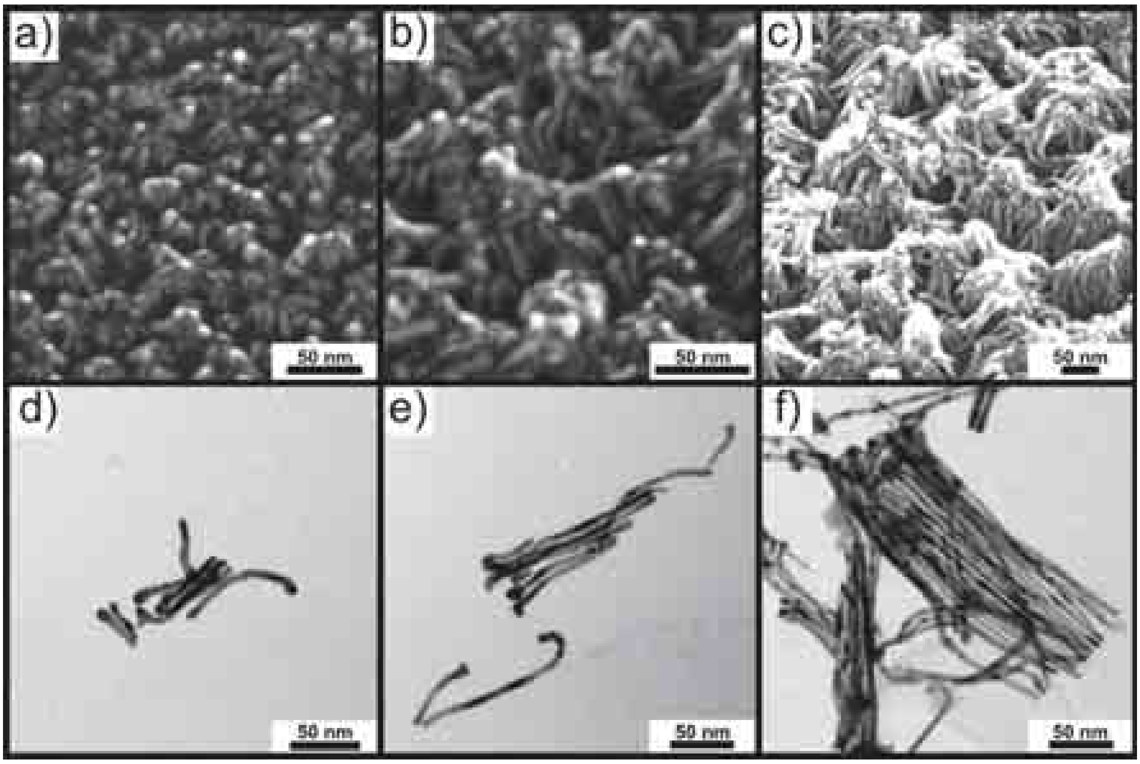

Figure 2.3. (a-c) SEM images of Au NWs on glass after growth times of 3 (a), 7 (b) and 10 min (c). (d-f) Corresponding TEM images of Au NWs from the same substrates.

The SERS efficiency and reproducibility of the substrates was evaluated by preparing three different series of samples and measuring the MBA SERS signal corresponding to the ν(C-C) mode[142] at 1075 cm^{-1} for each of them (Figure 2.4a). The observed trend was the same for all series and the maximum SERS intensity was always recorded for the substrates that were grown for 4 min, though almost no difference was observed when comparing 3, 4 and 5 min growth. The plasmon band for these substrates was centered around 740 nm, which is in close resonance with the laser wavelength used for SERS excitation (785 nm). Therefore, we decided to use these growth conditions in all subsequent experiments.

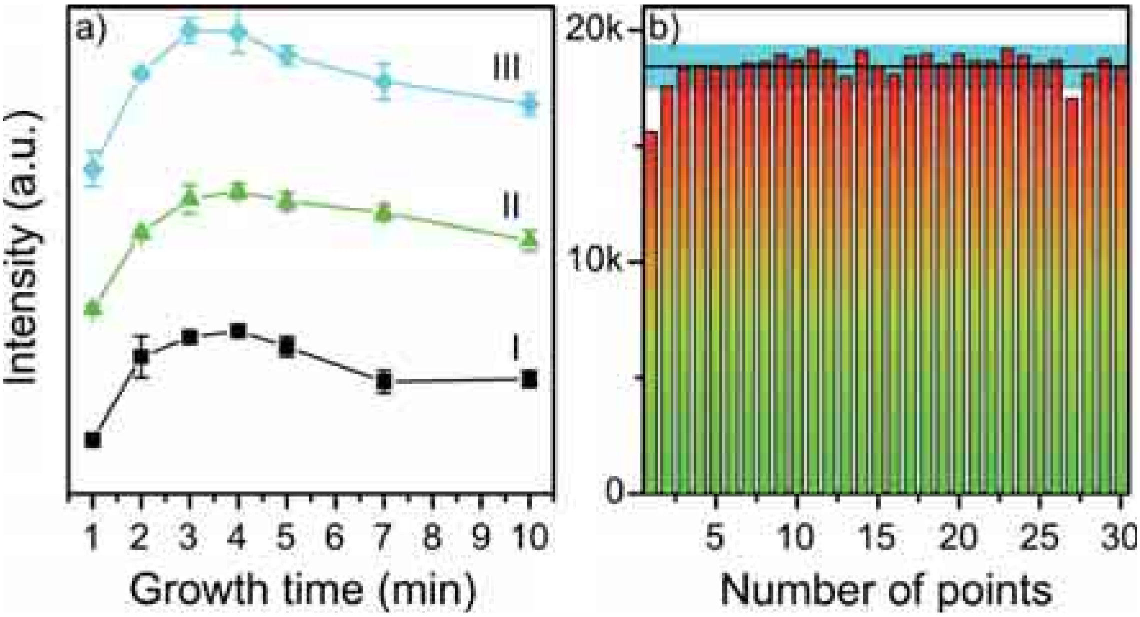

Figure 2.4. (a) SERS intensity (1075 cm^{-1} MBA peak) versus growth time: the maximum enhancement of the signal occurs with NWs grown for 4 min. Each point is the average intensity of three different areas in the substrate. (b) Statistics of the measured SERS scattering intensity (1075 cm^{-1} MBA peak) at 30 different points of a substrate. The black line represents the average value. Almost all of them are within 10% fluctuation from the average value (light blue area).

The high uniformity of the samples was demonstrated by recording MBA SERS spectra at 30 different spots covering the whole area of the same substrate (1 cm^2) and performing a statistical analysis of the results (Figure 2.4b). Remarkably, almost all the points fell into the light blue area in Figure 2.4b, which represents a fluctuation of ±5% from the mean value. To optimize the performance of a SERS substrate, it is important to fully exploit the enhanced near field, which is created in close proximity to the NWs surface.[143] To facilitate access of the analytes to the NWs surface, we used Ar$^+$ plasma cleaning to remove the MBA organic layer covering the NWs, which plays a key role during the synthesis process. As shown in Figure 2.4a, after Ar$^+$ plasma cleaning, no significant changes were observed in the UV-Vis spectrum, while the efficiency in removing MBA from the surface was confirmed by measuring the MBA SERS signal before and after cleaning (Figure 2.4b): all the SERS peaks disappeared, meaning that the resulting NWs surface was free of MBA molecules.

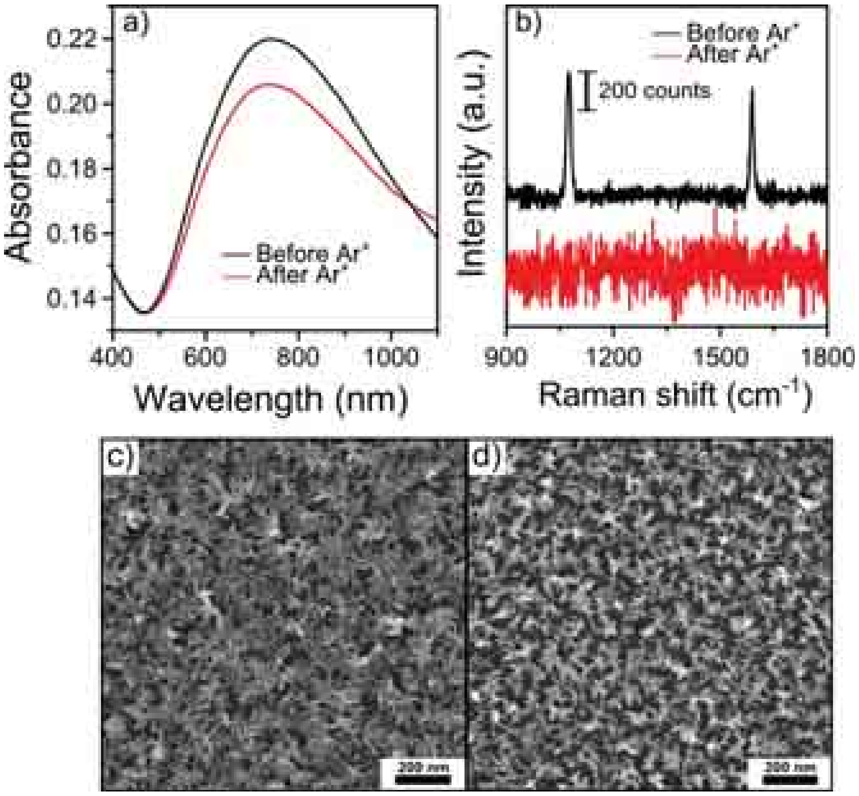

Figure 2.4. (a,b) UV-Vis and SERS spectra of an Au NW substrate before and after Ar^+ plasma cleaning: no significant changes are observed while complete removal of MBA from the Au surface is confirmed by the loss of MBA SERS signal. (c,d) SEM images of Au NWs before (c) and after (d) plasma treatment (4W, 10 mTorr, 6 minutes).

SEM analysis after Ar^+ plasma treatment (Figure 2.4c,d) revealed that the NWs were only slightly modified by the plasma, while keeping their morphology and 3D organization. The resulting MBA-free NWs were tested as SERS substrates for the detection of malachite green (MG). MG is an organic dye, which has an effective fungicide effect that is widely used in fish farms, in the aquaculture industry and in freshwater aquaria. However, the use of malachite green is rather controversial due to its genotoxic and carcinogenic nature and it is banned in several countries.[144] Figure 2.5a shows the recorded MG SERS spectra after dipping the sample in aqueous solutions containing different concentrations of MG, down to 10^{-6} M. By plotting the average intensity of the C-C stretching peak at 1618 cm^{-1} as a function of MG concentration (Figure 2.5b), we find that the peak intensity reaches a plateau around 0.5 mM MG, which is an evidence behind complete NWs coverage by MG molecules.

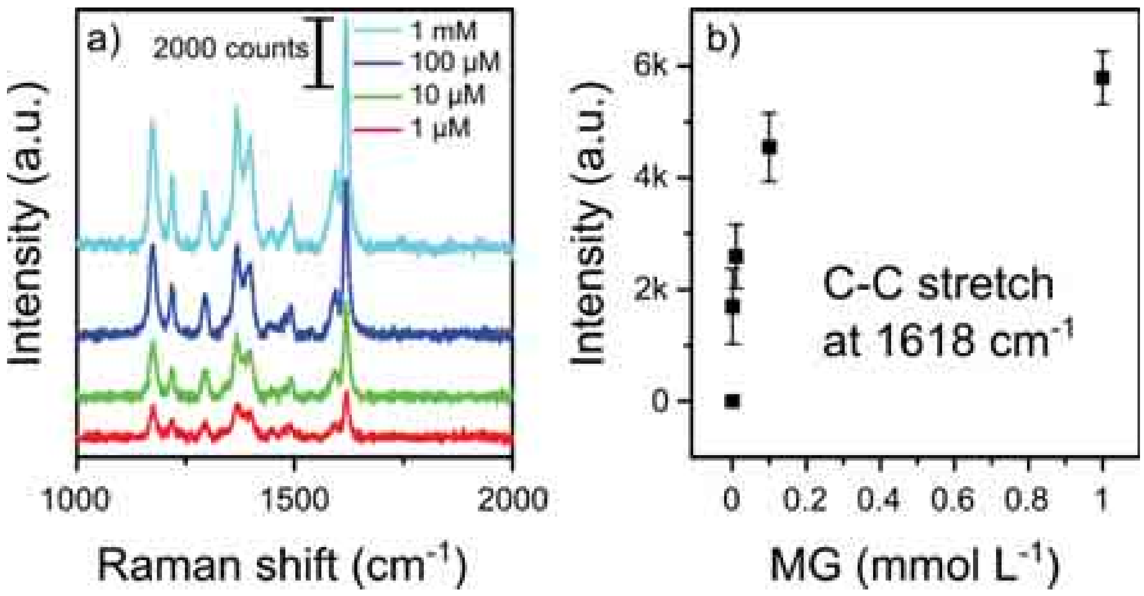

Figure 2.5. (c) SERS spectra of MG at different molar concentrations: the characteristic MG peaks are clearly visible down to 10^{-6} M. (d) Intensity of the C-C stretching peak vs. MG concentration. Data in C and D are averages from 3 measurements.

Since plasma cleaning has been shown to remove adsorbed molecules from the AuNWs with no significant alteration of their morphology and optical response, we tested reusability of the substrates for detection of different analytes. Thus, after MG sensing, the same substrate was used to detect 1-NAT and Rhodamine 6G (R6G), and the results are shown in Figure 2.6. MBA was first removed (Figure 2.6a) and MG was absorbed and detected by SERS (Figure 2.6b). A second Ar^+ plasma cleaning treatment was then applied to remove MG and 1-NAT was allowed to absorb onto the Au NWs surface (Figure 2.6c). Finally, a third plasma cleaning step enabled the detection of R6G (Figure 2.6d).

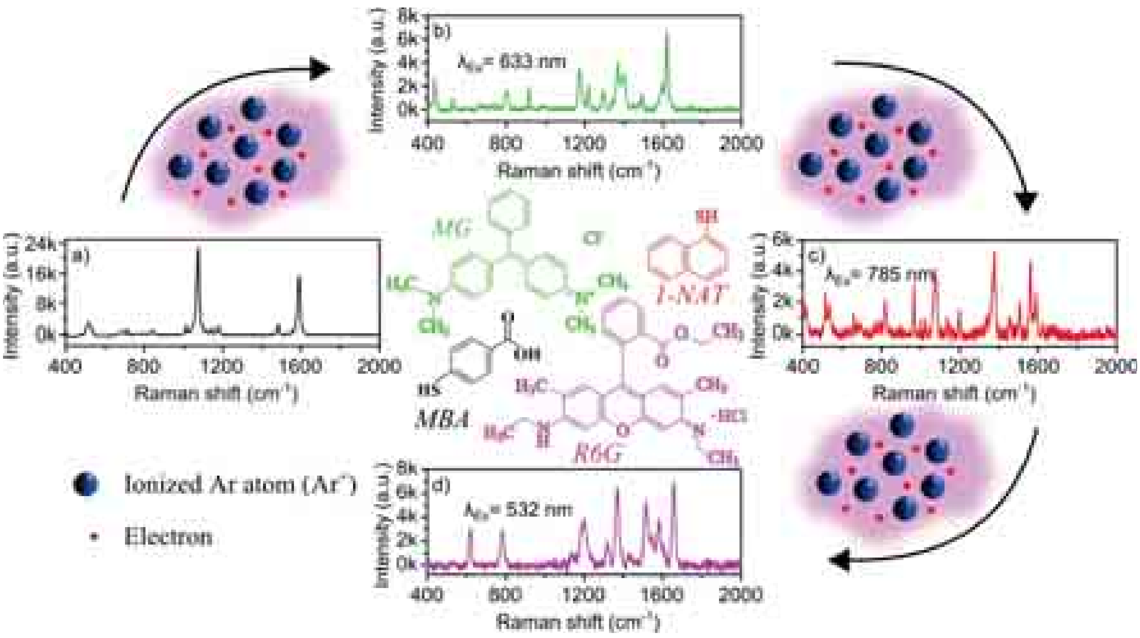

Figure 2.6. Illustration of a detection cycle of MG, 1-NAT and R6G upon removal of MBA molecules from the Au NWs substrate. (a) SERS spectrum of MBA right after the synthesis. (b-d) SERS spectra of MG (b), 1-NAT (c) and R6G (d) after successive Ar^+ plasma cleaning and dipping the substrate in the corresponding solution. Dipping time was 1h for all the samples.

In each SERS spectrum all the main features of the corresponding analyte were visible: ν(C-C) and ring-breathing at 1075 and 1589 cm^{-1} for MBA,[142] δ(C-H) and ν(N-Φ) for MG,[145] δ(C-H) and ring stretch for 1-NAT,[146] ν(C-C) and ν(C-N) for R6G.[147] Complete band assignment is provided in Table 1.

Table 1. Characteristic Raman scattering frequencies (cm^{-1}) of 4-Mercaptobenzoic Acid (MBA), Malachite Green (MG), 1-Naphtalenethiol (1-NAT) and Rhodamine 6G (R6G)

MBA	Vibrations	MG	Vibrations	1-NAT	Vibrations	R6G	Vibrations
1075	ring breathing	435	op ring deform.	515	ip ring deform.	620	ring bending
1142	ip δ(C-H)	526	ip ring deform.	536	ip ring deform.	781	op δ(C-H)
1180	ip δ(C-H)	914		661	ip ring deform.	1316	ν(C-C), ν(C-N)
1479	ring bending	1173	ip δ (C-H)	791	ip ring deform.	1370	ν(C-C), ν(C-N)
1589	ν(C-C)	1218	ν(N-C), δ(C-H)	817	ring breathing	1512	arom ν(C-C)
		1292	ipm C-C, ipm C-C-H	964	ring breathing	1580	arom ν(C-C)
		1366	ν(N-Φ)	1023	ip δ(C-H)	1654	arom ν(C-C)
		1398	ipm C-C, ipm C-H	1074	ip δ(C-H)		
		1491	δ(N-R_1), N-R_1 rock	1134	ip δ(C-H)		
		1594	ip ring stretch and bend	1196	ip δ(C-H)		
		1617	ν(N-Φ), ν(C-C)	1332	ip ring stretch		
				1377	ip ring stretch		
				1455	ip ring stretch		
				1505	ip ring stretch		
				1559	ip ring stretch		
				1588	ip ring stretch		

ip = in plane, ipm = in plane motion, op = out of plane, Φ = phenyl ring, R_1 = $(CH_3)_2$, arom = aromatic

The corresponding UV-Vis spectra at each step (Figure 2.7) revealed some broadening after the first plasma cleaning process, but no significant variations until the end of the entire cycle.

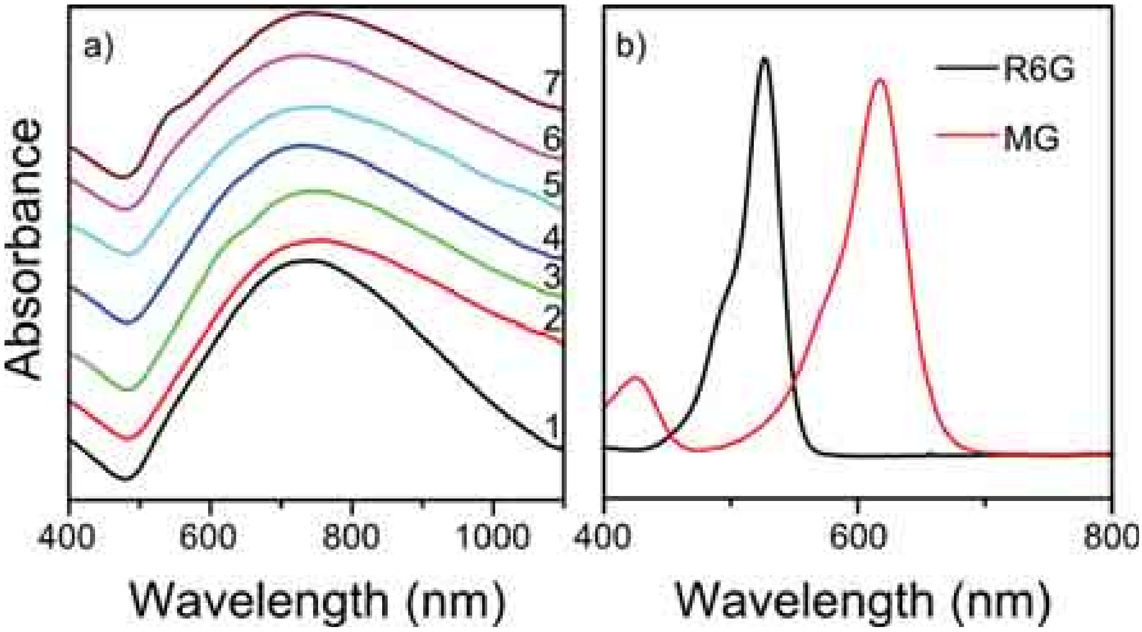

Figure 2.7. (a) UV-Vis spectra of the sample: before Ar^+ irradiation (1), after Ar^+ plasma cleaning (2), after MG adsorption (3), after second Ar^+ plasma cleaning (4), after 1-NAT adsorption (5), after third Ar^+ plasma cleaning (6), after R6G adsorption (7). The shoulders in 3 (~622 nm) and 7 (~535 nm) are due to the adsorption by MG and R6G, respectively. The corresponding absorption spectra of R6G and MG are shown in (b).

Further application of the substrates was found for detection from the gas phase, using 1-NAT as Raman probe. A simple experimental setup was designed as shown in Figure 2.8a. A 25 mL plastic tube was used as a chamber in which the substrate was fixed to the inner side of the cap, while single drops (25 μL) of 1-NAT solutions in ethanol at selected concentrations were deposited on the bottom of different tubes. The SERS spectra in Figure 2.8b confirm the detection of the volatile 1-NAT, down to a concentration of 10^{-3} M in the liquid drop. The adsorption of 1-NAT on the AuNWs forest could be monitored by registering the SERS peak intensity at 1559 cm^{-1}, as a function of time. As expected, the SERS intensity increased with time (Figure 2.8c), indicating the gradual evaporation of 1-NAT from the drop until the AuNWs surface was saturated. It is important to note that 10^{-3} M is the concentration of 1-NAT in the liquid, so the maximum concentration of 1-NAT in the 25 mL tube volume would be 10^{-6} M, assuming that all the molecules in the drop are evaporated. Additionally, part of the molecules are expected to adsorb onto the tube walls, not contributing to the internal pressure. At this upper limit of 1-NAT concentration, saturation of the SERS signal was reached after 50 min.

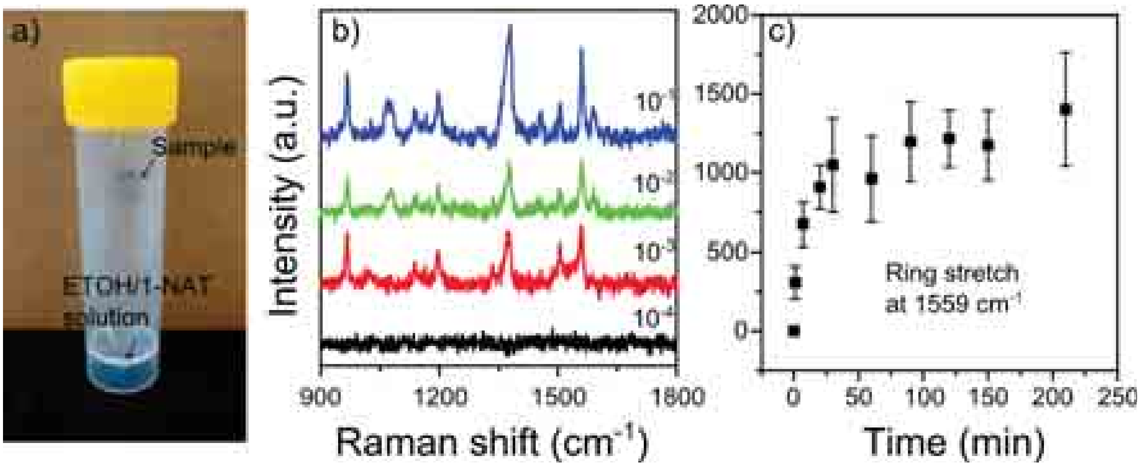

Figure 2.8. (a) Illustration of the experimental setup for gas phase detection: after Ar^+ cleaning the substrate was attached to the cap of a 25 mL tube containing an EtOH/1-NAT solution (25 µL). (b) SERS spectra measured for different 1-NAT concentrations inside the tube: typical features of 1-NAT spectrum are distinguishable down to 10^{-3} M. (c) Intensity of the ring stretching peak at 1559 cm^{-1} vs. time: saturation was reached at around 50 min incubation time.

2.3 Conclusion

We have demonstrated a simple and highly reproducible method for the vertical growth of densely packed AuNWs on APTES-functionalized glass slides, which allows fine tuning of the LSPR response in the NIR. This optical control allowed us to tune the plasmon band in the proximity of the excitation laser wavelength used for SERS measurements, thereby achieving high electric field enhancements at the surface of the NWs. MBA can be completely removed from the substrates by plasma cleaning without damage of the nanostructure, allowing its use as a sensor, which was demonstrated through the detection of MG in aqueous solution with a limit of detection of 10^{-6} M. We also demonstrated the reusability of the sensor by successive plasma cleaning after detection of each analyte. We were thus able to detect MG, 1-NAT and R6G by recycling the same substrate. As a final application of this system, gas sensing efficiency was demonstrated by detecting 1-NAT evaporated from solution. This is thus a robust and highly versatile system that can be implemented for multiple detection uses. The detection efficiency might however be improved by using an infrared laser source which couples to LSPRs of longer Au NWs.

2.4 Experimental Section

Chemicals. (3-Aminopropyl triethoxysilane, APTES, ≥98%), sodium borohydride ($NaBH_4$, 99%), gold(III) chloride trihydrate ($HAuCl_4$, ≥99.9%), 4-mercaptobenzoic acid (MBA, 90%), L-ascorbic acid (≥99%), sodium citrate tribasic dihydrate (≥98%), Malachite Green Chloride (≥96%), 1-Naphthalenethiol (99%), and Rhodamine 6G (95%) were all purchased from Sigma-Aldrich. Hydrogen peroxide (H_2O_2, 35% w/w) and sulfuric acid (H_2SO_4, 96%) were purchased from Scharlab and Panreac, respectively. Glass slides (24×24 mm^2) were purchased from Menzel-Gläser.

Characterization. Optical extinction spectra were recorded using an Agilent 8453 UV-Vis diode-array spectrophotometer. UV-Vis-NIR spectra were collected using a scanning spectrophotometer Cary5000. The samples were treated with Ar^+ plasma using AJA-ATC 1800 UHV Magnetron Sputtering. SERS spectra were recorded using a Renishaw Invia Raman microscope equipped with two Peltier-cooled CCD detectors, a Leica microscope two gratings with 1200 and 1800 lines/mm and band pass filter optics. Excitation lasers with emission wavelengths of 785, 633 and 532 nm were used and focused onto the sample through a 100× objective with N.A. 0.85, this producing a spot size of 923, 745 and 626 nm^2 for 785, 633 and 532 nm, respectively. The SERS spectra were collected with an integration time of 10 s and the samples were irradiated with constant powers of 1.2 mW (785 nm), 0.05 mW (633 nm) and 0.1 mW (532 nm). Transmission electron microscopy (TEM) images were collected with a JEOL JEM-1400PLUS instrument operating at 120 kV. Scanning electron microscopy (SEM) was measured with a Dual beam FIB – FEI Helios 450S microscope with electron column resolution of 0.8 nm at 20 kV.

Syntesis of Au seeds. An aqueous solution (20 mL) containing $HAuCl_4$ (1.25×10^{-4} M) and sodium citrate (2.5×10^{-4} M) was heated up to 50 ºC and a freshly prepared $NaBH_4$ solution (300 µL, 10^{-2} M) was added under vigorous stirring. After 30s stirring was slowed down and maintained for 15 min. The UV-Vis spectrum of the solution showed an absorbance band at 509 nm.

Preparation of the substrates. Each glass slide was first treated with piranha solution (H_2SO_4/H_2O_2 3:1) for 60 min, then rinsed with abundant distilled water and dried under with N_2. The substrates were then immersed in an APTES/EtOH solution (5% v/v) overnight. After washing with ethanol to remove excess APTES and drying under N_2, they were soaked in the seed solution for 60 min, followed by rinsing with distilled water and drying under N_2.

AuNWs Synthesis. The seed-functionalized part of the glass was immersed in a growth solution in EtOH/H_2O (3:1 v/v) containing MBA (412 μM), $HAuCl_4$ (860 μM) and ascorbic acid (2 mM). After the addition of ascorbic acid the stirring was maintained for few more seconds to mix all the components and then turned off. To stop the growth at any point during the synthesis the substrate was extracted from the solution, washed with ethanol[33] to remove unbound MBA and dried under N_2.

Preparation of TEM grids. NWs were extracted into solution by washing the substrate with ethanol after growth, then soaking it in milli-Q water and immersing in a sonicator bath for 15 min. Important: the sample should not be allowed to dry after washing. The NWs were then centrifuged and redispersed in milli-Q water, several drops were casted on the grid and dried in air.

Detection in solution. Each sample was exposed to Ar^+ plasma cleaning (4W, 10 mTorr of Ar inside the sputtering chamber) for 6 min. Cleaned samples were cut into stripes (~0.7 cm) and dipped in MG solutions with different concentrations for 1h. For the successive detection of MG, 1-NAT and R6G, the cleaning/dipping steps were repeated three times.

Gas sensing. To ensure a closed environment during gas detection, the samples were fixed inside 25 mL plastic tubes containing drops of 1-NAT solutions in ethanol at different concentrations. Regarding the saturation curve, 10 samples were placed in 10 different tubes, all containing a 1-NAT drop (10^{-1} M) and extracted after selected times.

CHAPTER 3

PEN-ON-PAPER APPROACH TOWARD THE DESIGN OF UNIVERSAL SURFACE ENHANCED RAMAN SCATTERING SUBSTRATES

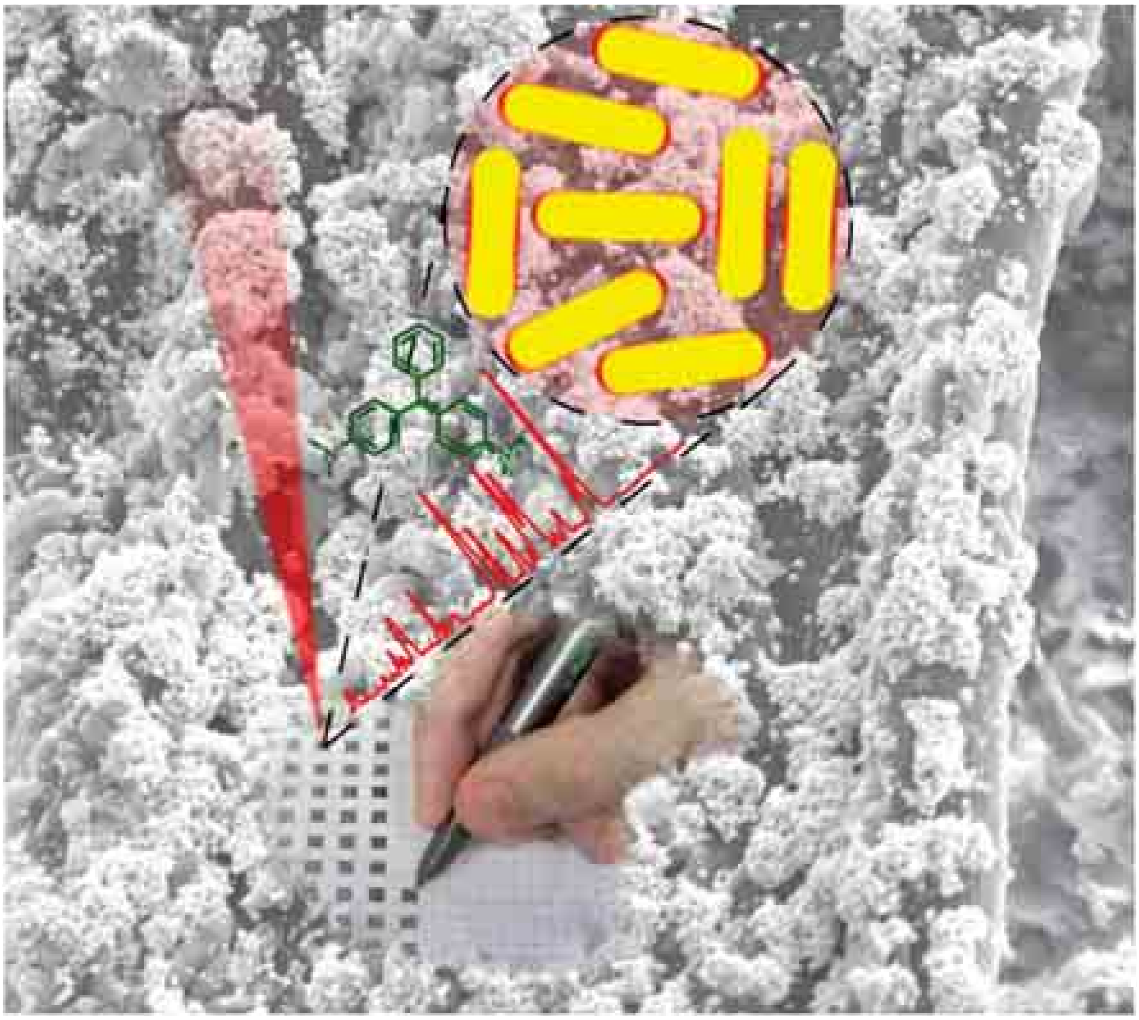

Abstract

The transformation of a technology from the laboratory into the real world should meet the demand of economic viability and operational simplicity. Inspired by recent advances in conductive inks for fabrication of electronic devices on paper, we present here a "pen-on-paper" approach to fabricate surface enhanced Raman scattering (SERS) substrates. Through this approach, no professional training is required to create SERS arrays on paper using an ordinary fountain pen filled with plasmonic nanoparticle inks that are made of metal nanoparticles of arbitrary shape and size. We demonstrate the use of plasmonic inks made of gold nanospheres, silver nanospheres and gold nanorods, to write SERS arrays that can be used with various excitation wavelengths. The strong SERS activity of these features allowed us to reach detection limits down to 10 attomoles of dye molecules in a sample volume of 10 µL, depending on the excitation wavelength, dye molecule and type of nanoparticles. Furthermore, such simple substrates were applied to pesticide detection down to 20 ppb. This universal approach offers ultrasimple, portable and cost effective fabrication of highly efficient SERS substrates at the point of care. This approach is expected to bring SERS closer to the real world in such a way that ink cartridges could be available to be fixed to a pen for creation of plasmonic sensors at will.

3.1 Introduction

What if we could create our own SERS substrates at the point care for preliminary assessment of a suspected desease or to detect specific chemical species? This challenge is to be addressed to transform the SERS technology and bring it closer to the real world.[148,149] The recent developments on smart phones coupled with spectrometers are encouraging towards portable detection based on Raman signals.[150–152] Over the past decade or so, surface enhanced Raman scattering (SERS) has emerged as one of the most attractive and powerful spectroscopic techniques for label-free ultrasensitive (down to single molecule level) detection of chemical and biological species, because of its ability to provide a spectroscopic fingerprint of each molecule.[8,42,153,154] SERS has largely profited from recent advances in the wet chemical and lithography-based preparation of plasmonic nanostructures with tunable optical properties.[50,155–157] SERS is expected to play a vital role in various fields, such as medical diagnostics, environmental and security applications in the near future. However, the transformation of this technology into real world applications has been largely hindered by problems mainly associated with reproducibility and complexity in the preparation of SERS substrates. In general, SERS substrates have been prepared by either top-down or bottom-up approaches, including electron beam lithography, colloidal lithography, chemical vapor deposition, chemical attachment of NPs to glass substrates and self-assembly.[43,45,50,99] Substrates prepared by means of the above methods exhibit excellent performance, but large scale preparation invariably leads to laborious and relatively expensive processes, which often require sophisticated instrumental facilities.

To overcome such problems associated with conventional SERS substrates, much attention has been recently paid towards paper based SERS substrates. Paper is inexpensive, flexible, biodegradable, disposable and light weight, samples can be wicked by capillary forces and it is widely used in our daily life.[148,158–167] A great deal of research has been carried out to impregnate plasmonic nanoparticles (NPs) into paper through various processes such as dip coating, inkjet printing, screen printing and physical vapor deposition.[148,158–166] For instance, Srikanth and co-workers reported SERS paper substrates impregnated with gold nanorods by dip coating.[158,162,168] However, the process required dipping the paper into a concentrated NPs solution for two days.[158,166] Yu *et al.*[160,163] reported inkjet printing of SERS arrays on hydrophobized cellulose paper. Batch fabrication of SERS substrates by screen printing has been reported by Lu *et al.*[165] However, all these processes require some kind of instrumentation. In order to fabricate viable and economical SERS substrates, the whole process should be rapid, simple and close to the real world. Can we make our own SERS substrates without any kind of instrumentation? Recently, Russo *et al.*[169] reported a pen that can be used to write flexible electronic devices on paper. Various other types of conductive NP ink pens are available in the market. Can we use a similar approach to fabricate SERS substrates immediately before sample analysis? This idea motivated us to investigate a pen-on-paper (POP) approach for the fabrication of SERS substrates.

Here we demonstrate a simple method for the fabrication of SERS substrates on paper via a POP approach that has been previously applied for paper electronics. This is a simple way of making efficient SERS substrates by directly writing on paper using a pen filled with plasmonic NP inks. We studied the SERS properties of plasmonic paper substrates prepared by using three different types of NPs (Au nanospheres, Au nanorods and Ag nanospheres), at three different excitation wavelengths. Our substrates exhibit high SERS activity at all three excitation wavelengths, but the SERS efficiency varies depending on the shape and the type of metal nanoparticles, as expected. In principle, plasmonic NPs of any shape or size that are stable at relatively high concentrations could be used as inks and one can choose the type of ink depending on the required excitation wavelength. In addition, these substrates exhibit rather high uniformity across different substrates made from the same ink, as well as long term stability, and they outperform commercially available SERS substrates. Finally, we demonstrate the application of such substrates for the detection of a pesticide down to 20 ppb.

3.2 Results and Discussion

In the present POP approach, an ordinary fountain pen with a cost of ~0.5$ was chosen for writing SERS substrates on paper, as shown in Figure 3.1. Fountain pens contain a reservoir of aqueous ink and the pen can draw the ink from the reservoir and dispense it on paper through the nib (Figure 3.1b,c), via a combination of capillary action and gravity. Depending on the fountain pen model, ink can be filled into the reservoir through the nib by suction or by filling the ink directly into a removable reservoir, like pre-filled ink cartridges. In the present case, the pen had a 2 mL reservoir that was partially filled with ink by suction through the nib. Figure 3.1a-c shows a photograph (a) and optical microscopy images (b,c) of a fountain pen with a nib diameter of ~125 µm that is filled with a NP ink for writing SERS substrates on paper. Since paper is made of organic compounds, it is important that they exhibit weak Raman cross sections.

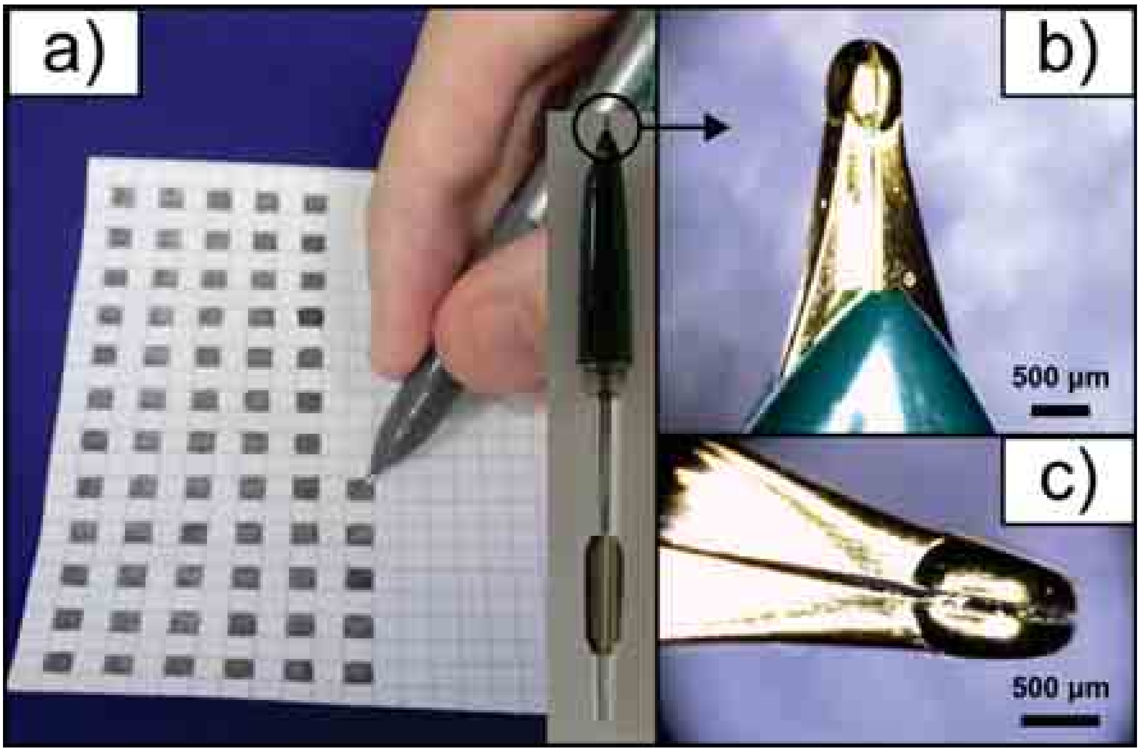

Figure 3.1. (a) Photograph of a fountain pen loaded with a plasmonic NP ink and writing SERS substrates on paper (the inset shows the inner part of the pen). (b-c) Optical microscopy images of the nib at two different magnifications.

Therefore, we measured Raman scattering spectra of paper (80 g/m^2 white color A4 photocopy paper) at three different excitation wavelengths and found that no Raman bands were detected within the spectral region where most molecules of interest are Raman active (Figure 3.2a). Interestingly, unlike filter paper, A4 photocopy paper exhibits a certain degree of hydrophobicity, which helps concentrating the sample on the SERS active area alone, rather than spreading it all over the paper by capillarity (Figure 3.2b). This is interesting because it allows us to skip a hydrophobation step by chemical functionalization, which is typically necessary to concentrate analyte molecules at a small SERS sensing area and obtain a higher efficiency.[163]

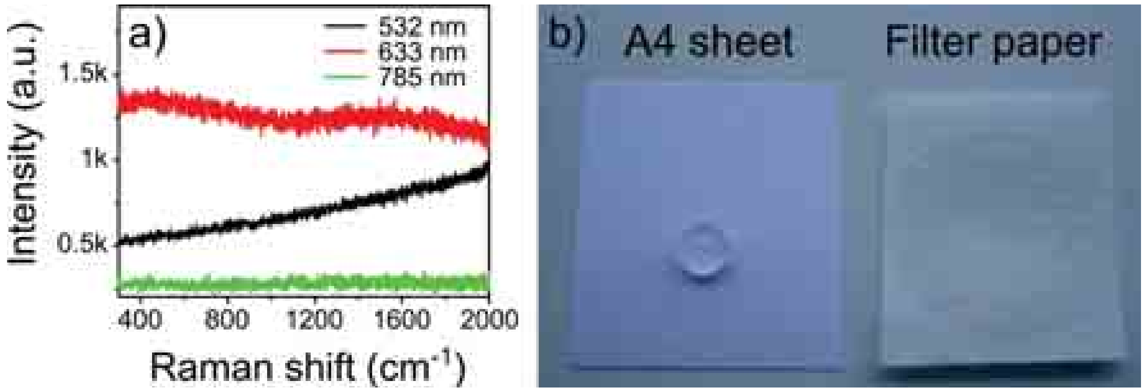

Figure 3.2. (a) Raman spectra of paper to be used for writing SERS substrates**,** obtained at three excitation wavelengths (532, 633, 785 nm). (b) Photograph of a drop of water deposited on A4 photocopy paper and on filter paper.

An essential part of this POP approach is the plasmonic NP ink, which must readily flow through the nib during writing, be stable at higher NP concentrations and be highly SERS active upon writing on paper. The SERS activity of plasmonic NPs depends on their size, shape and the type of metal, which governs their surface plasmon resonance properties. Among various metal NPs, spherical gold NPs are one of the simplest systems in terms of preparation and size tunability. Thus, we first synthesized spherical gold NPs within a wide size range (~15-120 nm) and studied their size-dependent SERS properties using crystal violet as Raman probe, to select the most appropriate particle size for the NPs ink in the POP approach (Figure 3.3). As particle size increases, the UV-Vis spectra were found to become broader and the localized surface plasmon resonance (LSPR) bands exhibit a gradual red shift (Figure 3.3a), leading to effective coupling with the 633 nm excitation laser. As a consequence, the SERS efficiency increases with the size of the NPs, up to ~95-100 nm and then it remains constant or decreases with further increase of particle size (Figure 3.3b). Additionally, particles with sizes above 100 nm exhibit poor colloidal stability in water and tend to settle down on the bottom of the container. On the basis of these results, we selected particles with an average diameter of ~95 nm as nanoparticle ink to test the SERS arrays prepared by the POP approach. TEM images of all NPs with different sizes are given in Figure 3.3.

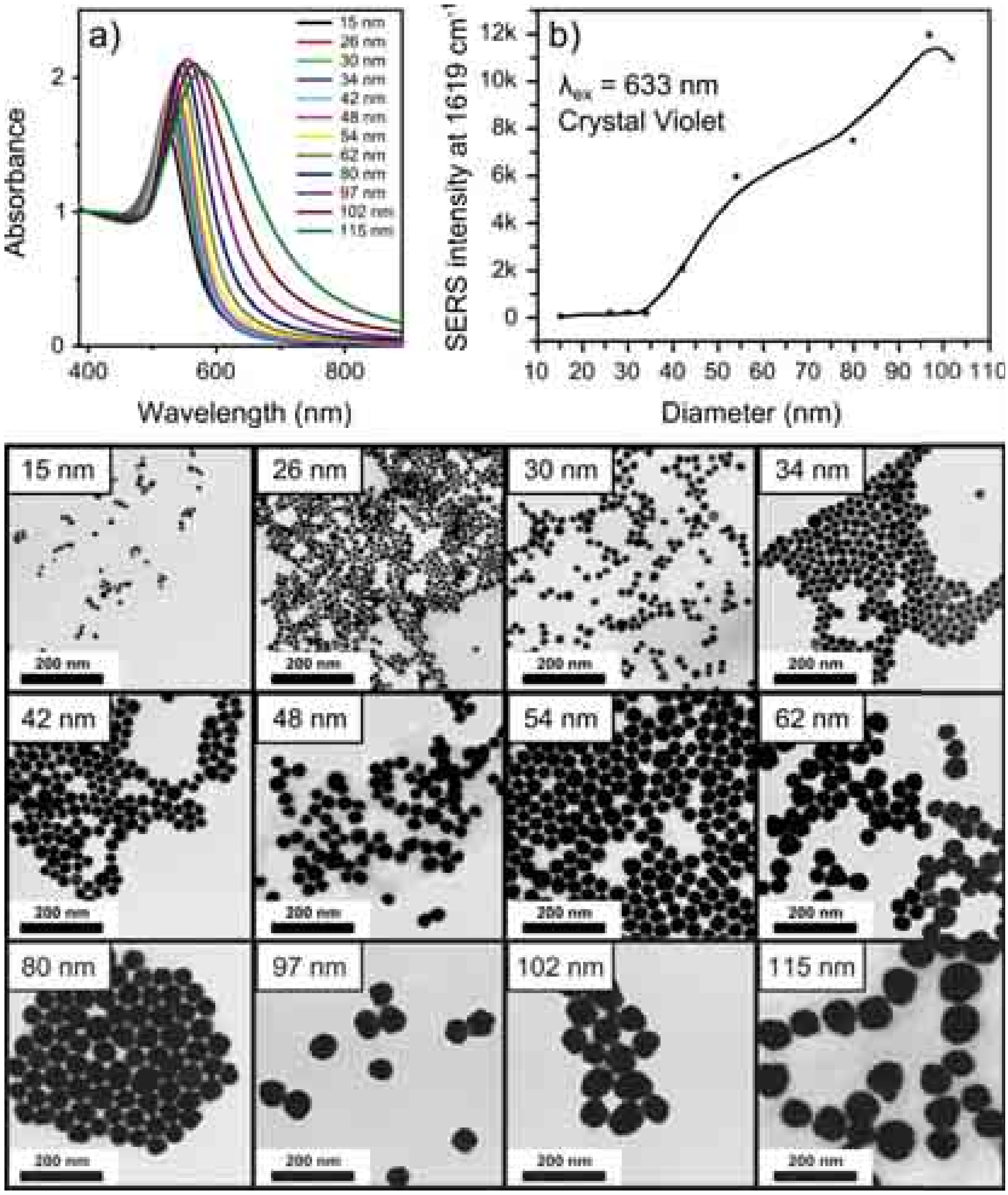

Figure 3.3. (a) Normalized (at 400 nm) extinction spectra of Au NPs of different sizes and their corresponding TEM images. (b) Particle size dependent SERS intensity of the Raman band of CV at 1619 cm^{-1}.

Figure 3.4 shows, together with the Au NPs we have chosen (3.4a), SEM images of the paper comprising a network of micron scale (10-20 μm) cellulose fibers without (3.4b) and with (3.4c) NPs. In Figure 3.4d the same sample is shown at higher magnification. Apart from spherical Au NPs, it is known from previous studies that both anisotropic gold nanostructures and silver NPs exhibit higher SERS activity than gold spheres. Thus, we also prepared Au NR and Ag NP inks and tested the SERS activity of substrates prepared from them. Au NRs with an aspect ratio of 3.6 (50 nm long, 14 nm thick) were prepared, which exhibit a longitudinal LSPR resonance at 665 nm (see Figure 3.4e for TEM and Figure 3.4f for SEM images of paper covered with them), which is close to the excitation wavelength of 633 nm. Unlike Au NPs, the size tunability of Ag NPs by the citrate reduction method is limited as polydispersity is often high. We synthesized quasi-spherical Ag NPs of sizes ranging from ~50-80 nm, as shown in Figure 3.4g. As in the previous cases, SEM of Ag NPs-covered paper fibers is shown in Figure 3.4h. It is evident that Au NPs and Au NRs are uniform in size, whereas Ag NPs exhibit rather high polydispersity, including a significant amount of high aspect ratio Ag NRs. Finally, we show in Figure 3.4i the UV-Vis spectra of both kinds of NPs.

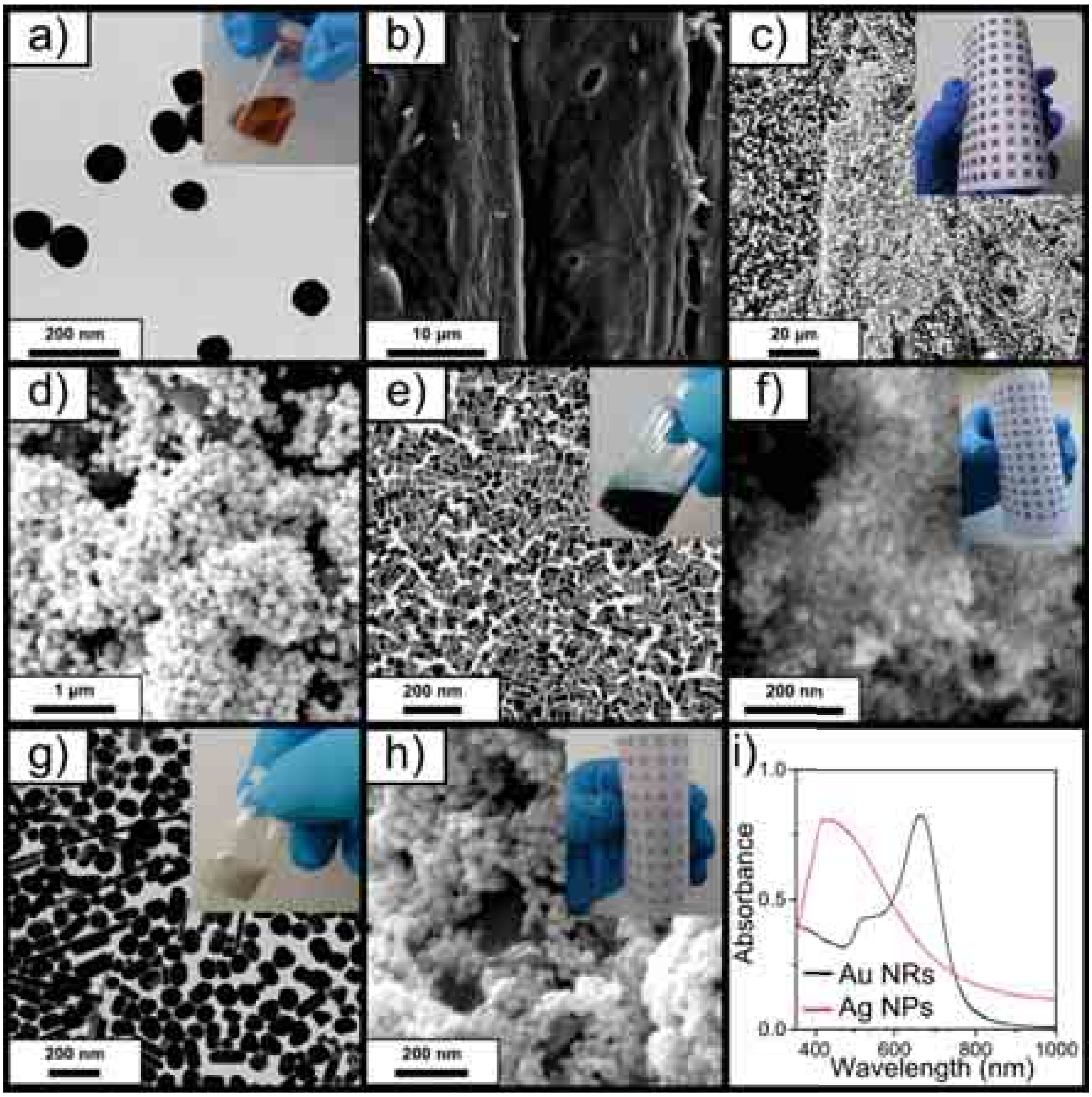

Figure 3.4. (a) TEM image of Au NPs and photograph of a representative ink. (b,c,d) SEM images of the paper before (b) and after (c and d at different magnifications) writing the SERS arrays. The inset in c shows an optical photograph of SERS-active arrays created by the POP approach. (e,g) TEM images of Au NRs and Ag NPs, respectively, and photographs of representative inks. (f,h) SEM images of SERS substrates prepared by using Au NRs (f) and Ag NPs (h) inks and photographs of the corresponding SERS arrays. (i) UV-Vis spectra of Au NRs and Ag NPs in water.

In general, as prepared NPs of any size or shape are not sufficiently concentrated to be used as inks and we thus increased the concentration by centrifugation. Moreover, excess surfactant present in the colloid should be removed to allow the analyte molecules to reach the NPs surface and achieve higher SERS activity, while preserving the particles stability after purification. We used centrifugation to purify and concentrate the NPs to 3 mg/mL. Details of the preparation of NP inks are provided in the experimental section. The three different inks were filled into three fountain pens to write SERS arrays of the corresponding NPs (note that any standard fountain pen can be used). The inks freely flow through the nib and are deposited on paper by writing so that the morphology of the SERS substrate can be easily controlled. The minimum size of the SERS spot that can be created is that of the nib (125 µm in the present case). In this approach, a very small volume of ink can be used to create large scale SERS arrays. For example, 0.2 mL of ink was used to create 15×15 spot SERS arrays with a spot area of 0.9 cm^2. Images in Fig. 3.4 show that the NPs are densely packed and adsorbed onto the surface of the cellulose fibers, so they are expected to produce intense SERS signals.

Another important factor that should be considered in the design of SERS substrates is their stability and robustness. In most earlier studies, the design was based on the immobilization of plasmonic NPs on glass substrates, either by chemical or electrostatic interactions. However, such substrates were found to be marginally stable and the particles may detach from the surface during use. We examined the adhesion between metal NPs and the paper substrate, in comparison with conventional SERS glass substrates, through the so-called scotch tape test.[170] For this test, a piece of scotch tape was pressed on the corresponding substrate and slowly pulled off (Figure 3.5). When this process was applied to Au nanostars (Figure 3.5a) attached to a 3-aminopropyl-trimethoxysilane (APTMS) modified glass substrate,[171] this conventional SERS substrate was found to lift off. However, NPs immobilized on paper (Figure 3.5b) did not come off with the scotch tape, indicating strong adhesion to the paper substrate. In addition, these substrates are stable in water, as indicated by the invariance of the patterns after dipping in water and subsequent drying (Figure 3.5c).

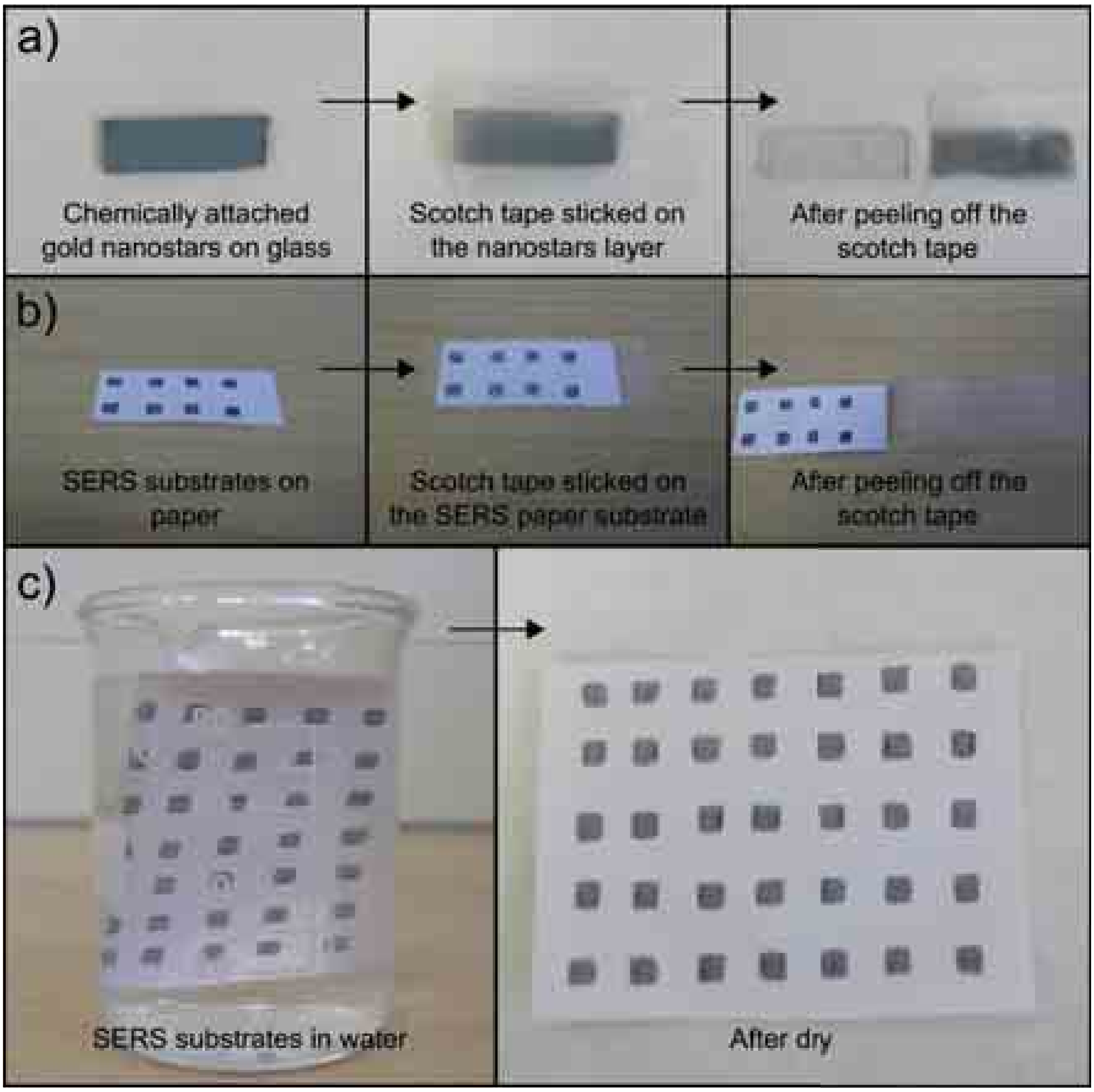

Figure 3.5. (a) A piece of scotch tape was pressed on the surface of Au nanostars attached to 3-aminopropyl)-trimethoxysilane (APTMS) modified glass substrate and then peeled off. The NPs were completely detached from the glass substrate. (b) The same test on SERS substrates prepared by POP approach; the NPs did not detach from the surface, illustrating their strong adhesion. (c) A SERS substrate prepared by POP approach was dipped into water for 15 min and then extracted and dried. No particles seem to be detached from the surface and the patterns are stable.

The SERS performance of three different substrates was characterized by drying on them a 10 μL droplet of Malachite Green (MG) as Raman active probe. MG is an organic dye, which has an effective fungicide effect that is widely used in fish farms, in the aquaculture industry and in freshwater aquaria. However, the use of malachite green is rather controversial due to its genotoxic and carcinogenic nature and it is banned in several countries. It is thus important to detect trace amounts of MG in water.[144] Figure 3.6a shows the SERS spectra of malachite green (1 mM) on three substrates under 633 nm laser excitation. It is clear that all three substrates exhibit SERS activity and the spectra clearly show the characteristic Raman peaks of MG: ring C–C stretching (1618 cm^{-1}), N-phenyl stretching (1397 cm^{-1}), ring C–H in-plane bending (1172 cm^{-1}), C–H out-of-plane bending (917 cm^{-1}). From the acquired data, the SERS efficiency of three substrates is in the order: Ag NPs > Au NRs >Au NPs, under the present experimental conditions. As expected, Au NRs exhibit higher field enhancement over spherical Au NPs, leading to higher efficiency. However, in the case of Ag NPs substrate, even though they are smaller than the Au NPs, their efficiency is highest. In general, it has been often reported in the literature that Ag NPs exhibit higher SERS efficiency over Au NPs due to their higher extinction cross section.[121,172] This trend was also observed with other Raman active probes, suggesting that these substrates exhibit high SERS activity irrespective of the type of Raman probe.

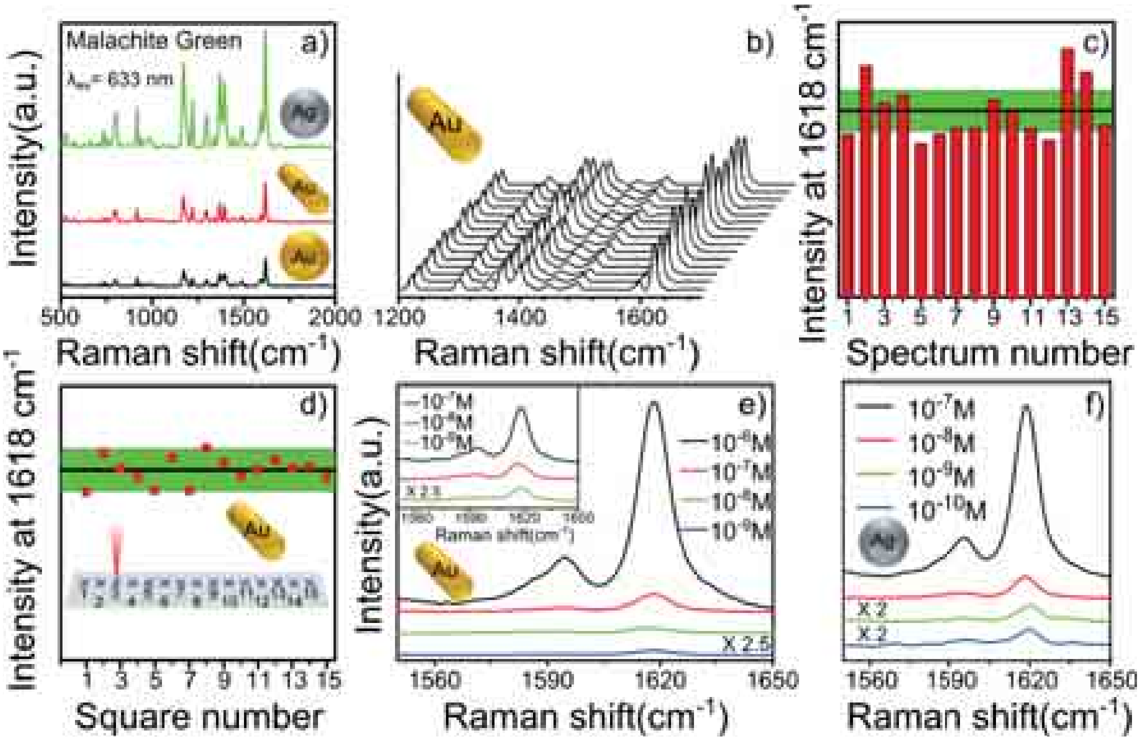

Figure 3.6. (a) SERS spectra of malachite green (1 μM) acquired from three different types of substrates prepared by POP approach (Au NPs, Au NRs, Ag NPs). (b,c) SERS spectra of malachite green acquired from 15 different spots on a single SERS paper substrate prepared with Au NRs ink (b) and the corresponding histogram for the peak intensity at 1618 cm^{-1} (c). (d) Reproducibility of SERS arrays prepared with Au NRs ink. SERS spectra were acquired at 15 different spots from an array (Inset shows the schematic representation of SERS measurements on a 15 point array). (e) SERS spectra (peak at 1618 cm^{-1}) of different concentrations (10^{-6} to 10^{-9} M) of malachite green on Au NRs substrate (the spectrum obtained at 10^{-9} M concentration was amplified 2.5 fold for clarity). (f) SERS spectra (peak at 1618 cm^{-1}) of different concentrations (10^{-6} to 10^{-10} M) of malachite green on Ag NPs substrate (the spectra obtained at 10^{-9} and 10^{-10} M concentrations were amplified 2 fold for clarity). All the SERS spectra were acquired at 633 nm excitation.

Uniformity is another major concern for any SERS substrate. In order to study the uniformity of the SERS substrates prepared by the POP approach, we registered SERS signals from 15 random places on one of the Au NRs substrates and the data are depicted in Figure 3.6b,c. The results indicate that the variation of intensity is within 10-20% (higher variations were rarely observed due to variation of NP density and non uniform drying of analyte at some places). In addition, we also tested the intensity variations from spot to spot within an array (Figure 3.6d), showing a high reproducibility. These results are remarkable considering the simplicity of preparation, cheapness and robustness of the substrates. Furthermore, the sensitivity of Au NRs and Ag NPs SERS substrates was tested as shown in Figures 3.6e and 3.6f, respectively. MG SERS signals are clearly detectable down to 1 nM on Au NRs and 0.1 nM on Ag NPs substrates, which represents 10 and 1 femtomoles of MG molecules, respectively, in 10 μL of sample volume. The sensitivity of these substrates is similar or even higher than that of substrates prepared by inkjet printing, depending on the type of NP ink.[163]

Although we have so far shown that SERS substrates can be readily prepared at the point of care by means of the POP approach, an ideal substrate should be stable for long periods of time. Thus, the stability of the substrate was studied by comparing the SERS signals from a freshly prepared Au NRs substrate and the substrate after storage under atmospheric conditions for one month (Figure 3.7a). The results on substrates made of NRs show that both substrates exhibit similar intensity on average, illustrating their long term stability. However it is mention that long term stability might not be possible with all kind of NPs, particularly with Ag as they tend to oxidize easily when they transferred from solution to substrates. In such cases, the preparation of substrates at the point of care is crucial and this approach offers unique way of preparation. Importantly, all three substrates exhibited higher SERS efficiency over commercial SERS substrates under the same experimental parameters (Figure 3.7b).

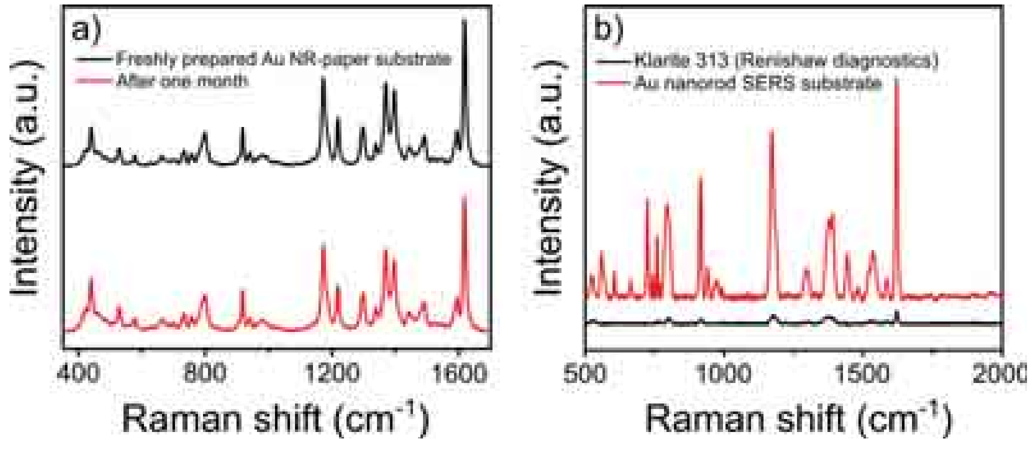

Figure 3.7. (a) SERS spectra of malachite green (1 μM) acquired from freshly prepared Au NRs SERS substrate and from a substrate prepared one month before. (b) SERS spectra of crystal violet (1 μM) acquired from Au NRs substrate prepared by POP approach and from the commercial Klarite substrate (Renishaw Diagnostics). Au NRs substrate shows much higher intensity than the commercial substrate (optimized from 633, 785 nm excitation). All the spectra have been recorded with 633 nm excitation wavelength.

Most of the results presented above were obtained with an excitation wavelength of 633 nm. For completeness, the SERS activity of the substrates was also studied with 532 and 785 nm laser excitations and the results are depicted in Figure 3.8. We found that all three substrates exhibit SERS activity under 785 nm excitation (Figure 3.8a), which is important in bio-related applications, but Au NPs and Au NRs substrates show poor SERS signals for MG under 532 nm excitation (Figure 3.8b), due to plasmon damping by coupling to interband transitions.[172,173]

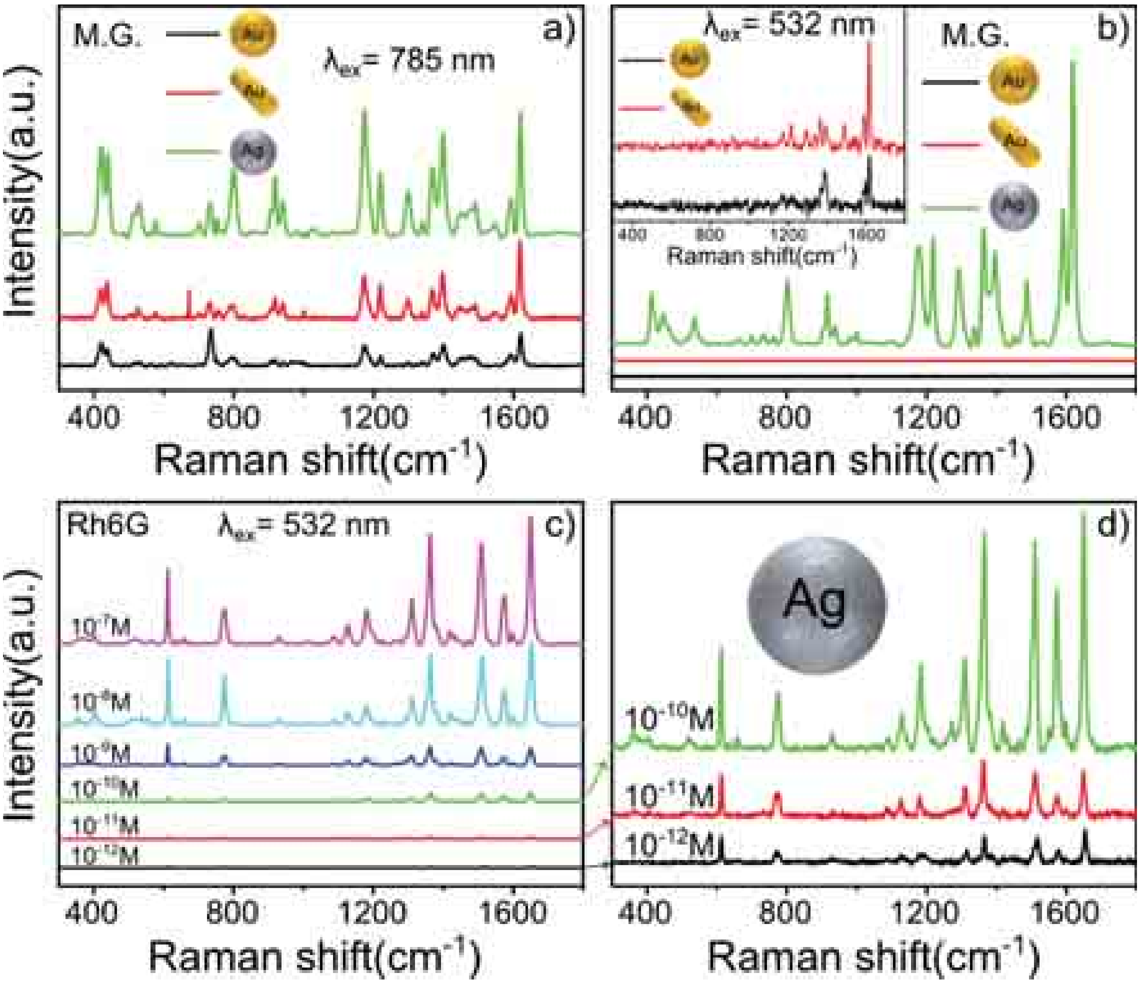

Figure 3.8. (a, b) SERS spectra of malachite green (1 µM) collected from three different SERS substrates (Au NPs, Au NRs, Ag NPs) with excitation wavelengths of 785 nm (a) and 532 nm (b). (c) SERS spectra of R6G at different concentrations (10^{-7} to 10^{-12} M) on Ag NPs substrate with 532nm excitation. Magnified spectra at low concentrations are shown in (d).

However, Ag NPs substrates do exhibit intense SERS activity with 532 nm excitation. We studied the SERS efficiency of Ag NPs substrates with 532 nm excitation for R6G detection, which has been reported for other Ag NPs substrates.[118] Interestingly, our Ag NPs substrates provided extremely high sensitivity down to 10^{-12} M, corresponding to 10 attomoles of R6G molecules in a 10 µL sample volume. As shown in Fig.3.8c, the SERS signal intensity gradually decreased with the decrease of R6G concentration, this indicating the possibility of quantitative determination of analyte. Figure 3.8d shows the three lowest concentrations for clarity.

The calculation of enhancement factor (EF) is not straightforward. Various methods have been reported in the literature depending on several factors. For instance, by measuring the SERS spectrum of a bulk powder of the analyte, one has to calculate the EF based on several assumptions such as penetration depth of the laser and molecular packing, which leads to a significant error. In the case of resonant dyes, fluorescence usually screens the Raman signals, which gives EF higher than the real value. So, based on our experience, it is extremely difficult to measure the EF at the resonance frequency of fluorescent Raman probes. We thus calculated the enhancement factor of the substrate prepared by POP approach at a non-resonant frequency (532, 785 nm) for MG. The average EF was is determined by comparing the signals acquired from MG at a concentration of 1 mM on paper without NPs, with the signals obtained from MG at a concentration of 1 µM on Ag NPs on paper. The EF was calculated using the formula, $E.F. = (I_{SERS}/I_{Ref})(C_{Ref}/C_{SERS})$, where, where I_{SERS} and I_{ref} represent the intensities of the 1618 cm^{-1} band for MG adsorbed on the Ag impregnated paper substrate and paper substrate, respectively, whereas C_{SERS} and C_{ref} represent the corresponding concentrations of MG on these substrates. The average enhancement factors on Ag NPs substrates were roughly estimated to be ~2×10^5 and 1.5×10^5 at 532 and 785 nm, respectively. These average EFs are similar to those previously reported for some of the conventional SERS substrates[174] and even with inkjet-printed SERS substrates.[163]

We finally demonstrate the application of these substrates for the detection of thiabendazole, which is a fungicide and parasiticide. It has been widely used as food preservative and additive, but it is not approved in EU, Australia and New Zealand due to its toxicity at higher doses. Figure 3.9a shows the SERS spectra of thiabendazole (20 ppm) acquired with different excitation wavelengths, illustrating the ability to detect it with any available excitation wavelength. At all excitation wavelengths, the characteristic SERS signals of thiabendazole were registered: skeletal ring stretching modes (1580 cm^{-1}, 1546 cm^{-1}), phenyl ring breathing mode (1010 cm^{-1}), Ag–S bond stretch (782 cm^{-1}) and C–N stretch (1280 cm^{-1}). SERS analysis of thiabendazole at 785 nm excitation and decreasing concentrations showed a detection sensitivity of 20 ppb in a 10 µL sample volume (Figure 3.9b).

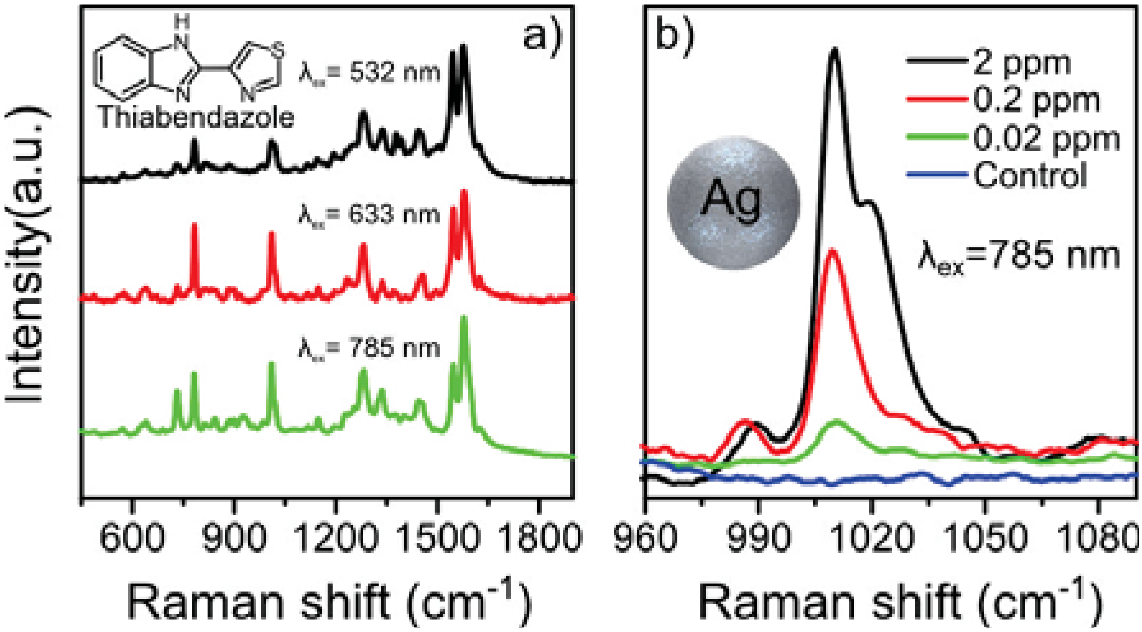

Figure 3.9. (a) SERS spectra of thiabendazole (20 ppm) on Ag NPs substrate with three different excitation wavelengths of 532, 633 and 785 nm. (b) SERS spectra (peak at 1008 cm^{-1}) of thiabendazole with different concentrations (2, 0.2, 0.02 ppm) on Ag NPs substrate with 785 nm excitation.

3.3 Conclusions

In this chapter we demonstrated the application of the pen-on-paper approach used in the field of paper electronics, for simple and economically viable design of highly efficient, reproducible, uniform and low-cost SERS substrates. In this approach, a fountain pen filled with plasmonic NPs ink was used to directly write SERS arrays on paper substrates with no need of any professional training. Au NP, Au NR and Ag NP inks were tested for the preparation of efficient SERS substrates, which exhibit highly efficient detection, even down to 10 attomoles of molecules in a sample volume of 10 μL, depending on the excitation wavelength, dye molecule and the type of NPs. Such substrates, in particular those containing Ag NPs, exhibit high SERS activity over a broad range of excitation wavelengths. As a practical application, we demonstrated the detection of toxic parasiticide molecules down to 20 ppb in a 10 μL sample volume. Thus, this universal approach is expected to bring the SERS technology closer to real world applications.

3.4 Experimental Section

Materials: Tetrachloroauric acid ($HAuCl_4 \cdot 3H_2O$), trisodium citrate dihydrate, silver nitrate ($AgNO_3$), L-ascorbic acid, Rhodamine 6G, crystal violet, and thiabendazole were purchased from Sigma-Aldrich. Cetyltrimethyl ammonium bromide (CTAB) and malachite green were purchased from Fluka. All chemicals were used as received, without further purification. Fountain pens were purchased from a general store in India with a cost of ~0.5$ per pen. Glassware was washed with aqua regia followed by water. Milli-Q water (Millipore) was used throughout the experiments.

Preparation of Au nanoparticles of different sizes and NPs ink: Citrate-stabilized Au NPs of different sizes were prepared by the kinetically controlled seeded growth method reported by Bastús *et al*.[56] Briefly, Au seeds were first prepared by injecting 1 mL $HAuCl_4$ (25 mM) solution to the boiling solution of 150 mL, 2.2 mM sodium citrate. The color of the solution changes from colorless to pink after 10 min of reaction. In order to grow the obtained seeds into bigger Au NPs, the reaction temperature of the seed solution was first cooled down to 90 ºC immediately after seed formation and then 1 mL $HAuCl_4$ solution (25 mM) was added. After 30 min of reaction time, another 1 mL of $HAuCl_4$ solution (25 mM) was injected. After the reaction, the sample was diluted by extracting 55 mL of the obtained Au NPs solution and adding 53 mL of water and 2 mL of 60 mM sodium citrate. The obtained colloid was used as seed solution to further increase the Au NPs size. Such process was continued until the Au NPs size reached to 115 nm. From the size dependent SERS measurements, 95 nm NPs were selected to prepare Au NPs ink, which was prepared by concentrating the 100 mL of obtained Au NPs into 1.5 mL by centrifugation for a final concentration of 3 mg/mL.

Preparation of Au nanorod ink*:* Gold nanorods were prepared by seed mediated growth.[175] Seed solution was prepared by adding 0.3 mL of 10 mM ice-cold $NaBH_4$ solution to a mixture of CTAB (4.7 mL, 0.1 M) and $HAuCl_4$ (25 µL, 0.05 M) aqueous solution under vigorous stirring at room temperature. Upon $NaBH_4$ addition, the solution color changes from pale yellow to brown, indicating the formation of small seed particles. Nanorods were grown by adding 0.36 mL of seed solution to a growth solution (prepared by mixing 150 mL of CTAB (0.1M), 1.5 mL of $HAuCl_4$ (0.05 M), 0.225 mL of $AgNO_3$ (0.01 M), 0.12 mL of ascorbic acid (0.1M)). The solution color changes from colorless to blue after the addition of seed solution to the grown solution. The obtained solution was centrifuged twice and redispersed in 2 mL of water to obtain Au NR ink with a concentration of 3 mg/mL. The final concentration slightly varied from batch to batch depending on the purification step, however it can be easily adjusted by either diluting or concentrating the obtained NPs solution.

Preparation of Ag nanoparticle ink*:* The Ag NPs were synthesized according to the Lee and Meisel method.[95] Briefly, 4.5 mL of 1.00 wt% trisodium citrate solution was added to the boiling solution containing 42 mg of $AgNO_3$ in 200 mL of water under vigorous stirring. The reaction was boiled for another 1 hr and then cooled to room temperature. The obtained Ag nanoparticles in 200 mL of water were centrifuged at 7000 rpm for 20 min and then redispersed in 2 mL of water to obtain Ag NP ink with a concentration of 3 mg/mL.

Characterization*:* The optical properties of nanoparticle solutions were recorded using an Agilent 8453 UV-Vis spectrophotometer. TEM images were obtained using a JEOL JEM 1400 Plus microscope operating at an acceleration voltage of 100 kV. For SEM measurements, nanoparticles impregnated papers were first coated with a layer of Ti-Au (~3 nm) to make their surface partially conductive to minimize charging effects. SEM images of Au and Ag NPs were obtained using SEM (JEOL 6490LV) and the SEM images of Au NRs were obtained using ESEM Quanta250 FEG (FEI company, Netherlands). Optical photographs of a pen nib were obtained with an optical microscope (Leica Microsystems).

Size dependent SERS study of Au NPs suspensions*:* Size dependent SERS properties of Au NPs were measured by adding 20 µL of a 10 µM crystal violet solution to 1 mL of 0.02 nM (nanoparticle concentration) Au NPs of different sizes and then the average SERS signals were recorded from the NPs suspensions using a micro-Renishaw InVia Reflex system equipped with Peltier charge-coupled device (CCD) detectors with the excitation wavelength of 633 nm.

SERS measurements on NPs substrates prepared by POP approach: SERS substrates were prepared by direct writing of SERS arrays on paper and each spot of the array is a square with an area of 0.3×0.3 cm^2. SERS measurements were performed using the same Raman system mentioned above. For SERS characterization, a 10 µL of analyte was dropped onto a NPs impregnated paper substrate having dimensions of 0.3×0.3 cm^2 and then dried in an oven at 60 ºC for 5 minutes. The signals from each sample were collected for 10s using a 100× objective with three different excitation wavelengths of 532, 633 and 785 nm. The laser beam was focus on the nanoparticles clusters by looking in the optical microscope connected to the Renishaw Raman spectrometer. Importantly, the focus of the laser beam was adjusted to maximum SERS signal at each point as the microscopic organization of the fibers is not flat.

CHAPTER 4

THE IMPORTANCE OF CITRATE AS STABILIZING AGENT FOR GOLD NANOPARTICLES IN SURFACE-ENHANCED RAMAN SCATTERING

Abstract

This chapter deals with the study of the SERS efficiency of gold nanoparticles with different morphologies, both in solution and on solid supports. The effect of surface functionalization was analyzed by replacing the original CTAB stabilizing agent with citrate ions, for all geometries. The influence of nanoparticle shape and size on the SERS response of such systems was studied by using three different excitation wavelengths, so as to understand the correlation with the localized surface plasmon resonance for each morphology. Upon optimization of key parameters in SERS spectroscopy such as surfactant concentration and irradiating power, we were able to detect typical Raman probes in solution down to the nanomolar range by using gold nanotriangles as optical enhancers. Switching from solution to substrate we observed a significant change in the relative efficiency between the different shapes, so that gold nanospheres were found to yield at least one order of magnitude higher signals than nanoparticles with other geometries.

4.1 Introduction

Since Michael Faraday first documented the synthesis of colloidal gold nanoparticles (AuNPs) back in 1856[176], the field of colloidal synthesis of nanocrystals has largely evolved, in turn leading to a huge progress of the science of metal nanoparticles. The importance of AuNPs arises from their unique optical properties, related to phenomena taking place at the interface between gold nanoparticles and dielectric medium, under light irradiation. Such an interaction generates stationary surface charge density waves localized at the interface and are known as localized surface plasmon resonances (LSPRs). Among other parameters, the polarizability of free electrons in AuNPs strongly depends on particle size and shape. Additionally, when gold nanoparticles are in close proximity at the nanoscale, electromagnetic coupling leads to new plasmon resonance modes that produce even larger field enhancements at interparticle gaps, known as *hot spots.*[177,178]

Although two different phenomena, absorption and scattering, occur to a different extent when AuNPs are irradiated with light, most technological applications of metal nanoparticles are based on the former, including surface enhanced Raman scattering (SERS) spectroscopy.[34,178] This technique is based on the enhancement of the Raman scattering spectra of molecules and biomolecules, in the presence of plasmonic nanostructures. Hence, the Raman cross section of a molecule at the nanoparticle surface is strongly enhanced and makes detection at ultra-low concentrations possible.[8] The magnitude of the enhancement is defined by the LSPR of AuNPs but also by the interaction of the analyte with the surface. Within this context, shape, size, assembly and surface chemistry of the nanoparticles are key parameters governing SERS spectroscopy.[34,42] In recent years a wide variety of approaches were reported with the aim to develop an ideal platform for SERS. The majority of the strategies relie on the creation of hot spots using AuNPs of different morphologies, either by controlled assembly in solution or by formation of 2D and 3D assemblies on substrates.[121,179–181] However, practical comparison between different systems and particles is challenging due the high variability introduced by the different surface cappings employed. For instance, thiolated molecules that bind strongly to gold atoms generally prevent close contact between the NP surface and the analyte, thus considerably reducing the SERS efficiency of the system. Moreover, in most cases the use of such molecules is required in the synthesis of specific shapes.[64,71,182,183]

We present herein a study in which we initially compare the effect of the morphology of three different CTAB-capped NPs on SERS enhancement, as a function of surfactant concentration. We propose the use of sodium citrate as a more suitable stabilizer than CTAB, since its relatively weak interaction with gold should further improve SERS activity. Additionally, citrate-stabilized AuNPs allowed us to prepare highly uniform and efficient SERS platforms.

4.2 Results and Discussion

AuNPs with different morphologies were synthesized using previously existing protocols: nanotriangles (AuNTs) with LSPR around 633 nm (laser excitation wavelength),[182] nanorods (AuNRs)[64] and nanospheres (AuNSs). UV-Vis spectra are displayed in Figure 4.1, from which the plasmon band position of the different morphologies can be determined: 720 nm for the longitudinal LSPR of AuNRs and 640 and 551 nm for AuNTs and AuNSs, respectively. TEM analysis allowed us to estimate the dimensions of the NPs and the results are shown in Table 4.1.

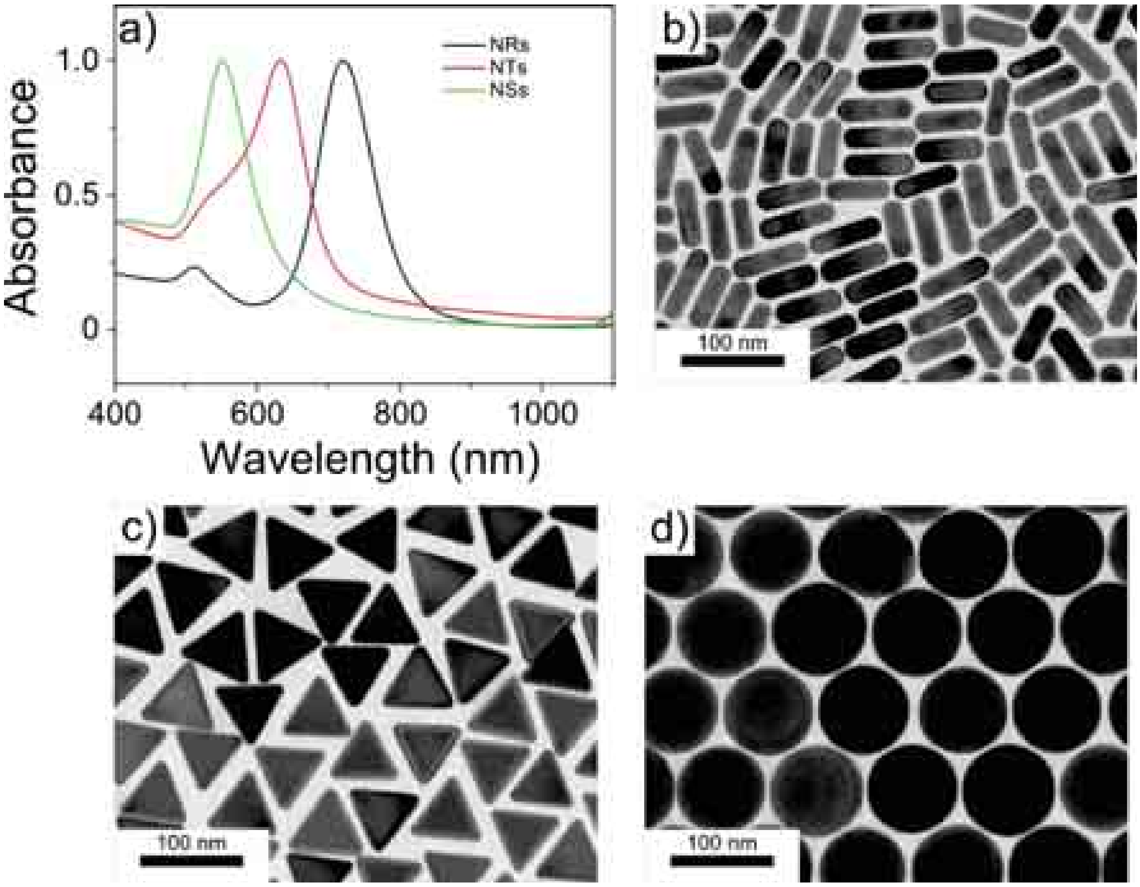

Figure 4.1. (a) Normalized UV-Vis spectra and TEM images of (b) AuNRs, (c) AuNTs and (d) AuNSs.

Table 4.1. Average dimensions of AuNPs with different shapes from TEM analysis.

AuNRs		AuNTs	AuNSs
Width (nm)	Length (nm)	Edge length (nm)	Diameter (nm)
22.45 ± 1.53	66.33 ± 5.39	65.6 ± 3.61	88.04 ± 3.13

After synthesis, the CTAC present onto the surface of AuNTs and AuNSs was replaced by CTAB (see Experimental Section). The optimization of conditions for SERS experiments started by using the three different morphologies in solution for the detection of Crystal Violet (CV), a common Raman dye, at a concentration of 1 μM. The results are shown in Figure 4.2a as a plot of the intensity of the C-C stretching peak at 1618 cm-1, as a function of CTAB concentration. Even though the highest intensity was recorded for AuNSs at a CTAB concentration of 1μM, observation of the UV-Vis spectra for all solutions after SERS measurement (Figure 4.2b,c and d), it is clear that strong aggregation occurred for this sample, at such a low surfactant concentration.

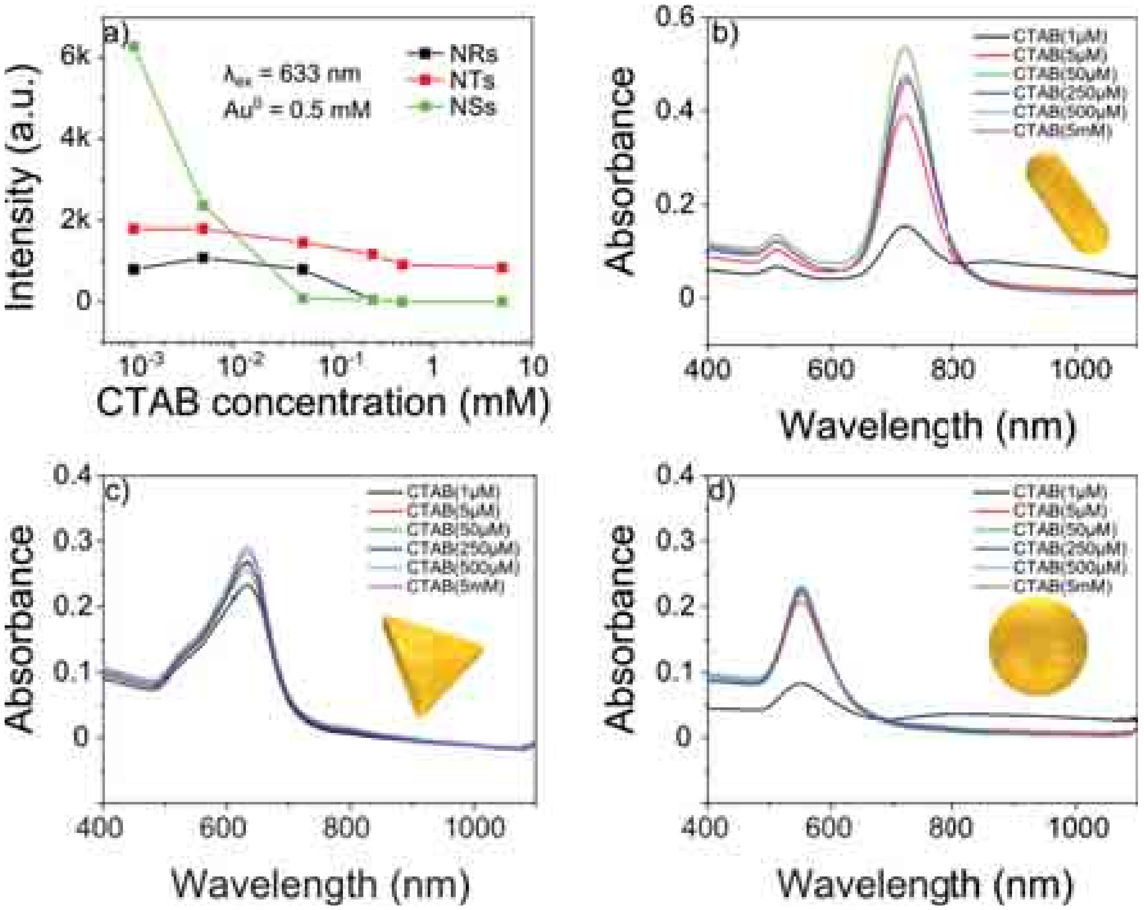

Figure 4.2. (a) Intensity of the peak at 1618 cm^{-1} in CV SERS spectra, as a function of CTAB concentration. (b-d) UV-Vis spectra of the three different samples (as indicated by drawings) after SERS measurements.

A concentration of 50 μM CTAB was selected for subsequent SERS experiments, as a reasonable balance between a low amount of CTAB in solution and reduced aggregation of the NPs. In such conditions, the SERS response was evaluated for each NP shape, with different excitation wavelengths and using again CV as analyte at the same concentration (1 μM). As shown in Figure 4.3, AuNTs exhibit the strongest signal regardless of the laser excitation wavelength (532, 633 or 785 nm). It is important to highlight that up to this point no optimization of the laser configuration, such as power and integration time, was carried out and, as a consequence, a comparison between laser intensities would not be meaningful.

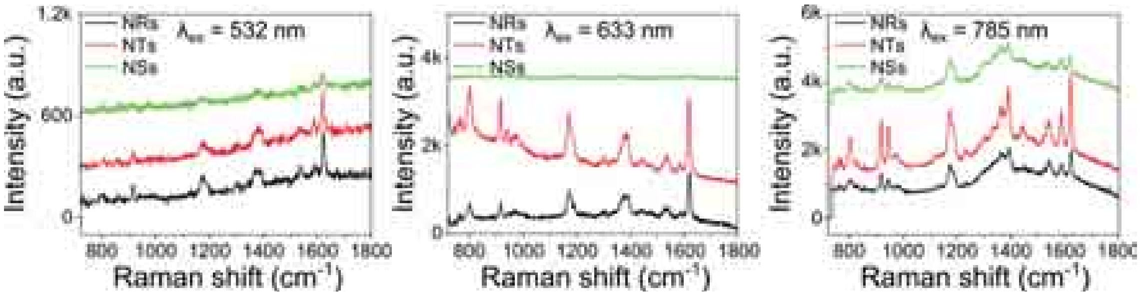

Figure 4.3. Comparison of SERS spectra concerning three different NPs shapes at laser excitation wavelengths of 532, 633 and 785 nm.

In order to further improve the SERS efficiency of AuNTs, a second modification of the NP surface coating was performed. Due to its size and high affinity toward Au, CTAB strongly affects analyte detection because it creates a thick and stable bilayer around the NPs that prevents the analyte from arriving close enough to the particle surface, so as to feel the electromagnetic field enhancement. Recently, Mehtala *et al.*[184] demonstrated that it is possible to obtain CTAB-free AuNRs and stabilize them with sodium citrate by repetitive centrifugation and redisperision cycles in sodium polystyrenesulfonate (Na-PSS). By applying this protocol (see Experimental Section for details) we were able to obtain stable citrate-stabilized AuNTs with no significant changes in the UV-Vis spectra (Figure 4.4a).

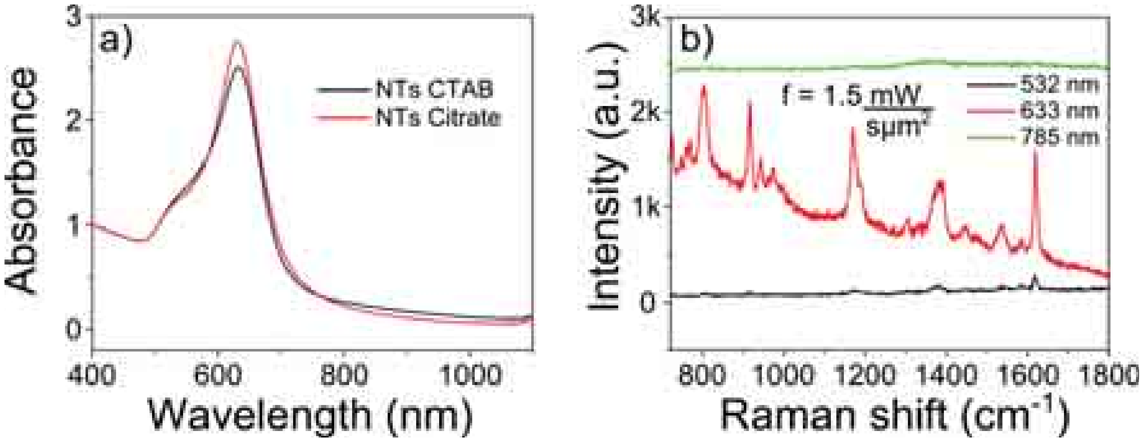

Figure 4.4. (a) Normalized UV-Vis spectra of AuNTs before and after surfactant exchange from CTAB to citrate. (b) SERS spectra of CV using AuNTs as substrates, at different excitation wavelengths. The flux *f* is indicated.

Figure 4.4b shows the SERS spectra of AuNTs using again three excitation wavelengths. The only difference is that in this case the flux of power *f*, defined as the irradiating surface power density per second, was adjusted to be the same for all lasers. At $f\ = 1.5\, mW/s\mu m^2$, the plot shows that CV (1 μM) vibrations are only visible at the excitation of 633 nm, which is in accordance with the coupling between the laser and the LSPR band of AuNTs. Once optimal conditions for SERS detection were identified, we compared the efficiency of AuNTs@CTAB and AuNTs@Citrate (Figure 4.5a). AuNTs@Citrate exhibit a SERS signal intensity that is approximately three times more intense than that from AuNTs@CTAB, which confirms the fact that it is easier for citrate to be replaced by the analyte onto the NP surface. The enhancement of the signal due to surfactant exchange allowed us to detect CV down to 1 nM (Figure 4.5b). The integration time during the measurements of different concentrations of CV was selected to improve clarity in the resulting spectra.

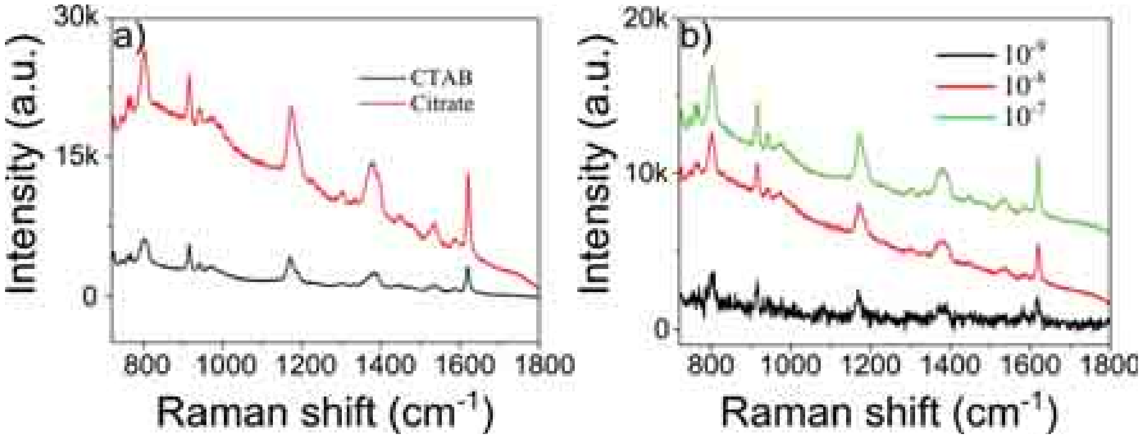

Figure 4.5. (a) SERS spectra of AuNTs@CTAB and AuNTs@Citrate. (b) Limit of detection down to 10^{-9} M. For clarity, the background spectrum corresponding to AuNTs@Citrate with no CV was subtracted from the 10^{-9} M curve.

Apart from "average" SERS measurements directly in solution, citrate-stabilized NPs were also tested as SERS substrates on solid supports. Uniform adsorption of AuNPs was achieved by using glass slides functionalized with (3-Aminopropyl)triethoxysilane (APTES), which were immersed in a highly concentrated colloidal solution ([Au^0] = 10 mM) and incubated for 1 h. As opposed to the experiment in solution, in this case AuNTs showed the weakest SERS intensity (Figure 4.6a) so they were not considered for this study. In order to study not only the influence of NP shape but also of particle size, smaller Au nanospheres were additionally considered. Statistical analysis revealed an average diameter of 45.42 ± 1.6 nm for this sample. Figures 4.6b,c,d show UV-Vis spectra and representative TEM images for this new sample, as well as photographs of the final substrates.

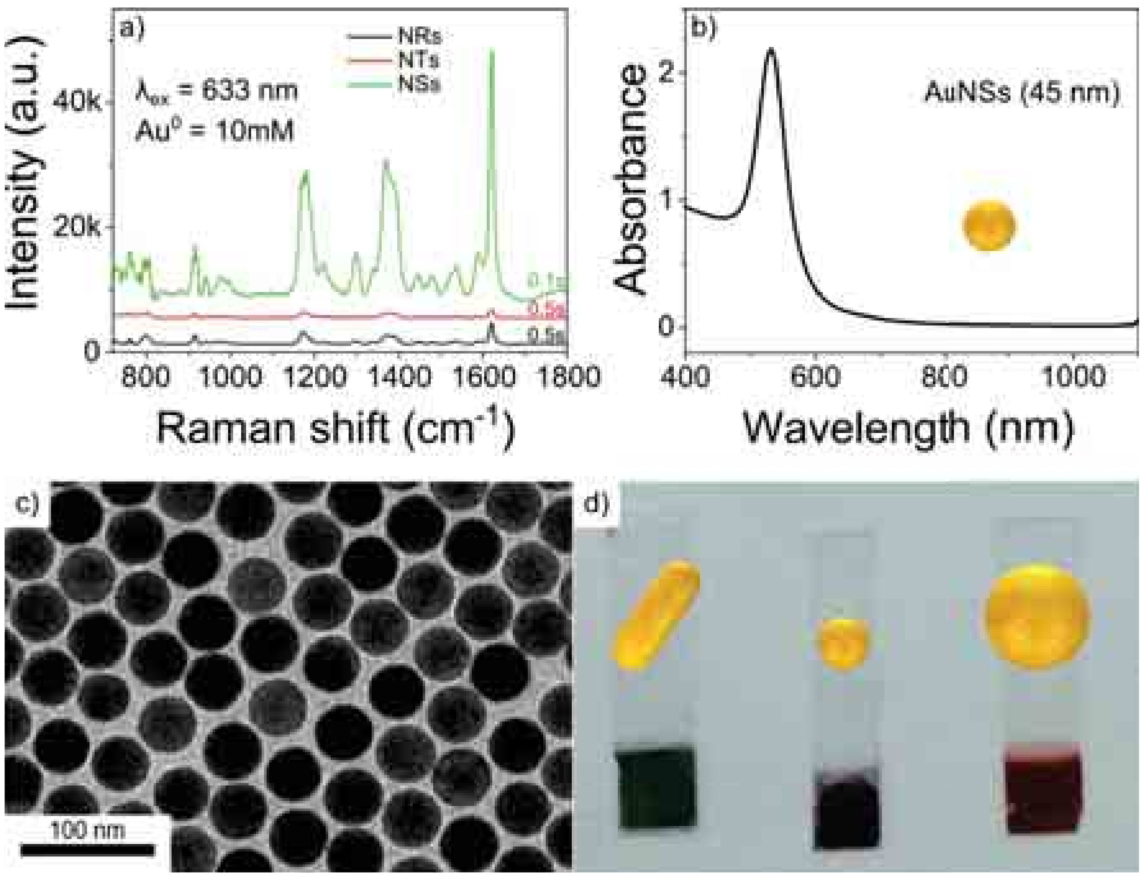

Figure 4.6. (a) SERS spectra of CV on the three different AuNP shapes deposited onto glass slides. (b,c) UV-Vis spectrum and TEM image of AuNSs of approximately 45 nm diameter. (d) Digital photographs of the different substrates.

It is remarkable that the intensity of the C-C stretching peak of CV at 1618 cm^{-1} was found to be one order of magnitude more intense for 90 nm AuNSs than for AuNRs. It should additionally be noted that, in Figure 4.6a, the spectrum for AuNSs was recorded with a lower integration time because the detector was saturated when measured under analogous conditions to those for AuNRs and AuNTs. Figure 4.7a shows the UV-Vis spectra of the film samples. Two well-defined LSPR bands were recorded for AuNSs, which might be an indication of the presence of nanoparticle clusters. In the case of AuNRs the strong coupling between individual particles leads to significant broadening of the LSPR band. SEM images of all samples are also shown in Figure 4.7.

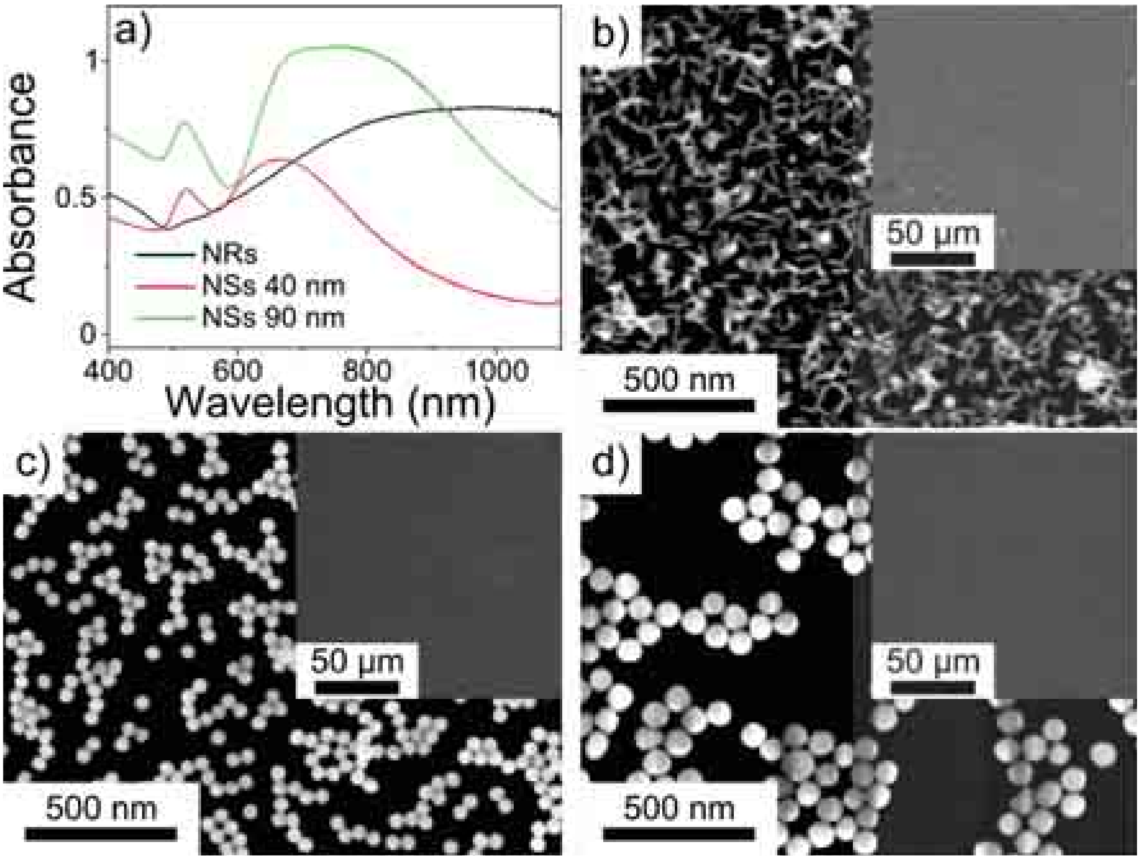

Figure 4.7. (a) UV-Vis spectra of AuNPs onto solid supports. (b-d) SEM images of the substrates covered with AuNRs, AuNSs (45 nm) and AuNSs (90 nm). The insets show SEM images at low magnification to highlight the uniform coverage of the glass slides.

In order to test the versatility of the substrate, additional SERS measurements were performed by using CV (10^{-7} M) and 4-Mercaptobenzoic acid (MBA, 10^{-5} M). As shown in Figure 4.8, the combination of AuNSs of 90 nm and 633 excitation laser yields the best response in terms of intensity, for both analytes. These results were obtained by averaging the intensities recorded over 60 different spots onto the films, covering an area of 20x20 μm^2. From the statistical analysis of the standard deviation, it is possible to estimate the fluctuation of the signal from point to point from the averaged value. For instance, in the case of 90 nm AuNSs at 633 nm excitation the fluctuation was found to be ca. 7.6% for CV and ca. 3.7% for MBA. This is an additional evidence of the high uniformity of the prepared SERS substrates.

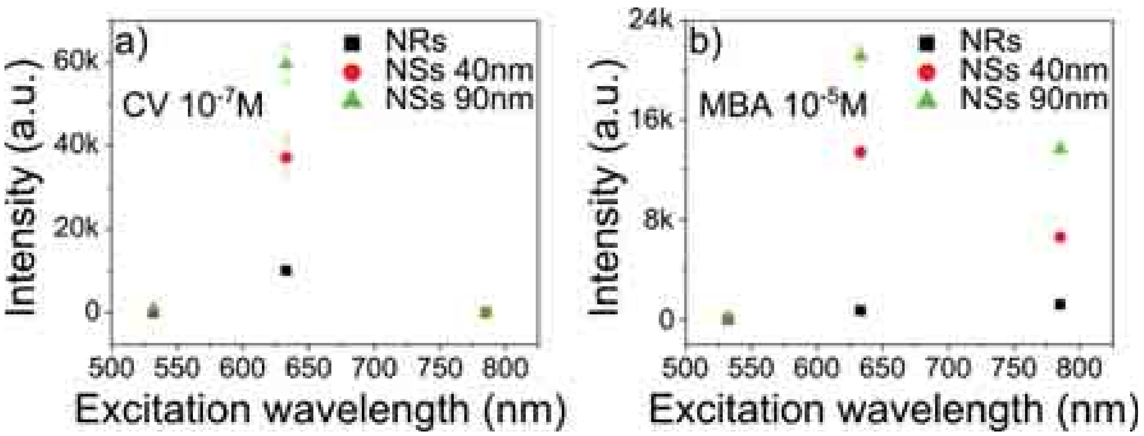

Figure 4.8. Plots displaying the SERS intensity of characteristic peaks of the analytes (1618 cm^{-1} for CV and 1587cm^{-1} for MBA), recorded by excitation of each sample at three different wavelengths (532, 633 and 785 nm).

4.3 Conclusions

In this chapter we have shown the possibility to exploit the stabilization of AuNPs with sodium citrate to enhance the SERS performance, as compared with the same AuNPs covered with CTAB. Studies of the influence of surfactant concentration, NPs shape and excitation laser wavelength, we have been able to detect CV in solution down to 1 nM by using AuNTs@Citrate. In addition, solid supports of densely packed citrate-stabilized NPs were obtained by simply functionalizing a glass support with APTES. Such substrates showed high uniformity and promising SERS performance, in particular with AuNSs of 90 nm diameter, which yielded the best response in terms of SERS intensity.

4.4 Experimental section

Chemicals. All chemicals were obtained from commercial suppliers and used without further purification: Hexadecyltrimethylammonium bromide (CTAB, ≥99%), hexadecyltrimethylammonium chloride (CTAC, 25% wt in water), 5-bromosalicylic acid (technical grade, 90%), hydrogen tetrachloroaurate trihydrate ($HAuCl_4 \cdot H_2O$, ≥99.9%), silver nitrate ($AgNO_3$, ≥99.0%), L-ascorbic acid (≥99%), sodium borohydride ($NaBH_4$, 99%), sodium bromide (BioUltra, ≥99.5%), crystal violet (CV, ≥90%), 4-

Mercaptobenzoic acid (4-MBA, 90%), poly(sodium 4-styrenesulfonate), Mw ~70,000, powder, sodium citrate tribasic dehydrate (≥98.0%). Nanopure water (resistivity 18.2 MΩ·cm at 25 °C) was used in all experiments.

Characterization. Optical extinction spectra were recorded using an Agilent 8453 UV/Vis diode-array spectrophotometer. SERS spectra were recorded using a Renishaw InVia Raman microscope equipped with two Peltier-cooled CCD detectors, a Leica microscope with two gratings of 1200 and 1800 lines/mm and band-pass filter optics. Excitation lasers with emission wavelengths of 532, 633 and 785 nm were used and focused onto the sample through a 50× objective with N.A. 0.5. Effective irradiation powers were measured by a photodiode power sensor (PD300-3W, Ophir). SERS spectra in solution were collected by using a constant flux of power of $f = 1.5\, mW/s\mu m^2$ hitting the samples for all the lasers. For the detection limit study, the flux was kept constant and the integration time was adjusted according to the concentration of analyte. The samples were irradiated with 633 nm excitation wavelength for 5, 50 and 500 seconds for analyte concentrations of 10^{-7}, 10^{-8} and 10^{-9} M, respectively. All SERS spectra recorded on substrate were averaged over 64 single spectra measured at different spots on the substrate. Typically, a 20×20 μm^2 area was chosen. Transmission electron microscopy (TEM) images were collected with a JEOL JEM-1400PLUS instrument operating at 120 kV. Scanning electron microscopy: (SEM) images were obtained using an ESEM Quanta250 FEG (FEI, The Netherlands).

Synthesis of Au NRs. The seeds were prepared by the standard CTAB/$NaBH_4$ method: 25 μL of a 0.05 M $HAuCl_4$ solution was added to 4.7 mL of 0.1 M CTAB solution; 300 μL of a freshly prepared 0.01 M $NaBH_4$ solution was then injected under vigorous stirring. Excess borohydride was consumed by keeping the seed solution for 30 min at room temperature prior to use. Gold nanorods were prepared, with some modifications, as previously described by Murray and co-workers. In a typical synthesis of a 50 mL NR solution, 45 mg of 5-bromosalicylic acid was added to 50 mL of 0.05 M CTAB. The solution was mildly stirred for 15 min until complete dissolution, and 480 μL of 0.01 M $AgNO_3$ and 500 μL of 0.05 M $HAuCl_4$ solution were added to the mixture. After 30 min at 25°C, 130 μL of 0.1 M ascorbic acid solution was added under vigorous stirring, followed by 80 μL of seed solution. The mixture was left undisturbed at room temperature for at least 4 h. Then, an additional aliquot of 120 μL of 0.1 M ascorbic acid solution was added to the AuNRs suspension. After 4 h, the resulting gold nanorods presented an LSPR band centered at 720 nm. At this point, the NRs were washed twice by centrifugation (6000 rpm, 30 min). Finally, they were redispersed in 10 mL of 1 mM CTAB solution.

Synthesis Au NTs. AuNTs were prepared following the procedure by Scarabelli *et al.*[77] Briefly, Au seed@CTAC were prepared adding, under vigorous stirring, 300 µL of a 0.01 M $NaBH_4$ solution to a 4.7 mL solution 0.1 M in CTAC and 0.25 mM in $HAuCl_4$. The prepared seeds were aged for 2 h at room temperature and then diluted 10 times in CTAC 0.1 M before proceeding. In order to prepare 10 mL of AuNT solution we proceeded as follows. Two growth solutions were simultaneously prepared, the first one (1) made of 8 mL of Milli-Q water, 1.6 mL of a 0.01 M CTAC solution, and 40 µL of a 50 mM $HAuCl_4$ solution, and the second one (2) made of 10 mL of 0.05 M CTAC, 125 µL of a 50 mM $HAuCl_4$ solution and 75 µL of a 0.01 M NaI solution. 40 and 100 µL of a 0.1 M ascorbic acid solution were added to solution (1) and (2) respectively, and manually mixed until complete disappearance of the yellow color (few seconds). Immediately after reaching complete transparency, 100 µL of the diluted seed@CTAC was added to solution (1). After manually stirring the solution for 1 or 2 seconds, 1.2 mL of solution (1) was injected into solution (2) and manually stirred for few seconds. The growing particles were then left set undisturbed for at least one hour before characterization. The shape-yield in AuNT was about 60%. In order to separate the by-product, 2.75 mL of a concentrate CTAC solution (25% in weight, ca. 0.78 M) was added to the AuNT solution; the entire mixture was transferred to a cylinder and left undisturbed overnight. Interparticle depletion forces drove the flocculation and precipitation of the AuNTs. The supernatant (pink-purple) was discarded, and the precipitate (forming a black patina at the bottom of the cylinder) was redispersed with 4 mL of CTAB 0.05 M, immediately giving rise to a deep blue coloration. The produced AuNTs presented a plasmon band centered at 640 nm. Finally, the AuNTs were centrifuged twice (4500 rpm 20 min) and concentrated 20 times at 1mM concentration of CTAB.

Synthesis AuNSs. AuNSs were prepared following a seeded growth method. First, small gold seeds were prepared by the standard CTAC/$NaBH_4$ procedure: 50 µL of a 0.05 M $HAuCl_4$ solution was added to 4.7 mL of 0.1 M CTAC solution; 200 µL of a freshly prepared 0.01 M $NaBH_4$ solution was then injected under vigorous stirring.

After 2 minutes, 50 µL of seed were diluted ten times with 0.1 M CTAC solution, and added under stirring to 50 mL of 25 mM CTAC, 0.2 mM $HAuCl_4$ and 0.32 mM AA solution to prepare 20 nm spheres. The mixture was left undisturbed for at least 10 min. In the case of 45nm and 90 nm spheres, 1250 µL and 250 µL of the 20 nm suspension were added to 50 mL of 25 mM CTAC, 0.2 mM $HAuCl_4$ and 0. 2 mM AA solution. The mixture was heated up to 70 °C for 30 min. Finally, once the growth process was completed (after 10 min in the particular case of the 45 nm NSs, 30 min for the 90 nm NSs), 750 µL of 1M NaBr and 40 µL of $HAuCl_4$ 0.05M solutions were added to the mixture and allowed to cool down at room temperature. After 30 min, 45 nm and 90 nm spheres were washed three times by centrifugation (3000 rpm and 1500 rpm respectively, 20 min). AuNSs were then redispersed in 50 mL of 50 mM CTAB solution after the first washing. Finally, they were redispersed in 2.5 mL of 1 mM CTAB solution.

Citrate stabilization of AuNPs. Citrate stabilized AuNPs were prepared following a modified procedure of Mehtalla *et al.*[184] Typically, 5 mL of concentrated AuNPs in 1 mM CTAB were diluted with 5 mL of water and then added under stirring to 40 mL of poly(sodium 4-styrenesulfonate solution (0.15 wt.% in water). Subsequently AuNPs were incubated for 1h and then centrifuged and redispersed again in 40 mL poly(sodium 4-styrenesulfonate) solution. After a second centrifugation step, AuNPs were redispersed and incubated for 12 h in 40 mL of 5 mM sodium citrate solution. The AuNPs suspension was washed with citrate once again and concentrated one thousand times.

Preparation of substrates. Each glass slide was first treated with piranha solution (H_2SO_4/H_2O_2 3:1) for 60 min, then rinsed with abundant distilled water and dried under with N_2. The substrates were then immersed in an APTES/EtOH solution (5% v/v) for 60 min. After washing with ethanol to remove excess APTES and drying under N_2, they were soaked in the NP colloids for 60 min, followed by rinsing with distilled water and drying under N_2. The concentration of Au^0 in all cases was 10mM. Prior to SERS experiments, so-prepared substrates were incubated in the analyte solution for 60 min, followed by rinsing with distilled water and drying with N_2.

CHAPTER 5

MULTIFUNCTIONAL SELF-ASSEMBLED COMPOSITE COLLOIDS AND THEIR APPLICATION TO SERS DETECTION

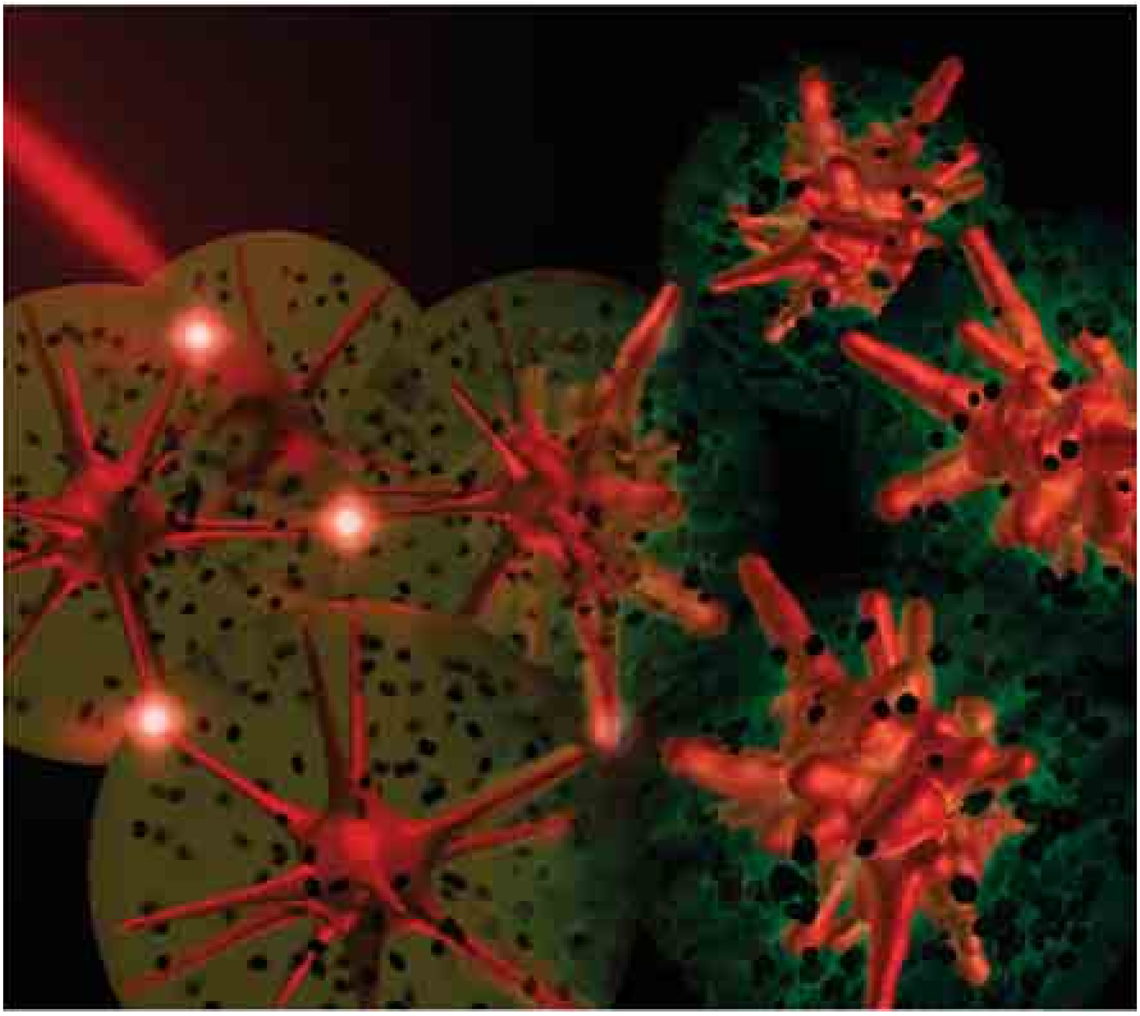

Abstract

In this method a simple method is presented for the co-encapsulation of gold nanostars and iron-oxide nanoparticles into hybrid colloidal composites that are highly responsive to both light and external magnetic fields. Self-assembly was driven by hydrophobic interactions between polystyrene capped gold nanostars and iron oxide nanocrystals stabilized with oleic acid, upon addition of water. A block copolymer was then used to encapsulate the resulting spherical colloidal particle clusters, which thereby became hydrophilic. Electron microscopy analysis unequivocally shows that each composite particle comprises a single Au nanostar surrounded by few hundreds of iron oxide nanocrystals. We demonstrate that this hybrid colloidal system can be used as an efficient substrate for surface enhanced Raman scattering, using common dyes as model molecular probes. The co-encapsulation of iron oxide nanoparticles renders the system magnetically responsive, so that application of an external magnetic field leads to particle accumulation and limits of detection in the nanomolar range.

5.1 Introduction

The combination of several functions within a single colloidal object has been proposed as a means to expand the potential applications of nanomaterials. A prototypical example of this class of systems is the integration of optical and magnetic properties, which has been achieved via different strategies.[105,185–189] Most of these methods however require either chemical reactions to be carried out on pre-formed colloids, or the irreversible assembly/aggregation of particles that are synthesized independently. The former method usually leads to poorly defined morphologies, whereas the latter results in rather large supra-particles. Recent progress on directed self-assembly has demonstrated that application of hydrophobic interactions may lead to the reversible assembly of plasmonic nanoparticles (NPs) of various morphologies and sizes.[190] An additional challenge was the application of the same concept to the reversible assembly of particles with dissimilar composition and surface chemistry. We were interested in applying this concept toward the formation of multifunctional assemblies that could retain small sizes, which are required for example in most biological applications. In particular, the incorporation of plasmonic and magnetic NPs offers several advantages, such as multimodal imaging capabilities or magnetic manipulation and increased detection sensitivity. A similar concept has been applied in the past toward the improvement of sensing and detection based on surface enhanced Raman scattering (SERS).[42,143] For example, microgels containing iron oxide and silver NPs were shown to allow the capture of various analytes and ultrasensitive detection,[191] whereas silica-coated iron oxide spindles covered with a dense layer of gold nanorods could be accumulated on a tiny spot, increasing SERS sensitivity as compared to gold nanorods alone.[192] The latter case is based on the aggregation of the NPs induced by an external magnetic field, so that additional hot-spots are created and a larger amount of sample is probed, leading to a lower limit of detection when using very small amounts of analyte. The recent development of colloidal synthesis methods has allowed a detailed comparison of the efficiencies of metal NPs with different morphologies as SERS enhancers. It is commonly accepted that spheres are only efficient when forming aggregates,[119,193,194] whereas nanorods,[195–197] nanocages or nanoplates[182,198,199] can perform even as single particles in solution. The most efficient performance thus seems to be related to the presence of sharp tips and therefore nanostars have been identified as displaying the optimum morphology for SERS enhancement.[200–202]

In this context, we present here a method to prepare colloidal hybrid assemblies that are stable in aqueous solution, while displaying interesting optical and magnetic properties, by co-encapsulation of gold nanostars and iron oxide nanocrystals within a protecting layer of poly(styrene)-block-poly(acrylic acid) (PS-b-PAA). Such a hybrid assembly combines the plasmonic properties characteristic of Au nanostars with the response to external magnetic fields provided by the presence of the superparamagnetic iron oxide NPs. This magnetic-plasmonic system was applied to the SERS detection of model molecular dyes. Interestingly, by applying magnetic accumulation, limits of detection in the nM range could be achieved.

5.2 Results and Discussion

The starting building blocks for the targeted composite colloids are gold nanostars (AuNSs)[69] and iron oxide NPs (Fe_3O_4 NPs).[203] Fe_3O_4NPs (7.0±0.6 nm, Figure 5.1a) were stabilized with oleic acid and thus intrinsically hydrophobic after synthesis and stable in pure THF. AuNSs (110.2±16.1 nm, Figure 5.1b) were initially capped with the cationic surfactant cetyltrimethylammonium bromide (CTAB) and subsequently mixed with an excess (~5 molecules per nm^2) of thiol-terminated polystyrene (PS, Mw = 53 kg mol^{-1}), leading to ligand exchange. This process yielded hydrophobic AuNSs that were also colloidally stable in THF.

The formation of magnetoplasmonic assemblies was based on a recently reported encapsulation strategy, in which polymeric micelles play a role of protecting layers.[204] The process involves the addition of water (10 wt%) to the THF solution containing a stable mixture of AuNSs, Fe_3O_4 NPs and the linear block copolymer (PS-*b*-PAA) (Figure 5.1c). Water addition resulted in a gradual variation of the polarity of the mixture, thereby driving co-aggregation of all three components mediated by hydrophobic interactions. To ensure the incorporation of Fe_3O_4 NPs at the void space between the spikes of AuNSs, an excess of Fe_3O_4 NPs was used as compared to NSs. Since hydrophobic interactions are not directional, the resulting assembled mixture contained three different types of colloidal nanostructures after aggregation: (i) empty copolymer micelles, (ii) polymer-encapsulated spherical aggregates of Fe_3O_4 NPs, and (iii) single AuNSs co-encapsulated within polymeric micelles containing a large number of small Fe_3O_4 NPs. Because of the larger mass of AuNSs, centrifugation could be readily used to remove both empty micelles and micelles containing iron oxide NPs only, effectively resulting in the purification of the bifunctional clusters (Figure 5.1d). The final product thus consisted of individual AuNSs co-encapsulated with surrounding magnetic NPs. These encapsulated magnetic-plasmonic micelles exhibit excellent colloidal stability in water because the outer polymer layer comprises the hydrophilic PAA blocks.[205]

Morphological characterization by transmission electron microscopy (TEM) confirmed that each NS was individually encapsulated in a polymeric micelle (143.1±11.2 nm total diameter), which also contained clearly visible spots corresponding to Fe_3O_4 NPs (Figure 5.1e). In addition, high angle annular dark field scanning TEM (HAADF-STEM) was used for detailed analysis of individual clusters. As shown in Figure 5.1f, the micelle comprises a bright central object corresponding to AuNSs, surrounded by satellite Fe_3O_4 NPs. Electron tomography and three-dimensional reconstruction of the same particle provided clear information on the spatial distribution of the NPs in three dimensions. As shown in Figure 5.1g, the AuNS (in blue) and the

Fe_3O_4 NPs (in red) are homogeneously distributed within the inner space of the micelles. Interestingly, the spikes of the AuNSs consistently appear to stick out of the polymeric envelope, as previously reported for single AuNSs.[204] The gaps between the particles confirm the presence of polymeric capping agents, while image analysis in 3D allowed us to estimate the presence of 200-300 Fe_3O_4 NPs per cluster.

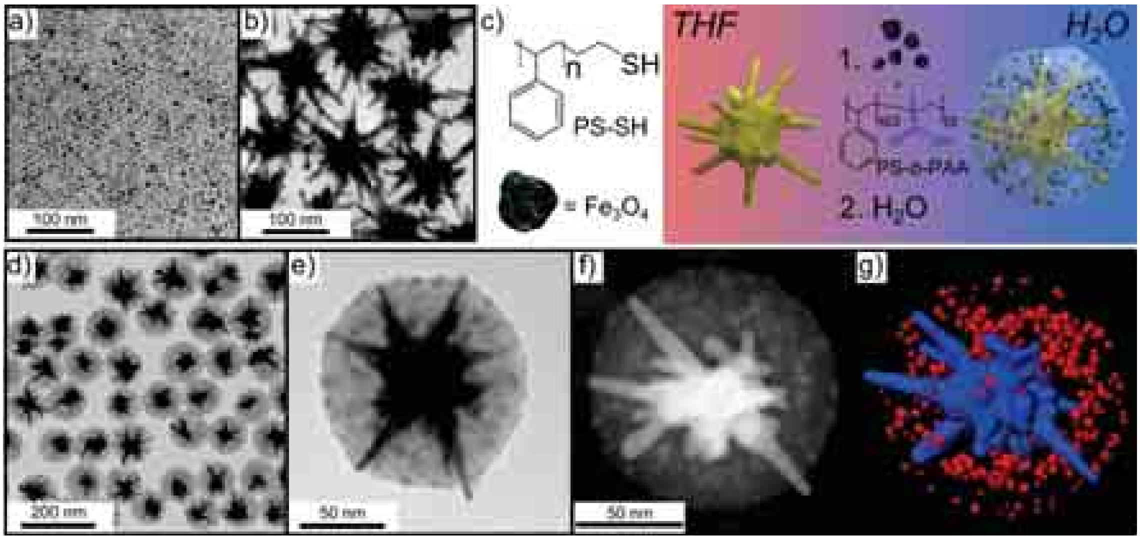

Figure 5.1. (a,b) TEM images of oleic acid-capped iron oxide NPs (a) and polystyrene-stabilized AuNSs (b). (c) Scheme illustrating the encapsulation process. (d,e) TEM images of hybrid colloidal assemblies at different magnifications. (f) HAADF-STEM image of an individual composite particle. (g) Three-dimensional electron tomography reconstruction of an individual cluster showing the AuNS in blue and Fe_3O_4 NPs in red.

The metallic cores of the magnetoplasmonic assemblies define the optical response of the system. As compared with individual AuNSs, increased absorbance was registered below 600 nm, due to enhanced light scattering by the presence of the polymeric shell, as well as some absorption by Fe_3O_4NPs, at wavelengths shorter than the localized surface plasmon resonances (LSPR) of AuNSs (Figure 5.2a). On the other hand, the copolymer shell and the Fe_3O_4 NPs increase the refractive index around the surface of the NSs, leading to a redshift of the LSPR maximum by 55 nm.[204] The magnetic response of the magnetoplasmonic micelles can be readily observed by the naked eye. Application of a hand-held magnet for 2 hours next to the colloid containing the hybrid clusters induces a clear separation of the particles and accumulation on the vial wall (Figure 5.2b).

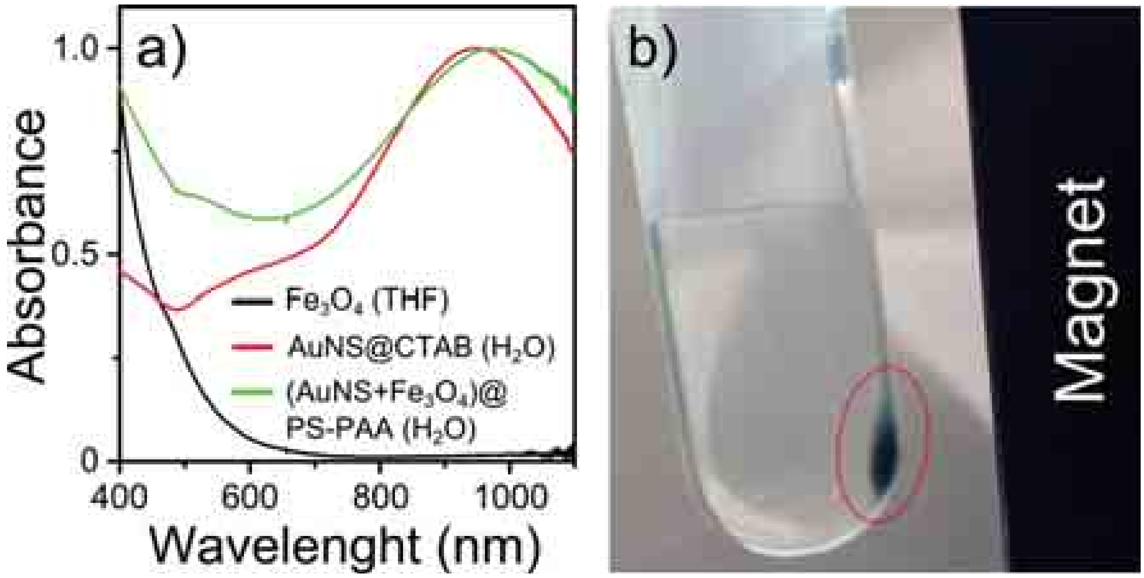

Figure 5.2. (a) UV-Vis spectra of CTAB-stabilized AuNSs in water (red line), Fe_3O_4 NPs stabilized with oleic acid in THF (black line) and the composite clusters in water (green line). (b) The stable colloid of hybrid clusters phase separates upon application of an external magnetic field.

The sharp spikes of AuNSs branching out of the polymeric micelle were expected to provide sufficient electric field enhancement to serve as efficient substrates for SERS. This was analyzed by means of the experimental design schematically shown in Figure 5.3. In a typical experiment, the mixture (20 μL) containing hybrid colloidal clusters and the desired concentration of analyte molecules was placed inside a glass tube (~1 mm internal diameter) and sealed at both ends. Such an experimental configuration was designed to prevent solvent evaporation and ensure a constant concentration of the analyte during the entire measurements. SERS spectra were acquired in the absence and in the presence of an external handheld magnet (Figures 5.3a,b).

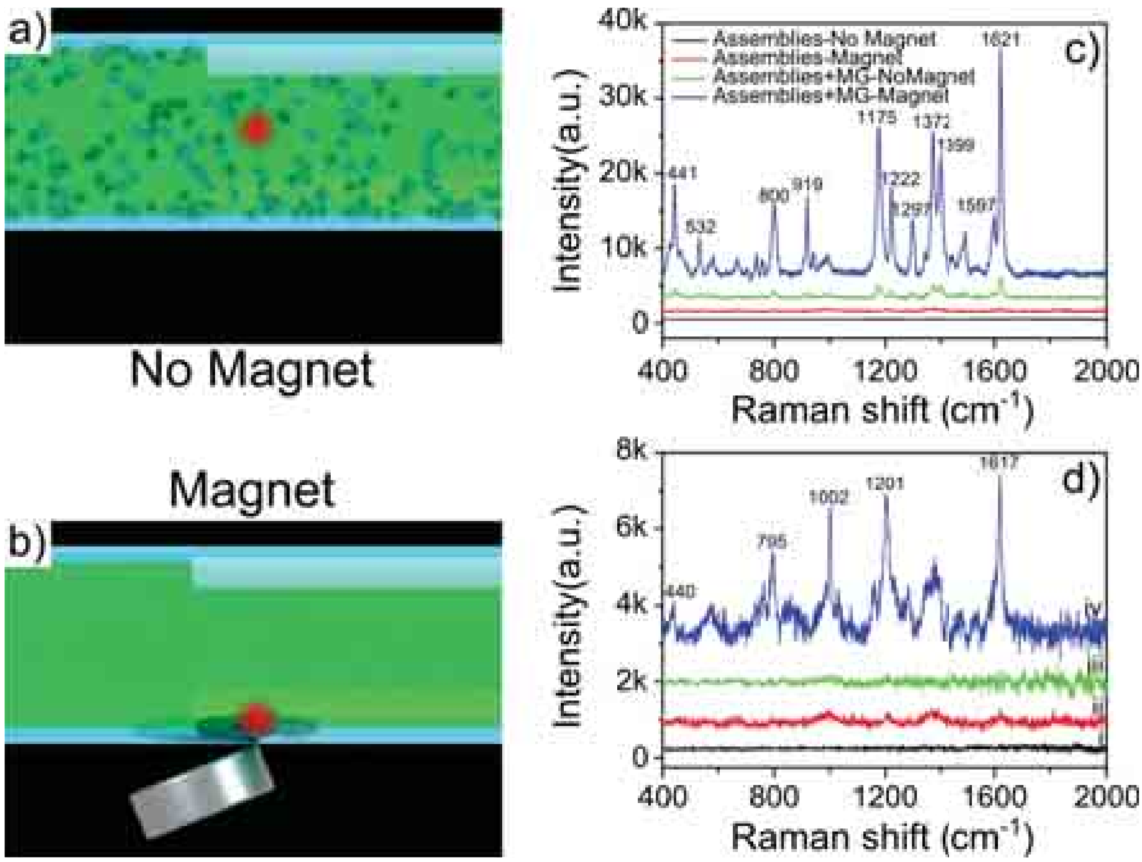

Figure 5.3. Schematic representation of the experimental setup for magnetic field assisted SERS detection. The mixture of hybrid clusters and analyte is placed inside a glass tube and SERS measurements are performed either in the presence or in the absence of a handheld magnet (a,b) by using different focal points for the two configurations. SERS spectra in (c) show a strong signal enhancement upon application of the external magnetic field and particle accumulation. The flat spectra of the assemblies without analyte (black and red lines) confirm that the recorded peaks stem from Malachite Green (MG). (d) SERS spectra of the magnetoplasmonic assemblies without analyte. By irradiating the sample with 0.61 mW there is no signal detected without magnetic field (i) and very weak peaks once it is applied (ii). On the other hand, by increasing the power at 5.93 mW there are again no peaks visible with no magnet (iii) but it is possible to distinguish clearly several features after assemblies aggregation (iv).

It is worth mentioning that the laser focal point was adjusted in each case, so that in the absence of magnetic field the focus was at the center of the tube but upon application of the magnet it was shifted to the bottom of the tube, where particles aggregate (red dots in Figures 5.3a,b). The small volume of the sample and the strong magnetic response of the particles allowed complete aggregation of the particles and accumulation at the glass tube wall within a short time, ~2 minutes.

Representative SERS spectra are displayed in Figure 5.3c before and after addition of Malachite Green (MG), with and without applied magnetic field, revealing a significant intensity difference depending on the aggregation state of the NPs. Under external magnetic field, the hybrid clusters form a compact aggregate at the inner wall, leading to signal accumulation and increase of the electric near field, thereby further enhancing the SERS signal.[66,206] To avoid potential contamination of the SERS signal by polystyrene peaks the laser power was kept relatively low (0.61 mW) and an integration time of 10 s was used. At such conditions no peaks from polystyrene were observed even after magnetic field accumulation (Figure 5.3d). This is clearly exemplified for MG in Figure 5.3, as its primary vibrations can be readily identified in the SERS spectra, related to stretching (C-C) at 1297, 1597 and 1621 cm^{-1}, stretching (N-phenyl) at 1372 and 1399 cm^{-1}, in plane bending (C-H) at 1175 and 1222 cm^{-1}, ring skeletal vibration of radical orientation at 532 and 919 cm^{-1}, out of plane bending (C-H) at 800 cm^{-1} and out of plane bending (phenyl - C^+ - phenyl) at 441 cm^{-1}.[207,208] Detailed peak assignment is given in Table 5.1. Although the peaks for MG are present both with and without applied magnetic field, a significant signal enhancement was obtained by magnetic accumulation. These results thus confirm that the applied magnetic field can remotely activate the formation of hot spots and increase analyte concentration, thus providing a convenient scenario for ultrasensitive detection.

Table 5.1. Assignment of the main vibrations for MG and CV.

Malachite Green *cm^{-1}*	***Crystal Violet*** *cm^{-1}*	*Assignment*
	339	ipδ(Φ - C$^+$ - Φ)
441	438	oopδ(Φ - C$^+$ - Φ)
532	527	ring skeletal vib. of radical orientation
	558	ring skeletal vib. of radical orientation
581	604	ring skeletal vib. of radical orientation
737	723	oopδ(C-H)
752	758	oopδ(C-H)
800	800	oopδ(C-H)
919	913	ring skeletal vib. of radical orientation
942	942	ring skeletal vib. of radical orientation
993	974	ring skeletal vib. of radical orientation
1175	1174	ipδ(C-H)
1222		ipδ(C-H)
1297	1298	ν(C-C)
1372	1372	ν(N-Φ)
1399		ν(N-Φ)
1444	1441	ν(C-C) + ring def.
1493	1477	ν(C-C) + ring def.
	1531	ν(C-C)
1597	1586	ν(C-C)
1621	1618	ν(C-C)

The contribution toward enhancement of the Raman signal by the local increase of analyte molecules and by hot spot formation in between AuNSs was further studied using magnetic micelles containing Fe_3O_4 NPs only. These AuNS-free micelles respond to the external magnetic field in a similar fashion as those containing AuNS. Figure 5.4 shows a comparison of Raman and SERS spectra for both micellar systems. In the absence of magnetic field no Raman peaks were recorded for the solution containing 10 nM MG. Magnetic accumulation of the assemblies makes possible the detection of analyte molecules only when the micelles containing AuNSs together with Fe_3O_4 NPs were used (Figures 5.4a,b). These results confirm the role of AuNSs as essential components of the SERS substrates. By combining magnetic and optical activity, the analyte concentration at the illumination volume can be increased by magnetic accumulation and exploit the surface plasmon electric field enhancement at the AuNSs tips for efficient SERS.

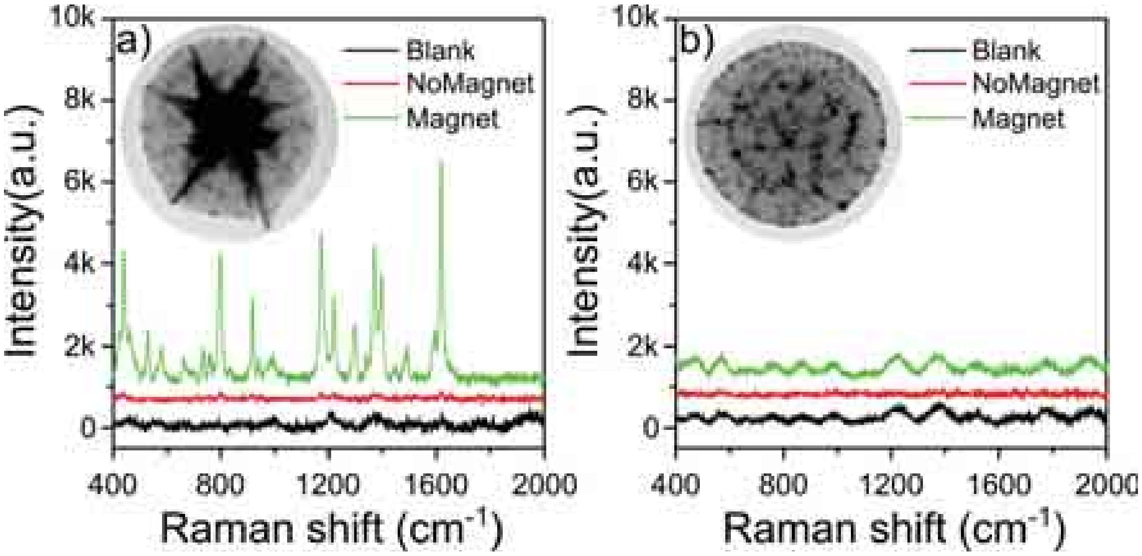

Figure 5.4. SERS spectra of MG in the presence of magnetic-plasmonic micelles (a) and magnetic micelles (b). The presence of the plasmonic AuNS core is crucial to sufficiently enhance the Raman signal. The blanks correspond to a magnetically aggregated sample with no dye.

Since the outer PAA polymer shell displays a negative value of ζ-potential (-25 mV), we hypothesize that analyte molecules with negative functional groups will be repelled from the micelle surface whereas molecules with positive functional groups adsorb onto the outer polymer surface. Such different interactions between analyte molecules and polymer surface ultimately determine the ability of the clusters for magnetic separation and SERS detection. This hypothesis was tested by comparing Malachite Green as positively charged probe and Trypan Blue (TB) as negatively charged analyte. A mixture containing the colloidal clusters and the analyte molecules (10^{-5} M) was decanted with the help of an external magnet and then redispersed in pure water. The washing cycle was repeated three times. After each washing step, SERS spectra were recorded in the presence and the absence of an external magnetic field.

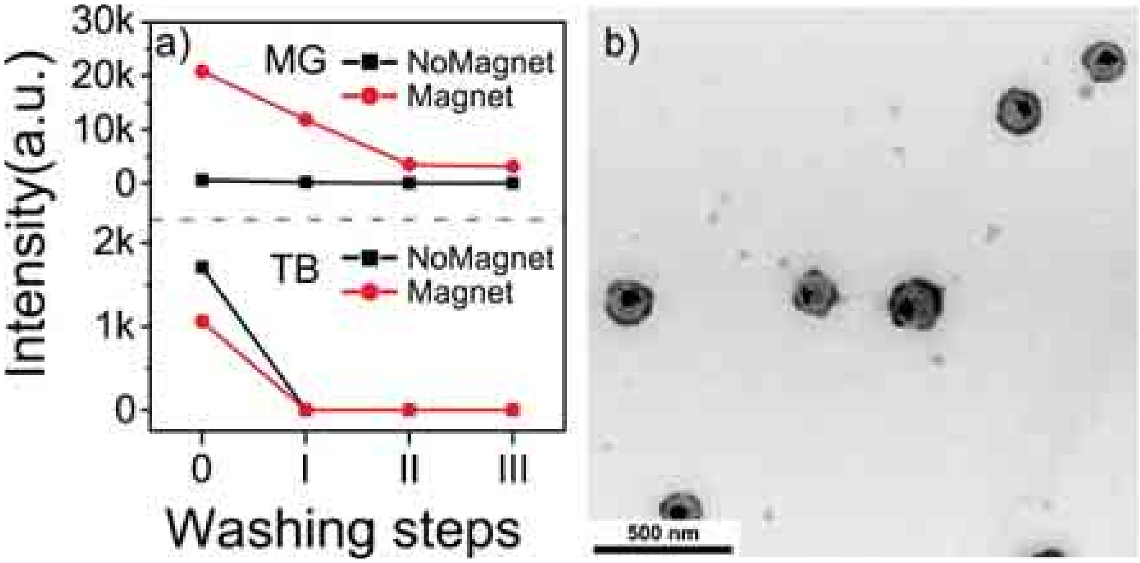

Figure 5.5. (a) SERS intensity of characteristic vibrations of MG and TB (919 and 1570 cm^{-1}, respectively) vs. number of washing steps. Data were recorded before (black) and after (red) collecting the assemblies by applying an external magnetic field. Progressive decrease of the SERS intensity was observed for MG as compared to a steep drop for TB, suggesting the preferential adsorption of positively charged dye molecules on the surface of the negatively charged polymer micelles. (b) TEM image of the hybrid clusters after a typical SERS experiment, showing the adsorption of the positive molecular probe (MG) in the form of a molecular shell.

The results in Figure 5.5a show that for MG the peak intensity was higher under magnetic field, indicating co-accumulation of the analyte molecules and magnetic particles. After subsequent washing steps, the peak intensity progressively decreased. The peak intensity however remained constant (nearly zero) after washing when no magnetic field was applied. The difference of Raman intensities between aggregated and dispersed modes suggests that MG molecules do adsorb onto the surface of the micelles, but can be gradually washed away. TEM analysis additionally confirmed the formation of a molecular shell around the hybrid clusters after treatment with MG molecules (Figure 5.5b). In the case of negatively charged TB, we found that the SERS intensities from the initial mixture were higher in the absence of a magnetic field (Figure 5.5a). This counter-intuitive observation is explained by the fact that the magnetic aggregation of the clusters may lead to expelling weakly bound TB molecules into the bulk solution. This behavior thus suggests that the micelles cannot accumulate TB molecules by induced phase separation. After the first washing step, the Raman intensity dropped to zero regardless of the external magnetic field, confirming the lack of retention of the analyte molecules on the surface of magnetomicelles. These results constitute a step toward understanding the surface chemistry of the clusters and may be of help when devising biomolecule detection protocols.

We finally evaluated the detection limit for MG and crystal violet (CV) as model (positively charged) probe molecules (Figure 5.6). The SERS spectra were recorded under applied magnetic field and taking as a reference the intensity of the 919 cm^{-1} and 913 cm^{-1} peaks for MG and CV, respectively. These peaks were selected to avoid potential interference with the peaks from polystyrene (795 cm^{-1}, 1002 cm^{-1} and 1200 cm^{-1}), which are visible at the relatively high laser power (5.93 mW) and prolonged accumulation time (30 s) used in these experiments. The peaks corresponding to polystyrene however could only be detected in the presence of external magnetic field. Under these conditions we obtained safe limits of detection of 5 nM for MG and 10 nM for CV, thus confirming the ultradetection capability of this system.

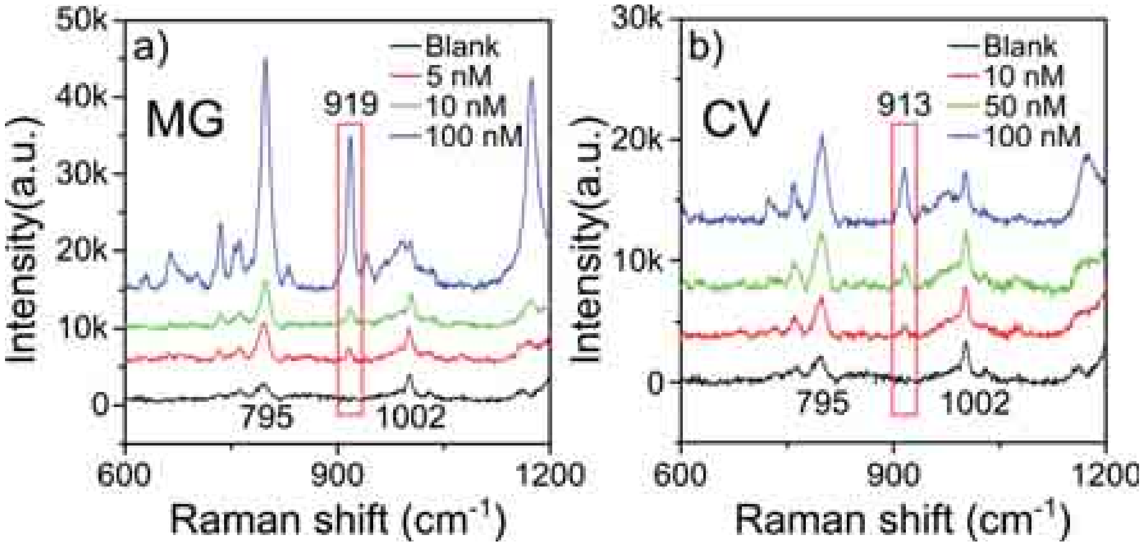

Figure 5.6. Limit of detection analysis under magnetic field accumulation and higher laser intensity (5.93 mW). Limits of detection are found to be 5 nM for MG (a) and 10 nM for CV (b).

5.3 Conclusions

We have demonstrated that the concept of hydrophobic interactions as a driving force toward the reversible assembly of NPs can be safely applied to the co-encapsulation of NPs with dissimilar size, morphology, composition and surface chemistry. Simple addition of water to a mixture of AuNSs and Fe_3O_4 NPs in THF allowed us to develop novel multifunctional nano-platforms that are responsive toward optical and magnetic stimuli, which was applied to SERS-based ultradetection. While the incorporation of a large amount of magnetic NPs in each capsule enables remote accumulation of adsorbed analyte molecules, the plasmonic AuNSs act as highly efficient substrates to enhance the Raman scattering signal, achieving detection limits in the nM range.

5.4 Experimental section

Chemicals. Hydrogen tetrachloroauratetrihydrate ($HAuCl_4 \cdot 3H_2O$, ≥99.9%), silver nitrate ($AgNO_3$, ≥99.0%), L-ascorbic acid (≥99%), iron chloride ($FeCl_3 \bullet 6H_2O \geq 99.9\%$), hydrochloric acid (HCl>99%) and sodium oleate were purchased from Aldrich. Thiol-terminated polystyrene (PS-SH) with a molecular weight of 53 kg/mol and diblock copolymer (polystyrene-b-polyacrylic acid, PS_{403}-b- PAA_{62}) were purchased from Polymer Source, Inc. All chemicals and solvents were used without further purification.

Synthesis of AuNSs. The surfactant-free method was used to prepare AuNSs[69]. A solution of gold seeds (~15 nm, [Au] = 0.5 mM, 0.5 mL) prepared by the Turkevich method[58] was added to a solution (50 mL) containing $HAuCl_4$ (0.25 mM) and HCl (1 mM), followed by addition of $AgNO_3$ (10 mM, 0.15 mL) and ascorbic acid (100 mM, 0.25 mL). To increase the stability of the obtained NSs, CTAB (100 mM, 2.5 mM) was added to the growth solution. Upon synthesis, the solution was centrifuged (4500 rpm, 30 min) to remove excess reactants, and redispersed in water.

Ligand exchange. The corresponding AuNSs colloid (5 mM, 1 mL) was added dropwise under sonication to a THF solution (10 mL) of PS-SH (5 molecules of PS-SH per nm^2 of gold surface). The solution was kept in an ultrasonic bath for 15 min. To ensure ligand exchange, the resulting mixture was left undisturbed for 12h, and then centrifuged twice. The particles were finally dispersed in THF (final concentration 5 mM).

Synthesis of Fe_3O_4 NPs. Fe_3O_4 NPs were prepared according to the method reported by Park et al.[203] The final concentration of Fe_3O_4 NPs in THF was 62 mg/mL.

Self-assembly of hybrid micellar clusters. In a typical assembly experiment, water (1 mL) was added dropwise to a mixture in THF containing AuNSs@PS (1.9 mL, 5.5 mM), PS_{403}-b- PAA_{62} (0.2 mL, 1.5 mg/mL) and Fe_3O_4 NPs (0.01 mL, 62 mg/mL) under magnetic stirring. Subsequently, the water content was increased up to 50 wt%, followed by increasing the temperature up to 50 ºC, which was maintained for 30 min. The final solution was centrifuged twice (3500 rpm, 20 min) and the particles redispersed in pure water at a concentration of [Au] = 0.5 mM.

Self-assembly of magnetic micelles. Water (1 mL) was added to a mixture in THF containing PS_{403}-b- PAA_{62} (0.2 mL, 1.5 mg/mL) and Fe_3O_4NPs (0.01 mL, 62 mg/mL) under magnetic stirring. Subsequently, the water content was increased up to 50 wt%, followed by increasing the temperature up to 50 ºC, which was maintained for 30 min. The final solution was centrifuged twice (3500 rpm, 20 min) and the particles dispersed in pure water.

Sample preparation for SERS measurements. The hybrid colloid ([Au]= 0.5 mM) and the desired amount of analyte were incubated for 2 hours to reach thermodynamic equilibrium. A small amount (20 µL) of the sample was then used to fill a thin glass tube (~1 mm internal diameter), which was sealed at both ends by parafilm®. A magnetic field we applied by putting a small commercial handheld magnet placed in contact with the tube. In order to avoid fluctuations in the SERS intensity due to the flow of NPs following the magnetic field, each sample was left in contact with the magnet during 15 minutes prior to recording the spectra. After this time no relevant changes in the intensities were observed.

Characterization. Optical extinction spectra were recorded using an Agilent 8453 UV/Vis diode-array spectrophotometer. SERS spectra were recorded using a Renishaw InVia Raman microscope equipped with two Peltier-cooled CCD detectors, a Leica microscope with two gratings of 1200 and 1800 lines/mm and band-pass filter optics. Excitation lasers with emission wavelengths of 633 and 532 nm were used and focused onto the sample through a 10× objective with N.A. 0.25, producing spot diameters of 3.1 and 2.6 µm for 633 and 532 nm, respectively. Except for the limit of detection experiment, all SERS spectra were collected with an integration time of 10 s, and the samples were irradiated with constant powers of 0.61 mW (633 nm) and 2.43 mW (532 nm). For the detection limit study, the samples were irradiated with 633 nm excitation at a constant power of 5.93 mW and 30s integration time. Transmission electron microscopy (TEM) images were collected with a JEOL JEM-1400PLUS instrument operating at 120 kV. In collaboration with the group of Prof. Sara Bals at Univesity of Antwerp, HAADF-STEM images and electron tomography tilt series were acquired using a double aberration corrected cubed FEI Titan 50-80 electron microscope operated at 300 kV. For the reconstruction of the series we used the SIRT algorithm, as implemented in the ASTRA toolbox.[209,210]

GENERAL CONCLUSIONS

The main goal of this PhD thesis was the development of new strategies to prepare highly efficient supports for SERS spectroscopy by exploiting the wide experience at the Bionanoplasmonics Laboratory (CIC biomaGUNE), on the synthesis of metal nanoparticles. By applying different approaches like directed self-assembly, magnetic accumulation and surface functionalization, we were able to accomplish the objective. A general and short summary of the specific results achieved in this thesis is presented herein.

- ✓ The specific diameter of Au nanowires vertically grown from a solid support can be finely tuned through the ratio between mercaptobenzoic acid (MBA) and borohydride during the synthesis. This aspect, together with the precise control over the length of the wires by stopping the reaction at the appropriate time, offers the possibility to tailor the plasmon band of the substrate at a desired position in the electromagnetic spectrum. We additionally demonstrated the efficiency of plasma cleaning to remove MBA from the metallic surface and to use the nanowires as SERS substrates. 1-Naphthalenethiol could be detected both from solution and from the gas phase, down to a concentration of 10^{-6} M. We also demonstrated the possibility to detect multiple analytes by cyclic plasma cleaning processes and incubation into solutions of different molecules.
- ✓ Standard commercial paper has been shown to be suitable as inexpensive SERS support for the adsorption of nanoparticles. Paper fibers loaded with both Ag and Au nanoparticles were prepared by using a fountain pen where the nanoparticle colloids were employed as ink. Cheapness is not the only advantage of this system. From the point of view of the SERS performance, a detection limit down to 10^{-12} M was reached for Rhodamine-6G. Even though each SERS area was prepared by simply hand-writing on the paper sheet, a high degree of uniformity and reproducibility was observed for each of the analyzed samples.

Detection of the fungicide Thiabendazole has been finally demonstrated with Ag nanospheres.

- ✓ Both isotropic and anisotropic Au nanoparticles such as nanorods, nanotriangles and nanospheres have been employed to study in detail the role of surfactants toward obtaining high enhancement factors in SERS experiments. By comparing these three morphologies coated with either CTAB or citrate, we could improve the measured SERS intensity in solution of CV adsorbed onto citrate-stabilized nanotriangles. By properly adjusting the experimental conditions, a limit of detection of 10^{-9} M was reached for CV. In order to further characterize these citrate-stabilized NPs we also prepared densely packed monolayers onto a glass slide, which showed a strong SERS efficiency when irradiated with the 633 nm excitation wavelength. Differently from experiments in solution, measurements on these NPs monolayers revealed that nanospheres are the most efficient choice to obtain SERS intensities which were about five-fold larger than those obtained with nanorods.
- ✓ A hybrid approach was adopted to develop a new kind of SERS platforms. The optical properties of Au nanostars and the magnetic behavior of Fe_3O_4 nanocrystals were joined together to form a stable colloidal solution of magneto-optical composites. From HAADF-STEM analysis it is possible to see that each individual nanostar is surrounded by hundreds of magnetic NPs. We showed that it was possible to increase the detected SERS intensity of the analyte under study by magnetically-induced accumulation of the nanocomposites. The particular morphology of these nanostructures facilitated the deposition of the probe in close proximity to the nanostar tips, where the electric field enhancement is several orders of magnitude more intense than anywhere else.

According to the results presented in this research work, this thesis is expected to be helpful toward the development of more efficient SERS substrates, thus improving the analytical power of this technique in the detection of challenging molecules at low concentrations.

RESUMEN

CONTROL RACIONAL SOBRE LA MORFOLOGÍA Y LA ORGANIZACIÓN DE NANOESTRUCTURAS DE ORO PARA DETECCIÓN POR SERS

Con este resumen se pretende ofrecer una visión global del trabajo presentado en los diferentes capítulos de esta tesis. El objeto de estudio de esta tesis ha sido el desarollo de nuevos sistemas basados en el uso de nanoestructuras de oro para detección mediante dispersión Raman aumentada por superficie (SERS). Se han desarollado diferentes técnicas para favorecer el ensamblaje de nanopartículas de forma controlada, con el objetivo de aumentar la intensidad de la señal Raman. Mediante microscopía electrónica se han caracterizado las diferentes nanoestructuras obtenidas, las cuales se han empleado como sustratos SERS para detectar concentraciones de analito en el rango nanomolar.

6.1 Objetivos

El uso de nanoestructuras metálicas en SERS ha permitido superar la principal limitación de la espectroscopía Raman convencional: la baja intensidad registrada. Entre todos los metales, oro y plata resultan ser los más adecuados debido sus peculiares propiedades ópticas. El objetivo principal de esta tesis es pues la fabricación de nuevos sustratos para SERS que sean altamente eficientes y permitan identificar y cuantificar diferentes especies químicas a concentraciones cada vez más bajas. El contenido de cada capítulo se justifica brevemente a continuación.

En el Capítulo 1 se describen consideraciones generales sobre el efecto Raman y espectroscopía SERS, de forma que se facilita la comprensión de conceptos teóricos básicos sobre esta espectroscopía. Se analizan además las propiedades ópticas de las nanopartículas de oro y plata, ya que estos son los materiales más empleados en SERS, y se ofrece una visión general sobre los procedimientos más comunes para la fabricación de substratos SERS, presentando a su vez una serie de ejemplos representativos.

En el Capítulo 2 se establece un método químico para obtener subtratos para SERS basados en nanohilos de oro mediante el crecimiento vertical de semillas de oro depositadas sobre un soporte de vidrio. El mecanismo de crecimiento altamente anisótropo da como resultado una monocapa de nanohilos de oro muy densa que presenta interesantes propiedades plasmónicas. Controlando la longitud y el diámetro de los nanohilos, es posible ajustar la posición de la banda plasmónica, determinando así la morfología óptima para SERS. Como aplicación particular de este sistema se ha demostrado la detección de analitos en fase gaseosa.

En el diseño y la fabricación de substratos SERS, además de la eficiencia, es necesario considerar otros aspectos, como son el bajo coste y la facilidad del proceso de fabricación. De esta forma, en el capítulo 3 se emplea un tipo estándar de papel industrial como soporte sólido para la adsorción de nanopartículas plasmónicas. Sin necesidad de tratamiento adicional, las fibras de papel son recubiertas completamente con nanopartículas, de forma que pueden usarse directamente como soportes para SERS. Utilizando una simple pluma estilográfica se han podido depositar las nanopartículas en forma de tinta, obteniéndose así substratos SERS flexibles y uniformemente cargados de partículas sin necesidad de emplear ninguna instrumentación sofisticada.

La eficiencia en SERS de un sustrato depende fuertemente de los agentes estabilizantes utilizados en la síntesis de las nanopartículas. Moléculas con alta afinidad por el metal evitan que el analito esté próximo a la superficie de las nanopartículas, donde se produce el campo eléctrico responsable de la detección SERS. En el capítulo 4 se introduce un método que permite sustituir el agente estabilizante que recubre la superficie de diferentes nanopartículas de oro, facilitando de esta forma la adsorción del analito. Se han podido comparar varias morfologías de partículas con el mismo recubrimiento químico, llegándose a alcanzar límites de detección en el rango nanomolar.

Las propias soluciones coloidales también pueden ser utilizadas como sustratos SERS. Este enfoque representa una alternativa válida a los mencionados soportes sólidos, ya que presenta varias ventajas como son la reducción de la degradación de la muestra o la mejora de la uniformidad en la distribución del analito. Así, en el capítulo 5 se introduce un sustrato SERS híbrido que combina las propiedades ópticas de nanopartículas de oro y la respuesta magnética de nanocristales de magnetita. De esta forma, gracias a la aplicación de un campo magnético externo se ha conseguido aumentar con éxito la sensibilidad por SERS en varios órdenes de magnitud.

En su conjunto, se espera que esta tesis pueda contribuir de forma significativa al desarrollo de nuevas nanoplataformas plasmónicas como sustratos de SERS sensibles y fiables, para la detección de analitos en diversos campos de aplicación.

6.2 Introducción

Desde su descubrimiento, la espectroscopía SERS se ha convertido en una de las más potentes técnicas de análisis. La principal ventaja de SERS se basa en el uso de potenciadores metálicos, que ofrecen la posibilidad de aumentar el campo eléctrico responsable del efecto Raman en varios órdenes de magnitud. Cuando un campo eléctrico externo interactúa con la nube electrónica de un metal, el efecto resultante es una oscilación de estos electrones a la misma frecuencia que el campo incidente. Estas oscilaciones, conocidas como plasmones, tienen un papel clave en el proceso SERS. Las nanopartículas metálicas representan la clase más importante de potenciadores ópticos debido al alto control sobre su morfología, tamaño y organización sin necesidad de instrumentación costosa. Entre todos los metales, oro y plata son los más utilizados debido a sus propiedades ópticas especiales. Hoy en día se puede obtener una amplia variedad de formas simplemente ajustando los parámetros de síntesis: esferas, cilindros, triángulos, estrellas, hilos, pirámides, etc. Se ha demostrado que, en las condiciones experimentales adecuadas, el campo eléctrico incidente se puede aumentar localmente de forma que la señal de Raman mejora hasta 10^8-10^{11} veces, abriendo incluso la posibilidad de detección de moléculas individuales.

Debido a la potencia analítica de la espectroscopía SERS, se han realizado numerosos estudios para obtener sustratos SERS fiables. Aparte de la eficiencia en la detección, un buen soporte de SERS tiene que garantizar un alto grado reproducibilidad y de uniformidad sobre el área de la muestra. En este contexto, la investigación dirigida hacia la fabricación de sustratos de SERS ideales sigue siendo un campo de investigación ampliamente abierto, donde todavía es necesario hacer grandes esfuerzos.

6.3 Bosques de Nanohilos de Oro Para Detección por SERS

En el capítulo 2 se describe el crecimiento de nanohilos verticales sobre un soporte sólido. Este enfoque permite controlar fácilmente tanto la longitud como el diámetro de los nanohilos ajustando diferentes parámetros tales como el tiempo de crecimiento y la relación entre ácido mercaptobenzoico (MBA) y Au(III) empleados en la solución de crecimiento. De acuerdo con la explicación dada por He *et al.*,[140] el crecimiento vertical tiene lugar como consecuencia de la diferente funcionalidad superficial entre el soporte de vidrio y las semillas de oro ancladas a este. Gracias a la interacción favorable $–NH_2$-Au, las semillas de oro estabilizadas con citrato se unen fuertemente a un portaobjetos de vidrio funcionalizado con aminopropiltrietoxisilano (APTES). Este sustrato se sumerge dentro de la solución de crecimiento, que contiene MBA. En este paso, el MBA cubre casi toda la superficie de las semillas, dejando descubierta sólo su parte inferior, donde la sustitución de citrato por MBA se impide debido a la presencia del APTES. Como consecuencia, la reducción de Au(III) se produce sólo en esta zona inferior, haciendo que las semillas se eleven y el crecimiento se produzca verticalmente.

De esta manera es posible desplazar la banda plasmónica del sustrato hacia la región que resulte de interés según nuestras condiciones, como por ejemplo la longitud de onda del láser de excitación. Tal como se aprecia en el espectro UV-Vis, al aumentar la longitud de los nanohilos, la banda plasmónica se desplaza hacia longitudes de onda mayores (Figura 6.1a).

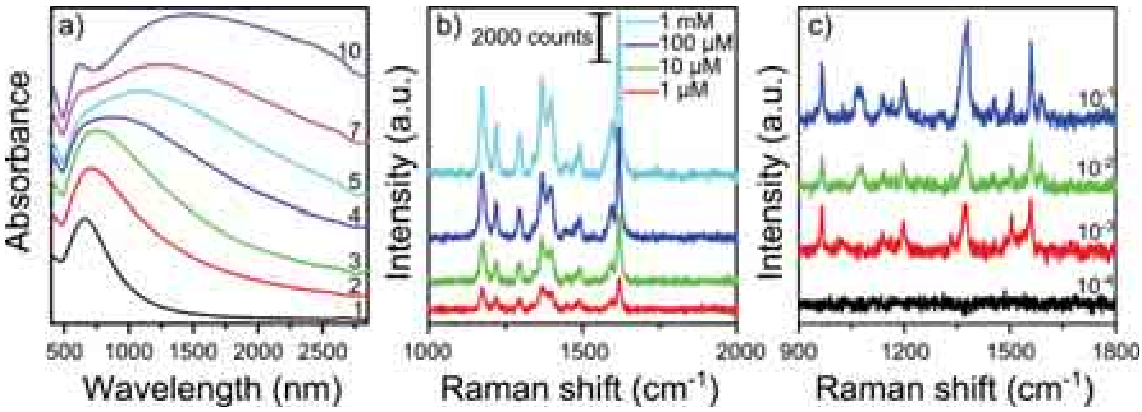

Figura 6.1. (a) Espectros UV-Vis de los nanohilos de oro después de diferentes tiempos de crecimiento (min). (b,c) Espectros SERS de MG en disolución y 1-NAT en fase gas, respectivamente.

La eficiencia SERS de los sustratos de nanohilos se ha comparado usando como analitos verde de malaquita (MG) en disolución, y 1-naftalenotiol (1-NAT) en fase gaseosa (Figura 6.1b, c), obteniéndose límites de detección de 1 µM y 1 mM, respectivamente. Sin embargo, es importante resaltar que la concentración 1 mM de 1-NAT se refiere a la disolución antes de evaporarse. Por tanto, se estima que en fase gaseosa se pueden detectar concentraciones de 1-NAT inferiores a 1 µM.

Por último, se han realizado experimentos SERS en varios ciclos para demostrar la posibilidad de reciclaje de los substratos obtenidos. Se han conseguido detectar hasta cuatro analitos diferentes usando el mismo sustrato plasmónico y aplicando de forma alternada limpieza por plasma e incubación con las diferentes disoluciones de analito.

6.4 Enfoque "pen on paper" hacia el Diseño Universal de Substratos para Dispersión Raman Aumentada en Superficie

En el capítulo 3 se presenta un enfoque "pen on paper" para fabricar sustratos de SERS. Utilizando una pluma estilográfica ordinaria cargada con tinta a base de nanopartículas plasmónicas, se han obtenido sustratos en soporte de papel. Nanoesferas de oro y plata, y nanobastones de oro han sido empleados como tinta para escribir matrices activas en SERS sobre papel industrial estándar, las cuales permiten además utilizar varias longitudes de onda de excitación. La Figura 6.2a muestra cómo se pueden fabricar de forma fácil y sencilla sustratos de SERS sobre papel, simplemente dibujando el patrón deseado con la pluma.

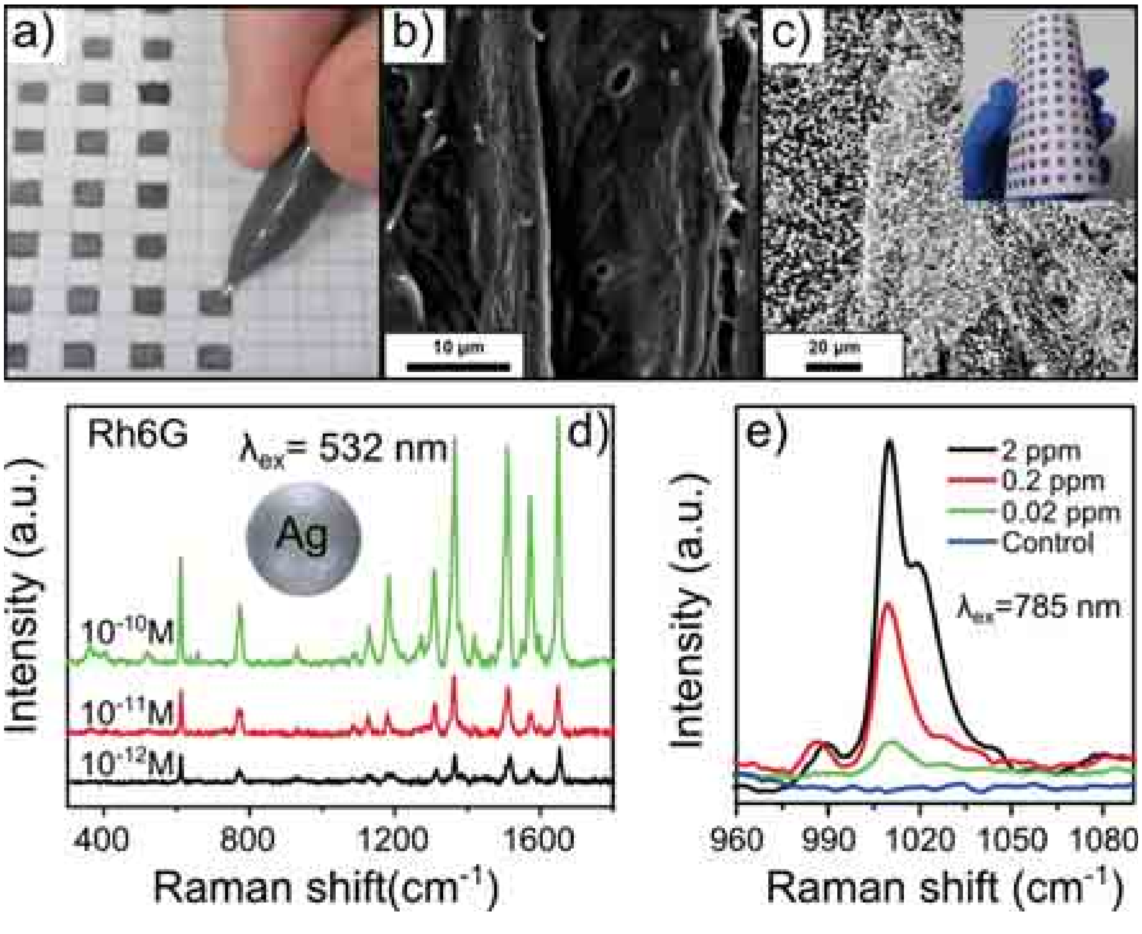

Figura 6.2. (a) Imagen del proceso de escritura y obtención de sustratos de SERS sobre papel. (b,c) Imágenes SEM del papel antes y después de la aplicación de la tinta de nanopartículas. (d,e) Límite de detección de Rodamina 6G y Tiabendazol, respectivamente. En ambos casos se han utilizado nanopartículas de Ag pero con dos longitudes de onda de excitación diferentes.

Las imágenes de SEM presentadas en la Figura 6.2 b y c muestran las fibras de papel antes y después del proceso de escritura. Se puede apreciar cómo las nanopartículas liberadas por la pluma forman una cobertura densa y uniforme sobre el soporte de papel. Los diferentes sustratos obtenidos han sido comparados según su eficiencia en SERS para detectar dos colorantes orgánicos diferentes, con las tres morfologías de nanopartículas y con tres láseres de excitación con longitudes de onda diferentes. En particular, tal y como se muestra en la figura 6.2d, el uso de nanopartículas de Ag y el láser a 532 nm nos permitió detectar Rodamina 6G a 10-12 M. Usando nanopartículas de Ag se han obtenido en todos los experimentos la mayor intensidad de SERS, seguidos de los nanobastones y las nanoesferas de oro. Aparte de los analitos convencionales, también se han podido detectar compuestos químicos más interesantes desde un punto de vista biológico. En este caso, se ha podido observar la huella digital Raman del plaguicida tiabendazol (Figura 6.2e) en concentraciones de hasta 20 ppb.

Por último, se han llevado a cabo varias series de experimentos y pruebas con el fin de demostrar la uniformidad y la estabilidad de este tipo de sustratos, con resultados muy prometedores en ambos casos. De hecho, se han registrado variaciones de intensidad de solamente un 20% usando este tipo de sustratos, los cuales además presentan muy alta estabilidad física cuando son sumergidos en agua y posteriormente secados.

6.5 La Importancia del Ion Citrato como Agente Estabilizante de Nanopartículas de Oro para Dispersión Raman Aumentada en Superficie

La eficiencia SERS de un sustrato está estrechamente vinculada, entre muchos otros factores, a la morfología y a la química superficial de las nanopartículas utilizadas como soporte. En el capítulo 4, se presenta un estudio sobre el efecto de estos dos aspectos. Para ello se utilizaron nanopartículas de diferente geometría, tales como nanobastones (Figura 6.3a), nanotriángulos (Figura 6.3b) y nanoesferas de oro (Figura 6.3c) de alrededor de 90 nm de diámetro, y bromuro de hexadeciltrimetilamonio (CTAB) y citrato de sodio como surfactantes. Con el fin de maximizar la respuesta en SERS de estas nanoestructuras, primero se optimizaron las condiciones experimentales analizando el efecto de la concentración de CTAB en las distintas disoluciones de nanopartículas para todas las longitudes de onda de excitación. Los resultados muestran que cuando se emplean nanotriángulos excitados a 633 nm se obtiene la máxima intensidad de SERS en la detección de Violeta Cristal (CV), una molécula activa en Raman estándar que se emplea en este tipo de experimentos (Figura 6.3d).

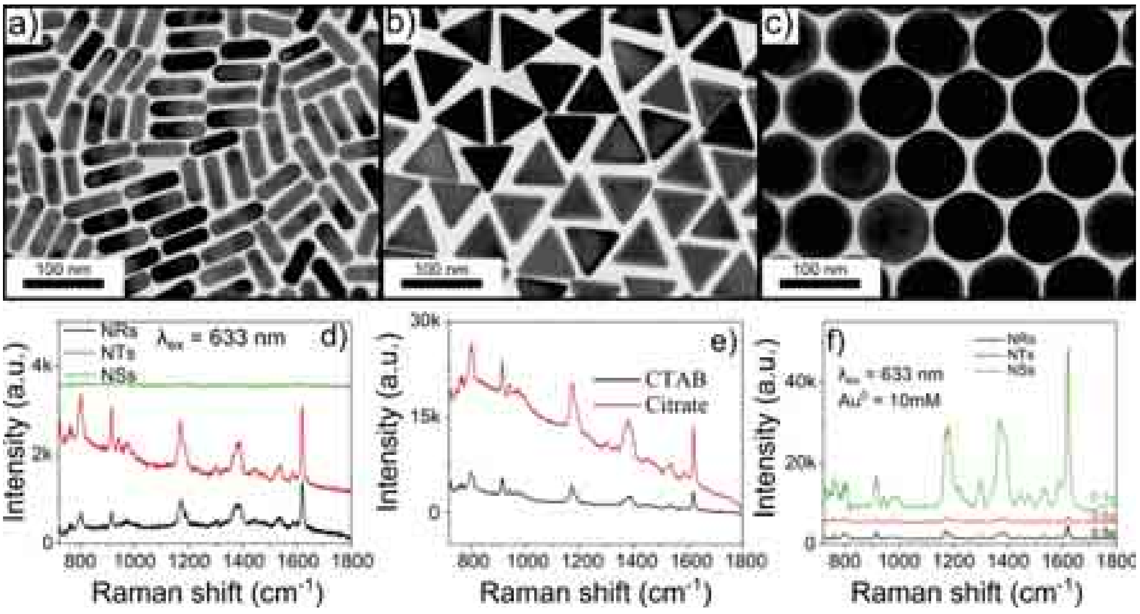

Figura 6.3. (a-c) Imágenes TEM de nanobastones (a), nanotriángulos (b) y nanoesferas de oro (c). (d) Espectros SERS de CV para las tres geometrías de partícula con una longitud de onda de excitación de 633 nm. (e) Comparación entre la eficiencia en SERS de nanotriángulos funcionalizados con CTAB y con citrato en disolución. (f) Espectros SERS de las tres geometrías de partícula sobre un sustrato sólido.

Con el fin de aumentar aun más la eficiencia en SERS de los nanotriángulos, se llevó a cabo la sustitución de CTAB por citrato de sodio de acuerdo con un protocolo recientemente publicado,[184] de forma que eliminando la bicapa de CTAB (la cual se sabe que es estable y gruesa) que recubre la superficie de las nanopartículas se pueda favorecer el acceso del analito a la superficie metálica, donde se genera un campo eléctrico de muy alta intensidad. Efectivamente, tal como se aprecia en la Figura 6.3e, se obtienen intensidades de SERS aproximadamente tres veces superiores para las nanopartículas estabilizadas con iones citrato. Usando esta estrategia se ha establecido un límite de detección de CV de 1 nM.

La eficiencia en SERS de las nanopartículas estabilizadas con citrato también se ha analizado cuando estas forman monocapa densa y uniforme sobre un soporte de vidrio previamente funcionalizado con APTES. A diferencia de la situación en disolución, las nanoesferas de oro de aproximadamente 45 nm de radio dieron lugar a las intensidades SERS más elevadas (Figura 6.3f). De hecho, incluso cuando se emplean tiempos de integración 5 veces menores, las partículas esféricas resultan ser la morfología más eficiente. Por último, la versatilidad de los sustratos preparados se ha demostrado mediante la detección de un analito diferente, en este caso ácido 4-mercaptobenzoico (MBA). Tanto para CV como MBA las nanoesferas de 90 nm de diámetro resultan ser las nanopartículas más eficientes en SERS.

6.6 Compuestos Coloidales Autoensamblados Multifuncionales y su Aplicación a la Detección por SERS

En el capítulo 5 se presenta una novedosa estrategia para preparar susbtratos de SERS híbridos. Se han empleado nanoestrellas de oro y nanopartículas de Fe_3O_4, de forma que ante la aplicación de un campo magnético externo se favorece la acumulación de las nanopartículas y la interacción entre las puntas de diferentes nanoestrellas, dando lugar a intensidades de SERS muy elevadas. Gracias a las interacciones hidrófobas que tienen lugar entre ligandos poliméricos, se ha obtenido una dispersión coloidal estable de partículas compuestas donde una nanoestrella de oro individual está rodeada de cientos de nanopartículas de Fe_3O_4 dentro de una esfera externa de un copolímero de poliestireno y ácido poliacrílico (Figura 6.4a). Se ha comprobado que la eficiencia en SERS de este sistema depende fuertemente de la presencia de un campo magnético externo capaz de inducir la agregación de las partículas plasmónicas. Usando verde de malaquita (MG) como molécula activa en Raman se ha comparado la intensidad de SERS antes y después de la aplicación de un pequeño imán de mano. Los resultados muestran valores de intensidad SERS aproximadamente un orden de magnitud más altos cuando una cuando se induce la agregación por campo magnético (Figura 6.4b).

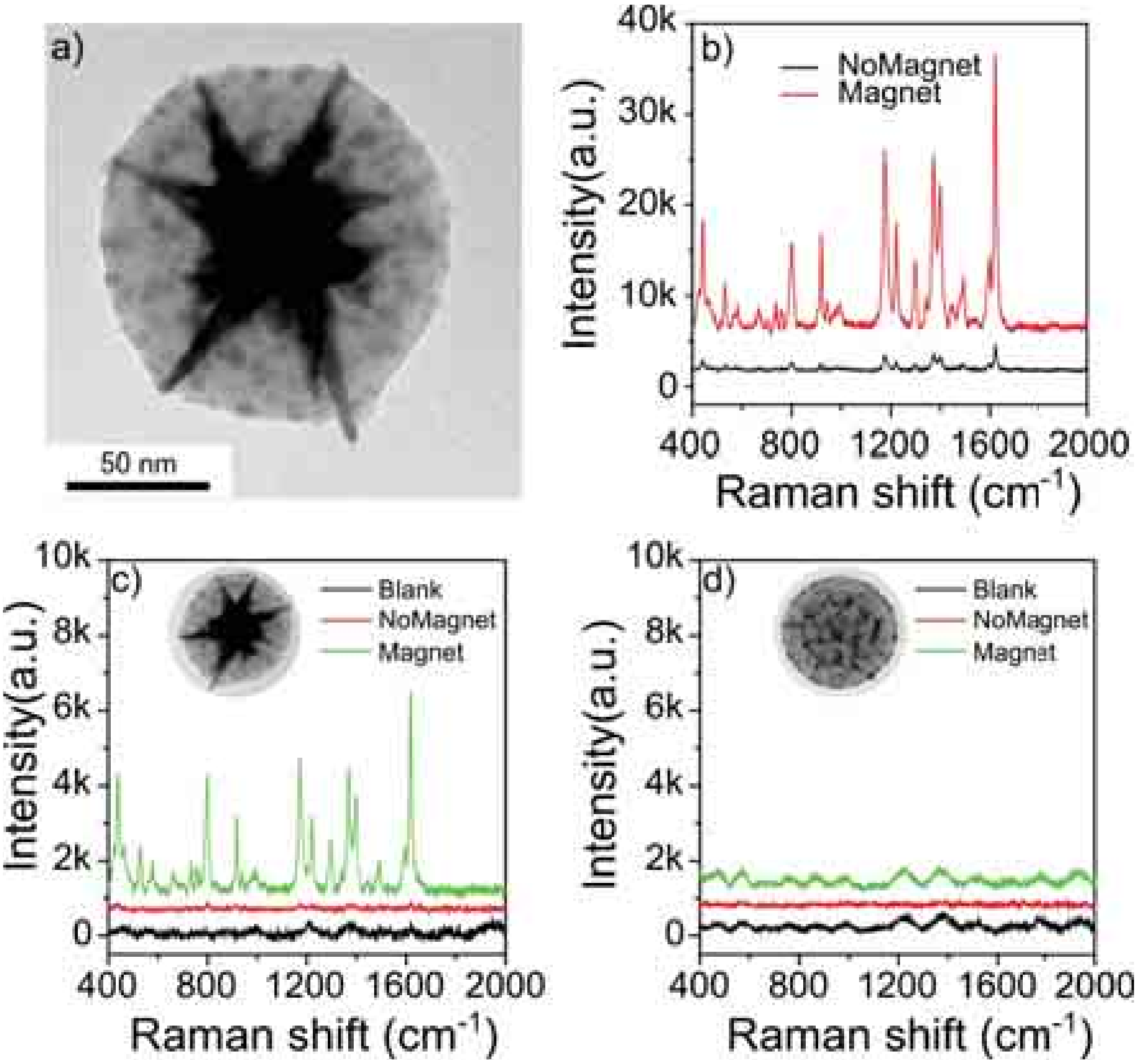

Figura 6.4. (a) Imagen TEM de una partícula nanocompuesta. (b) Comparación entre la intensidad de SERS, medida antes y después de la aplicación de un campo magnético externo. (c, d) Espectros de SERS de MG en presencia y ausencia, respectivamente, de nanoestrellas de oro dentro de la esfera polimérica.

Aunque el aumento de la señal de SERS puede deberse simplemente a la acumulación local de analito, se espera además que la formación de puntos calientes como consecuencia de la agregación de las nanoestrellas sea el factor principal que provoca un aumento significativamente en la intensidad de SERS. Para demostrar esta hipótesis, se compararon las intensidades de SERS de los nanocompuestos magneto-ópticos con otros nanocompuestos formados exclusivamente por nanopartículas magnéticas bajo condiciones experimentales idénticas (Figura 6.4c, d). La ausencia de señal cuando las nanoestrellas no están presentes confirma la importancia del intenso campo eléctrico que se genera en las puntas de las nanoestrellas. La principal ventaja de este método consiste en la posibilidad de aumentar la sensibilidad SERS cuando se emplean concentraciones muy bajas de analito. Por último, se ha calculado el límite de detección para MG y CV, en ambos casos alcanzándose el rango nanomolar.

6.7 Conclusiones

Esta tesis está enfocada al desarrollo de nuevas estrategias para la preparación de sustratos de SERS. Mediante el auto-ensamblaje, la aplicación de estímulos magnéticos y la funcionalización superficial de nanopartículas, se han podido alcanzar los principales objetivos planteados. A continuación se presenta un breve resumen de los resultados específicos obtenidos.

- ✓ Se ha conseguido crecer verticalmente una densa monocapa de nanohilos de oro sobre un soporte de vidrio. Modificando la relación entre las concentraciones de MBA y borohidruro sódico se ha podido controlar el diámetro de los hilos, mientras que su longitud se ha controlado mediante el ajuste de los tiempos de reacción. De esta forma, se ha conseguido controlar también la posición de la banda plasmónica. Tras limpiar mediante tratamiento con plasma la superficie plasmónica, se ha demostrado la eficiencia de estos substratos para detectar 1-NAT tanto en disolución como en fase gaseosa, llegando a alcanzar límites de detección de 1 µM. Además, los sustratos obtenidos pueden ser reutilizados, tal como se ha demostrado al detectar diferentes analitos tras limpiar e incubar el mismo substrato con las distintas disoluciones de forma cíclica.
- ✓ Se ha empleado un papel comercial estándar para fabricar de forma sencilla y económica soportes de SERS que permiten la adsorción de diferentes nanopartículas. Las fibras de papel se han podido impregnar totalmente de nanopartículas de oro y plata usando para ello una pluma estilográfica ordinaria, donde los nanocoloides preparados han sido usados como tinta. Estos sustratos presentan un alto grado de reproducibilidad y uniformidad además de una alta eficiencia en SERS, pudiéndose detectar concentraciones picomolares de Rodamina-6G y ser empleados en aplicaciones prácticas como la detección del plaguicida Tiabendazol.

- ✓ Se han empleado nanopartículas isótropas y anisótropas de oro, tales como esferas, nanobastones y nanotriángulos, para estudiar la influencia de la presencia de surfactantes en la eficiencia SERS de dichas nanopartículas. Al comparar CTAB y citrato como estabilizantes, se ha comprobado que las partículas que dan lugar a una mayor eficiencia en SERS son los nanotriángulos estabilizados con citrato, llegando a detectar en este caso concentraciones hasta 10^{-9} M de CV cuando se emplean condiciones experimentales óptimas. Las partículas estabilizadas con citrato se han estudiado asimismo un vez ensambladas en forma de monocapas sobre soportes de vidrio. En este caso los resultados obtenidos con el láser de 633 nm han revelado que, al contrario de lo que se ha observado en disolución, las nanoesferas de oro dan lugar a las mayores intensidades SERS.
- ✓ Se ha desarrollado un sistema híbrido compuesto por nanoestrellas de oro y nanopartículas de magnetita. Se ha demostrado que, mediante la aplicación de un campo magnético externo, es posible aumentar varios órdenes de magnitud la eficiencia del sistema para detección por SERS. La peculiar morfología de esta nanoestructura permite que las puntas de oro de las nanoestrellas, que presentan campos eléctricos muy intensos, se encuentren muy próximas entre sí, dando lugar a la formación de puntos calientes.

Según los resultados presentados en este trabajo, se espera que esta tesis contribuya al desarrollo de nuevos y más eficientes sustratos para detección por SERS y como consecuencia mejore significativamente el potencial de esta técnica espectroscópica como técnica analítica ultrasensible.

REFERENCES

1. Raman, C. V. & Krishnan, K. S. A New Type of Secondary Radiation. *Nature* **121,** 501–502 (1928).

2. Wiley: Modern Raman Spectroscopy: A Practical Approach - Ewen Smith, Geoffrey Dent. at <http://eu.wiley.com/WileyCDA/WileyTitle/productCd-0471497940.html>

3. Ru, E. L. & Etchegoin, P. *Principles of Surface-Enhanced Raman Spectroscopy: and related plasmonic effects*. (Elsevier, 2008).

4. Aroca, R. in *Surface-Enhanced Vibrational Spectroscopy* 1–33 (John Wiley & Sons, Ltd, 2006). at <http://onlinelibrary.wiley.com/doi/10.1002/9780470035641.ch1/summary>

5. Fleischmann, M., Hendra, P. J. & McQuillan, A. J. Raman spectra of pyridine adsorbed at a silver electrode. *Chem. Phys. Lett.* **26,** 163–166 (1974).

6. Jeanmaire, D. L. & Van Duyne, R. P. Surface raman spectroelectrochemistry: Part I. Heterocyclic, aromatic, and aliphatic amines adsorbed on the anodized silver electrode. *J. Electroanal. Chem. Interfacial Electrochem.* **84,** 1–20 (1977).

7. Albrecht, M. G. & Creighton, J. A. Anomalously intense Raman spectra of pyridine at a silver electrode. *J. Am. Chem. Soc.* **99,** 5215–5217 (1977).

8. Nie, S. & Emory, S. R. Probing Single Molecules and Single Nanoparticles by Surface-Enhanced Raman Scattering. *Science* **275,** 1102–1106 (1997).

9. Kneipp, K. *et al.* Single Molecule Detection Using Surface-Enhanced Raman Scattering (SERS). *Phys. Rev. Lett.* **78,** 1667–1670 (1997).

10. Goulet, P. J. G. & Aroca, R. F. Distinguishing Individual Vibrational Fingerprints: Single-Molecule Surface-Enhanced Resonance Raman Scattering from One-to-One Binary Mixtures in Langmuir−Blodgett Monolayers. *Anal. Chem.* **79,** 2728–2734 (2007).

11. McCabe, A. F. *et al.* SERRS labelled beads for multiplex detection. *Faraday Discuss.* **132,** 303–308 (2006).

12. Smith, W. E. Practical understanding and use of surface enhanced Raman scattering/surface enhanced resonance Raman scattering in chemical and biological analysis. *Chem. Soc. Rev.* **37,** 955–964 (2008).

13. Lyandres, O. *et al.* Real-Time Glucose Sensing by Surface-Enhanced Raman Spectroscopy in Bovine Plasma Facilitated by a Mixed Decanethiol/Mercaptohexanol Partition Layer. *Anal. Chem.* **77,** 6134–6139 (2005).

14. Faulds, K., Barbagallo, R. P., Keer, J. T., Smith, W. E. & Graham, D. SERRS as a more sensitive technique for the detection of labelled oligonucleotides compared to fluorescence. *Analyst* **129,** 567–568 (2004).

15. Sabatté, G. *et al.* Comparison of Surface-Enhanced Resonance Raman Scattering and Fluorescence for Detection of a Labeled Antibody. *Anal. Chem.* **80,** 2351–2356 (2008).

16. Koo, T.-W. *et al.* Specific Chemical Effects on Surface-Enhanced Raman Spectroscopy for Ultra-Sensitive Detection of Biological Molecules. *Appl. Spectrosc.* **58,** 1401–1407 (2004).

17. Vo-Dinh, T., Allain, L. R. & Stokes, D. L. Cancer gene detection using surface-enhanced Raman scattering (SERS). *J. Raman Spectrosc.* **33,** 511–516 (2002).

18. Haynes, C. L., Yonzon, C. R., Zhang, X. & Van Duyne, R. P. Surface-enhanced Raman sensors: early history and the development of sensors for quantitative biowarfare agent and glucose detection. *J. Raman Spectrosc.* **36,** 471–484 (2005).

19. Sägmüller, B., Schwarze, B., Brehm, G. & Schneider, S. Application of SERS spectroscopy to the identificationof (3,4-methylenedioxy)amphetamine in forensic samples utilizing matrixstabilized silver halides. *Analyst* **126,** 2066–2071 (2001).

20. Chen, K. *et al.* Application of surface-enhanced Raman scattering (SERS) for the identification of anthraquinone dyes used in works of art. *J. Raman Spectrosc.* **37,** 520–527 (2006).

21. Centeno, S. A. & Shamir, J. Surface enhanced Raman scattering (SERS) and FTIR characterization of the sepia melanin pigment used in works of art. *J. Mol. Struct.* **873,** 149–159 (2008).

22. Kui Chen, Marco Leona & Tuan Vo-Dinh. Surface-enhanced Raman scattering for identification of organic pigments and dyes in works of art and cultural heritage materialnull. *Sens. Rev.* **27,** 109–120 (2007).

23. Abalde-Cela, S. *et al.* Surface-enhanced Raman scattering biomedical applications of plasmonic colloidal particles. *J. R. Soc. Interface* **7,** S435–S450 (2010).

24. Wiley: Surface Enhanced Raman Spectroscopy: Analytical, Biophysical and Life Science Applications - Sebastian Schlucker, Wolfgang Kiefer. at <http://eu.wiley.com/WileyCDA/WileyTitle/productCd-3527325670.html>

25. Vial, A. Implementation of the critical points model in the recursive convolution method for modelling dispersive media with the finite-difference time domain method. *J. Opt. Pure Appl. Opt.* **9,** 745 (2007).

26. Palik, E. D. *Handbook of optical constants of solids*. (Academic Press, 1985).

27. Tian, Z.-Q., Ren, B. & Wu, D.-Y. Surface-Enhanced Raman Scattering: From Noble to Transition Metals and from Rough Surfaces to Ordered Nanostructures. *J. Phys. Chem. B* **106,** 9463–9483 (2002).

28. Tian, Z. Q. *et al.* Can surface Raman spectroscopy be a general technique for surface science and electrochemistry? *J. Raman Spectrosc.* **29,** 703–711 (1998).

29. Tian, Z.-Q. & Ren, B. Adsorption and Reaction at Electrochemical Interfaces as Probed by Surface-Enhanced Raman Spectroscopy. *Annu. Rev. Phys. Chem.* **55,** 197–229 (2004).

30. Hudson, S. D. & Chumanov, G. Bioanalytical applications of SERS (surface-enhanced Raman spectroscopy). *Anal. Bioanal. Chem.* **394,** 679–686 (2009).

31. Lee, S. *et al.* Biological Imaging of HEK293 Cells Expressing PLCγ1 Using Surface-Enhanced Raman Microscopy. *Anal. Chem.* **79,** 916–922 (2007).

32. Smith, A. M., Mancini, M. C. & Nie, S. Bioimaging: Second window for in vivo imaging. *Nat. Nanotechnol.* **4,** 710–711 (2009).

33. Weissleder, R. A clearer vision for in vivo imaging. *Nat. Biotechnol.* **19,** 316–317 (2001).

34. Schlücker, S. Surface-Enhanced Raman Spectroscopy: Concepts and Chemical Applications. *Angew. Chem. Int. Ed.* **53,** 4756–4795 (2014).

35. Le Ru, E. C., Blackie, E., Meyer, M. & Etchegoin, P. G. Surface Enhanced Raman Scattering Enhancement Factors: A Comprehensive Study. *J. Phys. Chem. C* **111,** 13794–13803 (2007).

36. Moskovits, M. Surface-enhanced spectroscopy. *Rev. Mod. Phys.* **57,** 783–826 (1985).

37. Wu, D.-Y., Duan, S., Ren, B. & Tian, Z.-Q. Density functional theory study of surface-enhanced Raman scattering spectra of pyridine adsorbed on noble and transition metal surfaces. *J. Raman Spectrosc.* **36,** 533–540 (2005).

38. Creighton, J. A. The resonance Raman contribution to sers: Pyridine on copper or silver in aqueous media. *Surf. Sci.* **173,** 665–672 (1986).

39. Gersten, J. I., Birke, R. L. & Lombardi, J. R. Theory of Enhance I Light Scattering from Molecules Adsorbed at the Metal-Solution Interface. *Phys. Rev. Lett.* **43,** 147–150 (1979).

40. Xie, Y. *et al.* Adsorption and photon-driven charge transfer of pyridine on a cobalt electrode analyzed by surface enhanced Raman spectroscopy and relevant theories. *J. Electroanal. Chem.* **554–555,** 417–425 (2003).

41. Jiang, Bosnick, K., Maillard, M. & Brus, L. Single Molecule Raman Spectroscopy at the Junctions of Large Ag Nanocrystals. *J. Phys. Chem. B* **107,** 9964–9972 (2003).

42. Alvarez-Puebla, R. A. & Liz-Marzán, L. M. SERS-Based Diagnosis and Biodetection. *Small* **6,** 604–610 (2010).

43. Fan, M., Andrade, G. F. S. & Brolo, A. G. A review on the fabrication of substrates for surface enhanced Raman spectroscopy and their applications in analytical chemistry. *Anal. Chim. Acta* **693,** 7–25 (2011).

44. Skaff, H. & Emrick, T. in *Nanoparticles* (ed. Rotello, V.) 29–52 (Springer US, 2004). at <http://link.springer.com/chapter/10.1007/978-1-4419-9042-6_2>

45. Kleinman, S. L., Frontiera, R. R., Henry, A.-I., Dieringer, J. A. & Duyne, R. P. V. Creating, characterizing, and controlling chemistry with SERS hot spots. *Phys. Chem. Chem. Phys.* **15,** 21–36 (2012).

46. Jin, M., Wolferen, H. van, Wormeester, H., Berg, A. van den & Carlen, E. T. Large-area nanogap plasmon resonator arrays for plasmonics applications. *Nanoscale* **4,** 4712–4718 (2012).

47. Yu, Q. *et al.* Surface-enhanced Raman scattering on gold quasi-3D nanostructure and 2D nanohole arrays. *Nanotechnology* **21,** 355301 (2010).

48. Sivashanmugan, K., Liao, J.-D., You, J.-W. & Wu, C.-L. Focused-ion-beam-fabricated Au/Ag multilayered nanorod array as SERS-active substrate for virus strain detection. *Sens. Actuators B Chem.* **181,** 361–367 (2013).

49. Wu, Y. & Dong, B. Aluminium nanohole arrays enhanced resonance Raman scattering spectra in the near ultraviolet region. *Sci. China Phys. Mech. Astron.* **57,** 2209–2213 (2014).

50. Haynes, C. L. & Van Duyne, R. P. Nanosphere Lithography: A Versatile Nanofabrication Tool for Studies of Size-Dependent Nanoparticle Optics. *J. Phys. Chem. B* **105,** 5599–5611 (2001).

51. Sharma, B. *et al.* High-performance SERS substrates: Advances and challenges. *MRS Bull.* **38,** 615–624 (2013).

52. Zhang, X., Whitney, A. V., Zhao, J., Hicks, E. M. & Van Duyne, R. P. Advances in Contemporary Nanosphere Lithographic Techniques. *J. Nanosci. Nanotechnol.* **6,** 1920–1934 (2006).

53. Hulteen, J. C. & Duyne, R. P. V. Nanosphere lithography: A materials general fabrication process for periodic particle array surfaces. *J. Vac. Sci. Technol. A* **13,** 1553–1558 (1995).

54. Haynes, C. L. & Van Duyne, R. P. Dichroic Optical Properties of Extended Nanostructures Fabricated Using Angle-Resolved Nanosphere Lithography. *Nano Lett.* **3,** 939–943 (2003).

55. Yang, S.-M., Jang, S. G., Choi, D.-G., Kim, S. & Yu, H. K. Nanomachining by Colloidal Lithography. *Small* **2,** 458–475 (2006).

56. Bastús, N. G., Comenge, J. & Puntes, V. Kinetically Controlled Seeded Growth Synthesis of Citrate-Stabilized Gold Nanoparticles of up to 200 nm: Size Focusing versus Ostwald Ripening. *Langmuir* **27,** 11098–11105 (2011).

57. Rodríguez-Fernández, J., Pérez-Juste, J., García de Abajo, F. J. & Liz-Marzán, L. M. Seeded Growth of Submicron Au Colloids with Quadrupole Plasmon Resonance Modes. *Langmuir* **22,** 7007–7010 (2006).

58. Turkevich, J., Stevenson, P. C. & Hillier, J. A study of the nucleation and growth processes in the synthesis of colloidal gold. *Discuss. Faraday Soc.* **11,** 55–75 (1951).

59. Jana, N. R., Gearheart, L. & Murphy, C. J. Wet Chemical Synthesis of High Aspect Ratio Cylindrical Gold Nanorods. *J. Phys. Chem. B* **105,** 4065–4067 (2001).

60. Johnson, C. J., Dujardin, E., Davis, S. A., Murphy, C. J. & Mann, S. Growth and form of gold nanorods prepared by seed-mediated, surfactant-directed synthesis. *J. Mater. Chem.* **12,** 1765–1770 (2002).

61. Gai, P. L. & Harmer, M. A. Surface Atomic Defect Structures and Growth of Gold Nanorods. *Nano Lett.* **2,** 771–774 (2002).

62. Busbee, B. d., Obare, S. o. & Murphy, C. j. An Improved Synthesis of High-Aspect-Ratio Gold Nanorods. *Adv. Mater.* **15,** 414–416 (2003).

63. Pérez-Juste, J., Pastoriza-Santos, I., Liz-Marzán, L. M. & Mulvaney, P. Gold nanorods: Synthesis, characterization and applications. *Coord. Chem. Rev.* **249,** 1870–1901 (2005).

64. Scarabelli, L., Grzelczak, M. & Liz-Marzán, L. M. Tuning Gold Nanorod Synthesis through Prereduction with Salicylic Acid. *Chem. Mater.* **25,** 4232–4238 (2013).

65. Jana, N. R., Gearheart, L. & Murphy, C. J. Wet chemical synthesis of silver nanorods and nanowiresof controllable aspect ratio. *Chem. Commun.* 617–618 (2001). doi:10.1039/B100521I

66. Kumar, P. S., Pastoriza-Santos, I., Rodríguez-González, B., Abajo, F. J. G. de & Liz-Marzán, L. M. High-yield synthesis and optical response of gold nanostars. *Nanotechnology* **19,** 015606 (2008).

67. Barbosa, S. *et al.* Tuning Size and Sensing Properties in Colloidal Gold Nanostars. *Langmuir* **26,** 14943–14950 (2010).

68. Trigari, S. *et al.* Synthesis and modelling of gold nanostars with tunable morphology and extinction spectrum. *J. Mater. Chem.* **21,** 6531–6540 (2011).

69. Yuan, H. *et al.* Gold nanostars: surfactant-free synthesis, 3D modelling, and two-photon photoluminescence imaging. *Nanotechnology* **23,** 075102 (2012).

70. Garcia-Leis, A., Garcia-Ramos, J. V. & Sanchez-Cortes, S. Silver Nanostars with High SERS Performance. *J. Phys. Chem. C* **117,** 7791–7795 (2013).

71. Pastoriza-Santos, I. & Liz-Marzán, L. M. Synthesis of Silver Nanoprisms in DMF. *Nano Lett.* **2,** 903–905 (2002).

72. Chen, S. & Carroll, D. L. Synthesis and Characterization of Truncated Triangular Silver Nanoplates. *Nano Lett.* **2,** 1003–1007 (2002).

73. Shankar, S. S. *et al.* Biological synthesis of triangular gold nanoprisms. *Nat. Mater.* **3,** 482–488 (2004).

74. Shankar, S. S., Rai, A., Ahmad, A. & Sastry, M. Controlling the Optical Properties of Lemongrass Extract Synthesized Gold Nanotriangles and Potential Application in Infrared-Absorbing Optical Coatings. *Chem. Mater.* **17,** 566–572 (2005).

75. Shankar, S. S., Bhargava, S. & Sastry, M. Synthesis of Gold Nanospheres and Nanotriangles by the Turkevich Approach. *J. Nanosci. Nanotechnol.* **5,** 1721–1727 (2005).

76. Millstone, J. E., Hurst, S. J., Métraux, G. S., Cutler, J. I. & Mirkin, C. A. Colloidal Gold and Silver Triangular Nanoprisms. *Small* **5,** 646–664 (2009).

77. Scarabelli, L., Coronado-Puchau, M., Giner-Casares, J. J., Langer, J. & Liz-Marzán, L. M. Monodisperse Gold Nanotriangles: Size Control, Large-Scale Self-Assembly, and Performance in Surface-Enhanced Raman Scattering. *ACS Nano* **8,** 5833–5842 (2014).

78. Jana, N. R., Gearheart, L. & Murphy, C. J. Wet chemical synthesis of silver nanorods and nanowiresof controllable aspect ratio. *Chem. Commun.* 617–618 (2001). doi:10.1039/B100521I

79. Fu, H., Yang, X., Jiang, X. & Yu, A. Bimetallic Ag–Au Nanowires: Synthesis, Growth Mechanism, and Catalytic Properties. *Langmuir* **29,** 7134–7142 (2013).

80. Brinson, B. E. *et al.* Nanoshells Made Easy: Improving Au Layer Growth on Nanoparticle Surfaces. *Langmuir* **24,** 14166–14171 (2008).

81. Sun, Y. & Xia, Y. Shape-Controlled Synthesis of Gold and Silver Nanoparticles. *Science* **298,** 2176–2179 (2002).

82. Langille, M. R., Personick, M. L., Zhang, J. & Mirkin, C. A. Defining Rules for the Shape Evolution of Gold Nanoparticles. *J. Am. Chem. Soc.* **134,** 14542–14554 (2012).

83. Hao, E., Kelly, K. L., Hupp, J. T. & Schatz, G. C. Synthesis of Silver Nanodisks Using Polystyrene Mesospheres as Templates. *J. Am. Chem. Soc.* **124,** 15182–15183 (2002).

84. Jena, B. K. & Raj, C. R. Seedless, Surfactantless Room Temperature Synthesis of Single Crystalline Fluorescent Gold Nanoflowers with Pronounced SERS and Electrocatalytic Activity. *Chem. Mater.* **20,** 3546–3548 (2008).

85. Zhao, L. *et al.* Formation and Stability of Gold Nanoflowers by the Seeding Approach: The Effect of Intraparticle Ripening. *J. Phys. Chem. C* **113,** 16645–16651 (2009).

86. Huang, C.-J., Chiu, P.-H., Wang, Y.-H. & Yang, C.-F. Synthesis of the gold nanodumbbells by electrochemical method. *J. Colloid Interface Sci.* **303,** 430–436 (2006).

87. Huang, C.-J. *et al.* Preparation and characterization of gold nanodumbbells. *Nanotechnology* **17,** 5355 (2006).

88. Novikov, S. M. *et al.* Gold Spiky Nanodumbbells: Anisotropy in Gold Nanostars. *Part. Part. Syst. Charact.* **31,** 77–80 (2014).

89. Bakshi, M. S., Possmayer, F. & Petersen, N. O. Aqueous-Phase Room-Temperature Synthesis of Gold Nanoribbons: Soft Template Effect of a Gemini Surfactant. *J. Phys. Chem. C* **112,** 8259–8265 (2008).

90. Tan, Y. N., Lee, J. Y. & Wang, D. I. C. Aspartic Acid Synthesis of Crystalline Gold Nanoplates, Nanoribbons, and Nanowires in Aqueous Solutions. *J. Phys. Chem. C* **112,** 5463–5470 (2008).

91. Lu, X., Rycenga, M., Skrabalak, S. E., Wiley, B. & Xia, Y. Chemical Synthesis of Novel Plasmonic Nanoparticles. *Annu. Rev. Phys. Chem.* **60,** 167–192 (2009).

92. Langer, J., Novikov, S. M. & Liz-Marzán, L. M. Sensing using plasmonic nanostructures and nanoparticles. *Nanotechnology* **26,** 322001 (2015).

93. Kimling, J. *et al.* Turkevich Method for Gold Nanoparticle Synthesis Revisited. *J. Phys. Chem. B* **110,** 15700–15707 (2006).

94. Frens, G. Particle size and sol stability in metal colloids. *Kolloid-Z. Z. Für Polym.* **250,** 736–741 (1972).

95. Lee, P. C. & Meisel, D. Adsorption and surface-enhanced Raman of dyes on silver and gold sols. *J. Phys. Chem.* **86,** 3391–3395 (1982).

96. Leopold, N. & Lendl, B. A New Method for Fast Preparation of Highly Surface-Enhanced Raman Scattering (SERS) Active Silver Colloids at Room Temperature by Reduction of Silver Nitrate with Hydroxylamine Hydrochloride. *J. Phys. Chem. B* **107,** 5723–5727 (2003).

97. Yu, Y. & Zhang, G. in *Updates in Advanced Lithography* (ed. Hosaka, S.) (InTech, 2013). at <http://www.intechopen.com/books/updates-in-advanced-lithography/colloidal-lithography>

98. Yap, F. L., Thoniyot, P., Krishnan, S. & Krishnamoorthy, S. Nanoparticle Cluster Arrays for High-Performance SERS through Directed Self-Assembly on Flat Substrates and on Optical Fibers. *ACS Nano* **6,** 2056–2070 (2012).

99. Alvarez-Puebla, R. A. *et al.* Gold nanorods 3D-supercrystals as surface enhanced Raman scattering spectroscopy substrates for the rapid detection of scrambled prions. *Proc. Natl. Acad. Sci.* **108,** 8157–8161 (2011).

100. Lohmueller, T., Bock, E. & Spatz, J. P. Synthesis of Quasi-Hexagonal Ordered Arrays of Metallic Nanoparticles with Tuneable Particle Size. *Adv. Mater.* **20,** 2297–2302 (2008).

101. Gandra, N., Abbas, A., Tian, L. & Singamaneni, S. Plasmonic Planet–Satellite Analogues: Hierarchical Self-Assembly of Gold Nanostructures. *Nano Lett.* **12,** 2645–2651 (2012).

102. Gómez-Graña, S., Pérez-Juste, J., Alvarez-Puebla, R. A., Guerrero-Martínez, A. & Liz-Marzán, L. M. Self-Assembly of Au@Ag Nanorods Mediated by Gemini Surfactants for Highly Efficient SERS-Active Supercrystals. *Adv. Opt. Mater.* **1,** 477–481 (2013).

103. Oh, M. K., Yun, S., Kim, S. K. & Park, S. Effect of layer structures of gold nanoparticle films on surface enhanced Raman scattering. *Anal. Chim. Acta* **649,** 111–116 (2009).

104. Fales, A. M., Yuan, H. & Vo-Dinh, T. Silica-Coated Gold Nanostars for Combined Surface-Enhanced Raman Scattering (SERS) Detection and Singlet-Oxygen Generation: A Potential Nanoplatform for Theranostics. *Langmuir* **27,** 12186–12190 (2011).

105. Jun, B.-H. *et al.* Multifunctional Silver-Embedded Magnetic Nanoparticles as SERS Nanoprobes and Their Applications. *Small* **6,** 119–125 (2010).

106. Álvarez-Puebla, R. A., Contreras-Cáceres, R., Pastoriza-Santos, I., Pérez-Juste, J. & Liz-Marzán, L. M. Au@pNIPAM Colloids as Molecular Traps for Surface-Enhanced, Spectroscopic, Ultra-Sensitive Analysis. *Angew. Chem. Int. Ed.* **48,** 138–143 (2009).

107. Moskovits, M. Surface-enhanced Raman spectroscopy: a brief retrospective. *J. Raman Spectrosc.* **36,** 485–496 (2005).

108. Quinten, M. Local fields close to the surface of nanoparticles and aggregates of nanoparticles. *Appl. Phys. B-Lasers Opt.* **73,** 245–255 (2001).

109. McMahon, J. M., Li, S., Ausman, L. K. & Schatz, G. C. Modeling the Effect of Small Gaps in Surface-Enhanced Raman Spectroscopy. *J. Phys. Chem. C* **116,** 1627–1637 (2012).

110. Shafer-Peltier, K. E., Haynes, C. L., Glucksberg, M. R. & Van Duyne, R. P. Toward a Glucose Biosensor Based on Surface-Enhanced Raman Scattering. *J. Am. Chem. Soc.* **125,** 588–593 (2003).

111. Kneipp, J., Kneipp, H., McLaughlin, M., Brown, D. & Kneipp, K. In Vivo Molecular Probing of Cellular Compartments with Gold Nanoparticles and Nanoaggregates. *Nano Lett.* **6,** 2225–2231 (2006).

112. Vo-Dinh, T., Yan, F. & Wabuyele, M. B. Surface-enhanced Raman scattering for medical diagnostics and biological imaging. *J. Raman Spectrosc.* **36,** 640–647 (2005).

113. Alvarez-Puebla, R. A., Zubarev, E. R., Kotov, N. A. & Liz-Marzán, L. M. Self-assembled nanorod supercrystals for ultrasensitive SERS diagnostics. *Nano Today* **7,** 6–9 (2012).

114. Sanles-Sobrido, M. *et al.* Label-free SERS detection of relevant bioanalytes on silver-coated carbon nanotubes: The case of cocaine. *Nanoscale* **1,** 153 (2009).

115. Dasary, S. S. R., Singh, A. K., Senapati, D., Yu, H. & Ray, P. C. Gold Nanoparticle Based Label-Free SERS Probe for Ultrasensitive and Selective Detection of Trinitrotoluene. *J. Am. Chem. Soc.* **131,** 13806–13812 (2009).

116. Harz, M. *et al.* Micro-Raman spectroscopic identification of bacterial cells of the genus Staphylococcus and dependence on their cultivation conditions. *Analyst* **130,** 1543–1550 (2005).

117. Leona, M., Stenger, J. & Ferloni, E. Application of surface-enhanced Raman scattering techniques to the ultrasensitive identification of natural dyes in works of art. *J. Raman Spectrosc.* **37,** 981–992 (2006).

118. Wustholz, K. L., Brosseau, C. L., Casadio, F. & Duyne, R. P. V. Surface-enhanced Raman spectroscopy of dyes: from single molecules to the artists' canvas. *Phys. Chem. Chem. Phys.* **11,** 7350–7359 (2009).

119. Wang, H., Levin, C. S. & Halas, N. J. Nanosphere Arrays with Controlled Sub-10-nm Gaps as Surface-Enhanced Raman Spectroscopy Substrates. *J. Am. Chem. Soc.* **127,** 14992–14993 (2005).

120. Chaney, S. B., Shanmukh, S., Dluhy, R. A. & Zhao, Y.-P. Aligned silver nanorod arrays produce high sensitivity surface-enhanced Raman spectroscopy substrates. *Appl. Phys. Lett.* **87,** 031908 (2005).

121. Gómez-Graña, S., Pérez-Juste, J., Alvarez-Puebla, R. A., Guerrero-Martínez, A. & Liz-Marzán, L. M. Self-Assembly of Au@Ag Nanorods Mediated by Gemini Surfactants for Highly Efficient SERS-Active Supercrystals. *Adv. Opt. Mater.* **1,** 477–481 (2013).

122. Nalbant Esenturk, E. & Hight Walker, A. R. Surface-enhanced Raman scattering spectroscopy via gold nanostars. *J. Raman Spectrosc.* **40,** 86–91 (2009).

123. Lu, G., Li, C. & Shi, G. Synthesis and Characterization of 3D Dendritic Gold Nanostructures and Their Use as Substrates for Surface-Enhanced Raman Scattering. *Chem. Mater.* **19,** 3433–3440 (2007).

124. Xu, P. *et al.* Facile Fabrication of Homogeneous 3D Silver Nanostructures on Gold-Supported Polyaniline Membranes as Promising SERS Substrates. *Langmuir* **26,** 8882–8886 (2010).

125. McLellan, J. M., Siekkinen, A., Chen, J. & Xia, Y. Comparison of the surface-enhanced Raman scattering on sharp and truncated silver nanocubes. *Chem. Phys. Lett.* **427,** 122–126 (2006).

126. Zhu, Y. *et al.* Gold nanorod assembly based approach to toxin detection by SERS. *J. Mater. Chem.* **22,** 2387–2391 (2012).

127. Zheng, Y. *et al.* DNA-Directed Self-Assembly of Core-Satellite Plasmonic Nanostructures: A Highly Sensitive and Reproducible Near-IR SERS Sensor. *Adv. Funct. Mater.* **23,** 1519–1526 (2013).

128. Gunnarsson, L. *et al.* Interparticle coupling effects in nanofabricated substrates for surface-enhanced Raman scattering. *Appl. Phys. Lett.* **78,** 802–804 (2001).

129. Félidj, N. *et al.* Controlling the optical response of regular arrays of gold particles for surface-enhanced Raman scattering. *Phys. Rev. B* **65,** (2002).

130. Kahl, M., Voges, E., Kostrewa, S., Viets, C. & Hill, W. Periodically structured metallic substrates for SERS. *Sens. Actuators B Chem.* **51,** 285–291 (1998).

131. Min, Q., Santos, M. J. L., Girotto, E. M., Brolo, A. G. & Gordon, R. Localized Raman Enhancement from a Double-Hole Nanostructure in a Metal Film. *J. Phys. Chem. C* **112,** 15098–15101 (2008).

132. Gopinath, A. *et al.* Plasmonic Nanogalaxies: Multiscale Aperiodic Arrays for Surface-Enhanced Raman Sensing. *Nano Lett.* **9,** 3922–3929 (2009).

133. Ou, F. S. *et al.* Hot-Spot Engineering in Polygonal Nanofinger Assemblies for Surface Enhanced Raman Spectroscopy. *Nano Lett.* **11,** 2538–2542 (2011).

134. Wells, S. M., Merkulov, I. A., Kravchenko, I. I., Lavrik, N. V. & Sepaniak, M. J. Silicon Nanopillars for Field-Enhanced Surface Spectroscopy. *ACS Nano* **6,** 2948–2959 (2012).

135. Yang, J. *et al.* Surface-Enhanced Raman Spectroscopy Based Quantitative Bioassay on Aptamer-Functionalized Nanopillars Using Large-Area Raman Mapping. *ACS Nano* **7,** 5350–5359 (2013).

136. Srivastava, S., Sinha, R. & Roy, D. Toxicological effects of malachite green. *Aquat. Toxicol.* **66,** 319–329 (2004).

137. Culp, S. J. & Beland, F. A. Malachite Green: A Toxicological Review. *Int. J. Toxicol.* **15,** 219–238 (1996).

138. Panandiker, A., Fernandes, C., Rao, T. K. & Rao, K. V. Morphological transformation of Syrian hamster embryo cells in primary culture by malachite green correlates well with the evidence for formation of reactive free radicals. *Cancer Lett.* **74,** 31–36 (1993).

139. Rao, K. V. K. Inhibition of DNA synthesis in primary rat hepatocyte cultures by malachite green: a new liver tumor promoter. *Toxicol. Lett.* **81,** 107–113 (1995).

140. He, J. *et al.* Forest of Gold Nanowires: A New Type of Nanocrystal Growth. *ACS Nano* **7,** 2733–2740 (2013).

141. Funston, A. M., Novo, C., Davis, T. J. & Mulvaney, P. Plasmon Coupling of Gold Nanorods at Short Distances and in Different Geometries. *Nano Lett.* **9,** 1651–1658 (2009).

142. Dar, M. I., Sampath, S. & Shivashankar, S. A. Microwave-assisted, surfactant-free synthesis of air-stable copper nanostructures and their SERS study. *J. Mater. Chem.* **22,** 22418–22423 (2012).

143. Stiles, P. L., Dieringer, J. A., Shah, N. C. & Van Duyne, R. P. Surface-Enhanced Raman Spectroscopy. *Annu. Rev. Anal. Chem.* **1,** 601–626 (2008).

144. Lee, S. *et al.* Fast and sensitive trace analysis of malachite green using a surface-enhanced Raman microfluidic sensor. *Anal. Chim. Acta* **590,** 139–144 (2007).

145. Lueck, H. B., Daniel, D. C. & McHale, J. L. Resonance Raman study of solvent effects on a series of triarylmethane dyes. *J. Raman Spectrosc.* **24,** 363–370 (1993).

146. Alvarez-Puebla, R. A., Dos Santos, D. S. & Aroca, R. F. Surface-enhanced Raman scattering for ultrasensitive chemical analysis of 1 and 2-naphthalenethiols. *Analyst* **129,** 1251–1256 (2004).

147. Baia, M., Baia, L. & Astilean, S. Gold nanostructured films deposited on polystyrene colloidal crystal templates for surface-enhanced Raman spectroscopy. *Chem. Phys. Lett.* **404,** 3–8 (2005).

148. Polavarapu, L. & Liz-Marzán, L. M. Towards low-cost flexible substrates for nanoplasmonic sensing. *Phys. Chem. Chem. Phys.* **15,** 5288–5300 (2013).

149. Betz, J. F., Yu, W. W., Cheng, Y., White, I. M. & Rubloff, G. W. Simple SERS substrates: powerful, portable, and full of potential. *Phys. Chem. Chem. Phys.* **16,** 2224–2239 (2014).

150. Wei, Q. *et al.* Fluorescent Imaging of Single Nanoparticles and Viruses on a Smart Phone. *ACS Nano* **7,** 9147–9155 (2013).

151. Ayas, S., Cupallari, A., Ekiz, O. O., Kaya, Y. & Dana, A. Counting Molecules with a Mobile Phone Camera Using Plasmonic Enhancement. *ACS Photonics* **1,** 17–26 (2014).

152. Khatua, S. & Orrit, M. Toward Single-Molecule Microscopy on a Smart Phone. *ACS Nano* **7,** 8340–8343 (2013).

153. Anker, J. N. *et al.* Biosensing with plasmonic nanosensors. *Nat. Mater.* **7,** 442–453 (2008).

154. Cao, Y. C., Jin, R. & Mirkin, C. A. Nanoparticles with Raman Spectroscopic Fingerprints for DNA and RNA Detection. *Science* **297,** 1536–1540 (2002).

155. Grzelczak, M. & Liz-Marzán, L. M. Colloidal Nanoplasmonics: From Building Blocks to Sensing Devices. *Langmuir* **29,** 4652–4663 (2013).

156. Camden, J. P., Dieringer, J. A., Zhao, J. & Van Duyne, R. P. Controlled Plasmonic Nanostructures for Surface-Enhanced Spectroscopy and Sensing. *Acc. Chem. Res.* **41,** 1653–1661 (2008).

157. Lohse, S. E. & Murphy, C. J. The Quest for Shape Control: A History of Gold Nanorod Synthesis. *Chem. Mater.* **25,** 1250–1261 (2013).

158. Lee, C. H., Tian, L. & Singamaneni, S. Paper-Based SERS Swab for Rapid Trace Detection on Real-World Surfaces. *ACS Appl. Mater. Interfaces* **2,** 3429–3435 (2010).

159. Yu, W. W. & White, I. M. Chromatographic separation and detection of target analytes from complex samples using inkjet printed SERS substrates. *Analyst* **138,** 3679–3686 (2013).

160. Yu, W. W. & White, I. M. Inkjet-printed paper-based SERS dipsticks and swabs for trace chemical detection. *Analyst* **138,** 1020–1025 (2013).

161. Cheng, M.-L., Tsai, B.-C. & Yang, J. Silver nanoparticle-treated filter paper as a highly sensitive surface-enhanced Raman scattering (SERS) substrate for detection of tyrosine in aqueous solution. *Anal. Chim. Acta* **708,** 89–96 (2011).

162. Lee, C. H., Hankus, M. E., Tian, L., Pellegrino, P. M. & Singamaneni, S. Highly Sensitive Surface Enhanced Raman Scattering Substrates Based on Filter Paper Loaded with Plasmonic Nanostructures. *Anal. Chem.* **83,** 8953–8958 (2011).

163. Yu, W. W. & White, I. M. Inkjet Printed Surface Enhanced Raman Spectroscopy Array on Cellulose Paper. *Anal. Chem.* **82,** 9626–9630 (2010).

164. Zhang, R. *et al.* Highly efficient SERS test strips. *Chem. Commun.* **48,** 5913–5915 (2012).

165. Qu, L.-L. *et al.* Batch fabrication of disposable screen printed SERS arrays. *Lab. Chip* **12,** 876–881 (2012).

166. Ngo, Y. H., Li, D., Simon, G. P. & Garnier, G. Gold Nanoparticle–Paper as a Three-Dimensional Surface Enhanced Raman Scattering Substrate. *Langmuir* **28,** 8782–8790 (2012).

167. Nery, E. W. & Kubota, L. T. Sensing approaches on paper-based devices: a review. *Anal. Bioanal. Chem.* **405,** 7573–7595 (2013).

168. Abbas, A. *et al.* Multifunctional Analytical Platform on a Paper Strip: Separation, Preconcentration, and Subattomolar Detection. *Anal. Chem.* **85,** 3977–3983 (2013).

169. Russo, A. *et al.* Pen-on-Paper Flexible Electronics. *Adv. Mater.* **23,** 3426–3430 (2011).

170. Lim, K. S., Chang, W.-J., Koo, Y.-M. & Bashir, R. Reliable fabrication method of transferable micron scale metal pattern for poly(dimethylsiloxane) metallization. *Lab. Chip* **6,** 578–580 (2006).

171. Su, Q., Ma, X., Dong, J., Jiang, C. & Qian, W. A Reproducible SERS Substrate Based on Electrostatically Assisted APTES-Functionalized Surface-Assembly of Gold Nanostars. *ACS Appl. Mater. Interfaces* **3,** 1873–1879 (2011).

172. Polavarapu, L. *et al.* Alkylamine capped metal nanoparticle 'inks' for printable SERS substrates, electronics and broadband photodetectors. *Nanoscale* **3,** 2268–2274 (2011).

173. Rycenga, M. *et al.* Probing the surface-enhanced Raman scattering properties of Au–Ag nanocages at two different excitation wavelengths. *Phys. Chem. Chem. Phys.* **11,** 5903–5908 (2009).

174. Osinkina, L., Lohmüller, T., Jäckel, F. & Feldmann, J. Synthesis of Gold Nanostar Arrays as Reliable, Large-Scale, Homogeneous Substrates for Surface-Enhanced Raman Scattering Imaging and Spectroscopy. *J. Phys. Chem. C* **117,** 22198–22202 (2013).

175. Nikoobakht, B. & El-Sayed, M. A. Preparation and Growth Mechanism of Gold Nanorods (NRs) Using Seed-Mediated Growth Method. *Chem. Mater.* **15,** 1957–1962 (2003).

176. Faraday, M. The Bakerian Lecture: Experimental Relations of Gold (and Other Metals) to Light. *Philos. Trans. R. Soc. Lond.* **147,** 145–181 (1857).

177. Myroshnychenko, V. *et al.* Modelling the optical response of gold nanoparticles. *Chem. Soc. Rev.* **37,** 1792–1805 (2008).

178. Aizpurua, J. & Hillenbrand, R. in *Plasmonics* (eds. Enoch, S. & Bonod, N.) 151–176 (Springer Berlin Heidelberg, 2012). at <http://link.springer.com/chapter/10.1007/978-3-642-28079-5_5>

179. Rodríguez-Lorenzo, L. *et al.* Zeptomol detection through controlled ultrasensitive surface-enhanced Raman scattering. *J. Am. Chem. Soc.* **131,** 4616–4618 (2009).

180. Zhao, Y. *et al.* Shell-Engineered Chiroplasmonic Assemblies of Nanoparticles for Zeptomolar DNA Detection. *Nano Lett.* **14,** 3908–3913 (2014).

181. Serrano-Montes, A. B. *et al.* A General Method for Solvent Exchange of Plasmonic Nanoparticles and Self-Assembly into SERS-Active Monolayers. *Langmuir ACS J. Surf. Colloids* **31,** 9205–9213 (2015).

182. Scarabelli, L., Coronado-Puchau, M., Giner-Casares, J. J., Langer, J. & Liz-Marzán, L. M. Monodisperse Gold Nanotriangles: Size Control, Large-Scale Self-Assembly, and Performance in Surface-Enhanced Raman Scattering. *ACS Nano* **8,** 5833–5842 (2014).

183. Turkevich, J., Stevenson, P. C. & Hillier, J. A study of the nucleation and growth processes in the synthesis of colloidal gold. *Discuss. Faraday Soc.* **11,** 55–75 (1951).

184. Mehtala, J. G. *et al.* Citrate-Stabilized Gold Nanorods. *Langmuir* **30,** 13727–13730 (2014).

185. Liu, G. L., Lu, Y., Kim, J., Doll, J. C. & Lee, L. P. Magnetic Nanocrescents as Controllable Surface-Enhanced Raman Scattering Nanoprobes for Biomolecular Imaging. *Adv. Mater.* **17,** 2683–2688 (2005).

186. Quaresma, P. *et al.* Star-shaped magnetite@gold nanoparticles for protein magnetic separation and SERS detection. *RSC Adv.* **4,** 3659–3667 (2013).

187. Bao, Z. Y., Dai, J., Lei, D. Y. & Wu, Y. Maximizing surface-enhanced Raman scattering sensitivity of surfactant-free Ag-Fe3O4 nanocomposites through optimization of silver nanoparticle density and magnetic self-assembly. *J. Appl. Phys.* **114,** 124305 (2013).

188. Yoon, M., Kim, Y. & Cho, J. Multifunctional Colloids with Optical, Magnetic, and Superhydrophobic Properties Derived from Nucleophilic Substitution-Induced Layer-by-Layer Assembly in Organic Media. *ACS Nano* **5,** 5417–5426 (2011).

189. Yoon, M., Choi, J. & Cho, J. Multifunctional Colloids with Reversible Phase Transfer between Organic and Aqueous Media via Layer-by-Layer Assembly. *Chem. Mater.* **25,** 1735–1743 (2013).

190. Grzelczak, M. & Liz-Marzán, L. M. Exploiting Hydrophobic Interactions at the Nanoscale. *J. Phys. Chem. Lett.* **5,** 2455–2463 (2014).

191. Contreras-Cáceres, R. *et al.* Multifunctional Microgel Magnetic/Optical Traps for SERS Ultradetection. *Langmuir* **27,** 4520–4525 (2011).

192. Spuch-Calvar, M., Rodríguez-Lorenzo, L., Morales, M. P., Álvarez-Puebla, R. A. & Liz-Marzán, L. M. Bifunctional Nanocomposites with Long-Term Stability as SERS Optical Accumulators for Ultrasensitive Analysis. *J. Phys. Chem. C* **113,** 3373–3377 (2008).

193. Talley, C. E. *et al.* Surface-Enhanced Raman Scattering from Individual Au Nanoparticles and Nanoparticle Dimer Substrates. *Nano Lett.* **5,** 1569–1574 (2005).

194. Li, W., Camargo, P. H. C., Lu, X. & Xia, Y. Dimers of Silver Nanospheres: Facile Synthesis and Their Use as Hot Spots for Surface-Enhanced Raman Scattering. *Nano Lett.* **9,** 485–490 (2009).

195. Nikoobakht, B. & El-Sayed, M. A. Surface-Enhanced Raman Scattering Studies on Aggregated Gold Nanorods†. *J. Phys. Chem. A* **107,** 3372–3378 (2003).

196. Orendorff, C. J., Gearheart, L., Jana, N. R. & Murphy, C. J. Aspect ratio dependence on surface enhanced Raman scattering using silver and gold nanorod substrates. *Phys. Chem. Chem. Phys.* **8,** 165–170 (2006).

197. Wang, Z., Zong, S., Yang, J., Li, J. & Cui, Y. Dual-mode probe based on mesoporous silica coated gold nanorods for targeting cancer cells. *Biosens. Bioelectron.* **26,** 2883–2889 (2011).

198. Potara, M. *et al.* Chitosan-coated triangular silver nanoparticles as a novel class of biocompatible, highly sensitive plasmonic platforms for intracellular SERS sensing and imaging. *Nanoscale* **5,** 6013–6022 (2013).

199. Smitha, S. L. & Gopchandran, K. G. Surface enhanced Raman scattering, antibacterial and antifungal active triangular gold nanoparticles. *Spectrochim. Acta. A. Mol. Biomol. Spectrosc.* **102,** 114–119 (2013).

200. Khoury, C. G. & Vo-Dinh, T. Gold Nanostars For Surface-Enhanced Raman Scattering: Synthesis, Characterization and Optimization. *J. Phys. Chem. C* **112,** 18849–18859 (2008).

201. Rodríguez-Lorenzo, L., Álvarez-Puebla, R. A., de Abajo, F. J. G. & Liz-Marzán, L. M. Surface Enhanced Raman Scattering Using Star-Shaped Gold Colloidal Nanoparticles†. *J. Phys. Chem. C* **114,** 7336–7340 (2010).

202. Hrelescu, C., Sau, T. K., Rogach, A. L., Jäckel, F. & Feldmann, J. Single gold nanostars enhance Raman scattering. *Appl. Phys. Lett.* **94,** 153113 (2009).

203. Park, J. *et al.* Ultra-large-scale syntheses of monodisperse nanocrystals. *Nat. Mater.* **3,** 891–895 (2004).

204. Grzelczak, M., Sánchez-Iglesias, A. & Liz-Marzán, L. M. A general approach toward polymer-coated plasmonic nanostructures. *CrystEngComm* **16,** 9425–9429 (2014).

205. Sánchez-Iglesias, A. *et al.* Hydrophobic Interactions Modulate Self-Assembly of Nanoparticles. *ACS Nano* **6,** 11059–11065 (2012).

206. Hao, F., Nehl, C. L., Hafner, J. H. & Nordlander, P. Plasmon Resonances of a Gold Nanostar. *Nano Lett.* **7,** 729–732 (2007).

207. Liang, E. J., Ye, X. L. & Kiefer, W. Surface-Enhanced Raman Spectroscopy of Crystal Violet in the Presence of Halide and Halate Ions with Near-Infrared Wavelength Excitation. *J. Phys. Chem. A* **101,** 7330–7335 (1997).

208. He, L., Kim, N.-J., Li, H., Hu, Z. & Lin, M. Use of a Fractal-like Gold Nanostructure in Surface-Enhanced Raman Spectroscopy for Detection of Selected Food Contaminants. *J. Agric. Food Chem.* **56,** 9843–9847 (2008).

209. Palenstijn, W. J., Batenburg, K. J. & Sijbers, J. Performance improvements for iterative electron tomography reconstruction using graphics processing units (GPUs). *J. Struct. Biol.* **176,** 250–253 (2011).

210. Palenstijn, W. J., Batenburg, K. J., Sijbers, J. & Sijbers, J. The ASTRA Tomography Toolbox. (2013).

LIST OF PUBLICATIONS

- ✓ Polavarapu L., **La Porta A.**, Novikov S. M., Coronado-Puchau M., Liz-Marzán L. M. “Pen-on-Paper Approach Toward the Design of Universal Surface Enhanced Raman Scattering Substrates” *Small*, **2014**, 10, 3065-3071. Number of citations: 13. Frontispiece of the Issue.

- ✓ **La Porta A.**, Grzelczak M., Liz-Marzán L. M. “Gold Nanowire Forests for SERS Detection” *ChemistryOpen*, **2014**, 106, 146-151. Number of citations: 3. Front cover of Issue.

- ✓ **La Porta A.**, Sánchez-Iglesias A., Altantzis T., Bals S., Grzelczak M., Liz-Marzán L. M. “Multifunctional self-assembled composite colloids and their application to SERS detection” *Nanoscale*, **2015**, 7, 10377-10381. Number of citations: 0. Inside Front Cover of the Issue

- ✓ Hamon C., Henriksen-Lacey M., **La Porta A.**, Langer J., Scarabelli L., Serrano Montes A. B., González-Rubio G., Basabe-Desmonts L., Liz-Marzán L. M. “Tunable nanoparticle and cell assembly using combined self-powered microfluidics and micro-contact printing”, *In preparation*